Measurement of the $t\bar{t}$ production cross section in $p\bar{p}$ collisions at $\sqrt{s} = 1.96$ TeV

by

Heather L. Ray

A dissertation submitted in partial fulfillment
of the requirements for the degree of
Doctor of Philosophy
(Physics)
in The University of Michigan
2004

Doctoral Committee:

Professor Dante Amidei, Chair
Professor Daniel C. Fisher
Professor Gordon Kane
Associate Professor Christopher Monroe
Associate Professor Keith Riles

© Heather Ray 2004
All Rights Reserved

DEDICATION

I dedicate this thesis to my father, Gerald Lee Ray and to my grandfather Harold Wayne Lutz, who could not be here with me today to share in this honor.

ACKNOWLEDGEMENTS

I thank my advisor, Dante Amidei, for having the strength and perseverance to tolerate my stubborn and hot-headed ways. Special thanks are due to Doctors Ken Bloom, J. Stephen Miller, and Monica Tecchio who have answered my numerous questions, and who have provided me with a thorough education in all things related to a particle physics experiment.

I would like to acknowledge my family, without whom this would not be possible: my mother, Susan Marie Ray, my grandmother, Catherine Lutz, my aunt, Carol Lutz, my step-mother, Alice C. Miller, and my pseudo-step-father, Bernard Kalanavich. I would like to thank Ivan K. Furić for being a continual source of unconditional love and support during the entire analysis and thesis writing process. In addition I would like to acknowledge those close friends who have supported me and gently directed me throughout my life when I was going astray: Martin William Pilgram III, Ricka Feeley, and Simon Fitzpatrick.

Last but not least, I would like to also dedicate this thesis in part to Angus Young and AC$\not$DC. Without the music of AC$\not$DC I would not have had the ability to restrain my frustrations with graduate school.

TABLE OF CONTENTS

DEDICATION ii

ACKNOWLEDGEMENTS iii

LIST OF FIGURES vii

LIST OF TABLES x

CHAPTER

I. Top Quark Physics 1

1.1 The Standard Model of Elementary Particle Physics 1
1.2 The Top Quark 4
1.2.1 Discovery 4
1.2.2 Top Quark Production 4
1.2.3 Top Quark Properties 7
1.3 Production Cross Section 10
1.3.1 Definition 10
1.3.2 Theoretical Expectations 13
1.3.3 Other Motivation 14
1.4 Summary 15

II. Experimental Design 16

2.1 Tevatron 16
2.2 The CDF Detector 20
2.2.1 CLC 20
2.2.2 Tracking Systems 22
2.2.3 Calorimeter 26
2.2.4 Muon Detector 27
2.2.5 Online Data Acquisition 29
2.2.6 Detector Control 30
2.2.7 Offline Reconstruction 32
2.3 Data Samples 32
2.3.1 Good Run List 33
2.3.2 Final Data Sample 34
2.4 Monte Carlo Samples 34

III. Event Selection 36

3.1 The Lepton+Jets Channel . . . 36
3.2 Online Triggers . . . 38
3.3 Primary Vertex . . . 41
3.4 Tight Lepton Selection . . . 43
3.4.1 Electron Selection . . . 43
3.4.2 Muon Selection . . . 46
3.5 Jet Selection . . . 50
3.5.1 Jet Energy Corrections . . . 51
3.5.2 Plug Electron Removal . . . 53
3.6 $\not\!\!E_T$ Measurement . . . 53
3.7 Z Removal . . . 56
3.8 Dilepton Veto . . . 57

IV. B-Tagging . . . 59

4.1 Introduction . . . 59
4.2 The B-Tagging Algorithm . . . 59
4.3 The B-Tagging Efficiency . . . 63

V. The Cross Section Measurement . . . 68

5.1 Introduction . . . 68
5.2 Candidate Data Events . . . 68

VI. Event Detection Efficiency . . . 71

6.1 Introduction . . . 71
6.2 $\epsilon_{t\bar{t}}^{MC}$ . . . 72
6.3 Individual Lepton Scale Factors and Uncertainties ($\epsilon_{t\bar{t}}^{LEP-only}$) . . . 74
6.4 Common Scale Factors and Systematic Uncertainties . . . 75
6.5 Final Acceptance and Luminosity Results . . . 76
6.6 Tagging Efficiency . . . 77
6.6.1 Measurement of ϵ_{tag} . . . 78
6.6.2 Systematic Uncertainties . . . 84
6.6.3 Results . . . 86
6.7 Event Detection Efficiency Final Result . . . 86

VII. Backgrounds . . . 88

7.1 QCD . . . 88
7.2 Real W + Heavy Flavor . . . 93
7.2.1 Basic Strategy . . . 93
7.2.2 Calculation of Background Contributions . . . 96
7.2.3 $Wb\bar{b}$ . . . 97
7.2.4 $Wc\bar{c}$ . . . 99
7.2.5 Wc . . . 99
7.2.6 Corrections due to Pre-Tag $t\bar{t}$ Events . . . 100
7.2.7 Results . . . 103
7.3 Electroweak Backgrounds . . . 103
7.3.1 WW . . . 105
7.3.2 WZ . . . 107
7.3.3 ZZ . . . 108
7.3.4 $Z \to \tau\tau$ . . . 109

7.3.5 Combined Results . . . 110
7.3.6 Single Top . . . 111
7.4 Mistags . . . 112
7.5 Results . . . 114

VIII. Results . . . 117

8.1 Cross Checks in Some Interesting Variables . . . 119
8.1.1 Introduction . . . 119
8.1.2 Method . . . 121
8.1.3 Results . . . 126

IX. Optimization Studies . . . 128

9.1 Introduction . . . 128
9.2 Figures of Merit . . . 129
9.3 Optimizing the QCD Background . . . 131
9.4 Expected Signal . . . 131
9.5 Background Estimates . . . 134
9.6 Results . . . 136
9.6.1 Optimization with Level 4 Jet Corrections . . . 137
9.6.2 Optimization with Level 5 Jet Corrections . . . 139
9.6.3 Optimization with Level 6 Jet Corrections . . . 140
9.7 Conclusions . . . 140
9.8 Validity of Total Significance as a Figure of Merit . . . 141

BIBLIOGRAPHY . . . **153**

LIST OF FIGURES

Figure

1.1 Standard Model particles. Generations are arranged so that the quark with $+\frac{2}{3}$ charge is on the top in each generation (up, charm, and top quarks), and the quarks carrying a -$\frac{1}{3}$ charge are on the bottom (down, strange, bottom quarks). [14] 2

1.2 Differences in particle creation between fixed target and collider experiments. [16] 5

1.3 Production mechanisms of $t\bar{t}$ pairs at the Tevatron. The dominant production mechanism, $q\bar{q}$ annihilation is shown highlighted in the upper left-hand plot. This occurs approximately 85% of the time. The other three Feynman diagrams are from gluon fusion. 6

1.4 Visual description of parton-parton interactions in proton anti-proton collisions. [2] 6

1.5 Parton distribution functions relevant for $t\bar{t}$ production. f(x) is the probability to find a given parton with momentum x. Plotted is x·f(x) as a function of x. x_{min} is 0.18 at the Tevatron, where $q\bar{q}$ annihilation dominates as the production mechanism of $t\bar{t}$ pairs. At the collider in CERN, due to begin running in 2008, x_{min} is 0.025 and gluon fusion dominates. [2] 7

1.6 Comparison of masses of Standard Model quarks. [17] 8

2.1 Chain of Accelerators at Fermilab [36] 18

2.2 Total luminosity delivered and recorded at CDF, as a function of time [37] 19

2.3 View of the CDF Run II Detector. The solenoid is located between the Central Outside Tracker and the Electromagnetic Calorimeter. [38] 21

2.4 Schematic Drawing of Tracking Detectors in CDF [39] 23

2.5 Particles path through the detector [40] 26

2.6 Schematic of Towers in the Calorimeter [41] 28

2.7 Trigger System Flowchart for CDF. This diagram shows the maximum rate which the trigger system was designed to handle. We are currently running at a 2.5 MHz input rate into Level 1, and a 20 kHz output rate from Level 1. [42] 31

3.1 Number of Tight Jets in Lepton+Jets $t\bar{t}$ Monte Carlo Events 37

3.2 Isolation of Tight Electrons in Lepton+Jets $t\bar{t}$ Monte Carlo Events 45

3.3 P_T of Tight Muons in Lepton+Jets $t\bar{t}$ Monte Carlo Events 46

3.4 Δx between Muon Stubs and Tracks in Lepton+Jets $t\bar{t}$ Monte Carlo Events 48

3.5 Isolation of Tight Muons in Lepton+Jets $t\bar{t}$ Monte Carlo Events 49

3.6 Jet corrections applied using level 4 corrections, as a function of uncorrected jet E_T. 52

3.7 ΔR between Plug Electrons and Tight Jets in Lepton+Jets $t\bar{t}$ Monte Carlo Events 53

3.8 $\not\!\!E_T$ in Lepton+Jets $t\bar{t}$ Monte Carlo Events 54

3.9 Transverse mass of W boson in candidate electron $t\bar{t}$ events, found using information from the electron and the $\not\!\!E_T$. The world average mass of the W boson is 80.42 GeV. [64] 57

4.1 Illustration of displaced vertex 61

4.2 Typical values for the $\mid L_{xy} \mid$ (left) and $\sigma_{L_{xy}}$ (right) for taggable b-jets found in $t\bar{t}$ Monte Carlo events. 62

4.3 Illustration of positively and negatively tagged jets 62

4.4 L_{xy} of Taggable (left) and Positively Tagged (right) B-jets in Lepton+Jets $t\bar{t}$ Monte Carlo Events 63

4.5 Illustration of b-enriched sample : electron, electron-jet, away-jet 66

4.6 B-tagging Scale Factor as a function of jet E_T (GeV). Shown are the calculated scale factors for both the double tag method and the single tag method which is used as a check on the double tag. The scale factor is found to be flat across jet E_T. [7] 67

5.1 Candidate electron event with three tight jets. Two of the three tight jets are B-tagged. 70

7.1 $\not\!\!E_T$ vs Isolation space for QCD background estimate 90

7.2 Production of W+heavy flavor backgrounds via gluon splitting in real W events . . 98

7.3 Lepton + three prong decay of Z$\rightarrow \tau\tau$ 109

7.4 Two production mechanisms of single top at the Tevatron : off-shell W production (left) and W-gluon fusion (right). 111

7.5 Positive and Negative Tags, expected (open circles) versus observed (filled circles), as a function of jet E_T. [60] 115

8.1 Positively tagged data events (points) with the expected contribution from our various background sources, per jet bin. 118

8.2 Positively tagged data events (points) with the expected contribution from our various background sources. The background sources are summed into the blue line. The red line is the expected distribution of $t\bar{t}$ events found using the Standard Model theory cross section of 6.7 pb. 119

8.3 Comparisons between measured cross section results and theory predictions. Theory curves have been generated using $M_{top} = 175$ GeV. Shown are results from Run I of the Tevatron, operating under $\sqrt{s} = 1.8$ TeV, and the current results from Run II. Results from the CDF collaboration are shown in red, from D0 in blue. The circle point from Run II is from the B-tagged lepton+jets analysis, the subject of this thesis. Results from the dilepton channel cross section are marked with upside-down triangles. It is evident that the dilepton analyses are still very much statistics limited. 120

8.4 L_{xy} of B-tagged jets in Lepton+Jets candidate events in the ≥ 3 jet bin 126

8.5 Number of vertex tracks of B-tagged jets in Lepton+Jets candidate events in the ≥ 3 jet bin 127

9.1 $\triangle\phi$ vs $\not\!\!E_T$ for non-isolated lepton events in the data. The standard event selection cut of $\not\!\!E_T > 20$ GeV has already been applied. The plot on the top is for electron events. The bottom displays the distribution for muon events. As mentioned in Section 7.1, events which pass our $\not\!\!E_T$ cut but contain a non-isolated lepton are a good representation of the QCD background to the $t\bar{t}$ production cross section measurement. These figures show the majority of the QCD events exist in the region $20 < \not\!\!E_T < 30$ GeV, and $0.5 > \triangle\phi > 0$, as well as $2.5 > \triangle\phi > 3.14$. [78] . . 132

9.2 $\triangle\phi$ vs $\not\!\!E_T$ for $t\bar{t}$ events found using the ALPGEN Monte Carlo, in the ≥ 3 jet bin region. The standard event selection cut of $\not\!\!E_T > 20$ GeV has already been applied. The plot on the top is for electron events. The bottom displays the distribution for muon events. It can be seen that requiring $0.5 < \triangle\phi < 2.5$ will not affect our signal events. [78] 133

9.3 Optimization results for Level 4 jet corrections, holding $\not\!\!E_T$ and η constant and varying jet E_T. Between jet E_T of 15 and 20 GeV the total significance experiences a 2% increase, while the statistical significance remains flat. The purity increases by 15%. The signal to background experiences a significant increase of 84% as we increase the jet E_T cut to 20 GeV. 138

LIST OF TABLES

Table

1.1 Frequency (branching ratios) for the W boson to decay into the various combinations of lepton neutrino and quark anti-quark pairs 10

1.2 Frequency (branching ratios) for the two W bosons to decay into the various combinations of lepton neutrino and quark anti-quark pairs in $t\bar{t}$ events. 10

3.1 I.D and kinematic cuts for "tight" electrons, muons, and jets in the $t\bar{t}$ cross section analysis 58

4.1 Selection cuts for electrons, electron-jets, and away-jets in the B-tagging scale factor measurement 65

5.1 Candidate Events 69

5.2 Kinematic quantities for the three tight jets and tight electron in the candidate event shown in Figure 5.1. 69

6.1 Acceptance efficiency cuts for each type of lepton. Quantities are measured in a $t\bar{t}$ Monte Carlo sample. Values shown are events left after applying each cut in sequence. 73

6.2 Individual lepton efficiencies, including systematic errors 75

6.3 Final acceptance and luminosity for each lepton type. *Results do not include the tagging efficiency* 77

6.4 Efficiencies measured during this analysis for B-jets. These efficiencies are shown on a per jet and per event basis. Errors shown are strictly statistical. 81

6.5 Per-Event B-tagging Efficiency (ϵ_{B-tag}^{event}). 81

6.6 Efficiencies measured during this analysis for charm jets. These efficiencies are shown on a per jet and per event basis. Errors shown are strictly statistical. The final per-event charm jet tagging efficiency is shown in the last row, and includes both statistical and systematic errors. 83

6.7 Efficiencies measured during this analysis for non-Heavy Flavor jets. These efficiencies are shown on a per jet and per event basis. Errors shown are strictly statistical. The final per-event non-heavy flavor jet tagging efficiency is shown in the last row, and includes both statistical and systematic errors. 85

6.8 Final efficiency to tag at least one jet in a top event. 86

6.9 Final event detection efficiency. The final row in this table corresponds to the entire denominator of Equation 1.9 87

7.1 QCD background estimates for electrons and muons, found using the pre-tag data sample. Results are separated by jet bin. 92

7.2 QCD background estimates for electrons and muons, found using the tagged data sample. Results are separated by jet bin. 92

7.3 Final results for the expected contribution from the QCD background, as a function of jet bin. These final results are found by combining the results from the pre-tagged and tagged data samples, for electrons and muons separately, using a weighted average. The two weighted averages are then summed together linearly. 93

7.4 Pre-tag data events (N_W) for electrons and muons, as a function of jet bin. These numbers are used for each of the three W+heavy flavor backgrounds. 95

7.5 Heavy flavor fraction and tagging efficiency for W$b\bar{b}$ events, as a function of jet bin. Please note the tagging efficiency shown here has the scale factor of 0.86 included. (part B = $F_{WHF} \cdot \epsilon_{tag}$) 98

7.6 Results for the $Wb\bar{b}$ background, from part A of Equation 7.9. These results are presented separately for electron and muon events, as a function of jet bin. The last row in this table is the final expected background contribution from $Wb\bar{b}$ events. (part A = $N_W \cdot (1 - F_{QCD})$) 99

7.7 Heavy flavor fraction and tagging efficiency for $Wc\bar{c}$ events, as a function of jet bin. Please note the tagging efficiency shown here has the scale factor of 0.86 included. 100

7.8 Results for the $Wc\bar{c}$ background, from part A of Equation 7.9. These results are presented separately for electron and muon events, as a function of jet bin. The last row in this table is the final expected background contribution from $Wc\bar{c}$ events. 100

7.9 Heavy flavor fraction and tagging efficiency, for Wc events, as a function of jet bin. Please note the tagging efficiency shown here has the scale factor of 0.86 included. 100

7.10 Results for the Wc background, from part A of Equation 7.9. These results are presented separately for electron and muon events, as a function of jet bin. The last row in this table is the final expected background contribution from Wc events. 101

7.11 Final results for the W+heavy flavor backgrounds, after corrections for $t\bar{t}$, as a function of jet bin. 103

7.12 Components used in the calculation of the WW background, as a function of jet bin and lepton type. Final estimates for the WW background contribution are shown in the last row. 106

7.13 Components used in the calculation of the WZ background, as a function of jet bin and lepton type. Final estimates for the WZ background contribution are shown in the last row. 107

7.14 Components used in the calculation of the ZZ background, as a function of jet bin and lepton type. Final estimates for the ZZ background contribution are shown in the last row. 108

7.15 $Z \to \tau\tau$ background 110

7.16 Total expected contribution from WW, WZ, ZZ, and $Z \to \tau\tau$ backgrounds. 111

7.17 Final results for the S-Channel Single Top backgrounds, as a function of jet bin. . 112

7.18 Final results for the T-Channel Single Top backgrounds, as a function of jet bin. . 113

7.19 Final results for the Single Top background, as a function of jet bin. 113

7.20 The number of observed positive tagged events and the background summary for an integrated luminosity of $108\,\mathrm{pb}^{-1}$. The corrected total refers to the background estimate after accounting for the $t\bar{t}$ contribution to the pre-tagged W+jets data sample. 116

7.21 Monte Carlo samples used for background calculations. The W+light flavor Monte Carlo samples are used in the calculation of the heavy flavor fraction. 116

8.1 Monte Carlo samples used for background shapes. 121

8.2 Monte Carlo samples used for background shapes. Total refers to the total input Monte Carlo, before any cuts are made on the sample. Pre-Tag is the number of events left after all event selection cuts, with the exception of B-tagging, have been applied. Tag is the number of events left after the requirement that there be at least one B-tagged jet in the event is applied. Mistag backgrounds are handled differently. (See text) 123

8.3 Monte Carlo samples used for background shapes. Total refers to the total input Monte Carlo, before any cuts are made on the sample. Pre-Tag is the number of events left after all event selection cuts, with the exception of B-tagging, have been applied. Mistag backgrounds are handled differently. (See text) 123

9.1 Background estimates for our baseline analysis, using "level 4" jet corrections. (See Section 3.5.1) Results shown are for both the Iso vs $\not\!\!E_T$ and the $\Delta\phi$ methods for estimating the background contribution due to QCD. The values shown for the $Wb\bar{b}$, $Wc\bar{c}$, and Wc backgrounds have not been corrected for the expected residual $t\bar{t}$ component. 135

9.2 Background estimates for jet correction Levels 4, 5, and 6, in the ≥ 3 jet bin. Level 4 is shown both before and after $t\bar{t}$ corrections for the $Wb\bar{b}$, $Wc\bar{c}$, and Wc backgrounds. Levels 5 and 6 are shown after $t\bar{t}$ corrections only. The $\Delta\phi$ cut is applied when calculating the QCD background. All values are shown for the baseline set of cuts. (See Section 9.1) 137

9.3 Most optimal points for Level 4, Level 5, and Level 6 jet corrections. 141

9.4 Level 4 jet E_T vs MET, with $|\eta|$ held constant at 2. The most optimal point is found by increasing the jet E_T cut to 20 GeV, and not changing the MET. Numbers in italics are the baseline, bold-faced numbers are the most optimal. 143

9.5 Level 4 jet E_T vs jet $|\eta|$, with MET held constant at 20 GeV. The most optimal point is found by increasing the jet E_T cut to 20 GeV, and not changing the η cut. Numbers in italics are the baseline, bold-faced numbers are the most optimal. . . . 144

9.6 Level 5 jet E_T vs MET, with $|\eta|$ held constant at 2. The most optimal point is found by increasing the jet E_T cut to 25 GeV, holding the MET steady at 20 GeV. Numbers in italics are the baseline, bold-faced numbers are the most optimal. . . . 145

9.7 Level 5 jet E_T vs jet $|\eta|$, with MET held constant at 20 GeV. The most optimal point is found by increasing the jet E_T cut to 25 GeV, and not changing the η cut. Numbers in italics are the baseline, bold-faced numbers are the most optimal. . . . 146

9.8 Level 6 jet E_T vs MET, with $|\eta|$ held constant at 2. The most optimal point is found by increasing the jet E_T cut to 25 GeV, and not changing the MET. Numbers in italics are the baseline, bold-faced numbers are the most optimal. 147

9.9 Level 6 jet E_T vs jet $|\eta|$, with MET held constant at 20 GeV. The most optimal point is found by increasing the jet E_T cut to 25 GeV, and not changing the η cut. Numbers in italics are the baseline, bold-faced numbers are the most optimal. . . . 148

9.10 Level 5 jet E_T vs MET, with $|\eta|$ held constant at 2. The cross section used to generate our expected signal at each set of test cuts is now the measured value of 4.5 pb. It is quite clear that the most optimal point is still at jet E_T of 25 GeV, and the MET value does not change. Numbers in italics are the baseline, bold-faced numbers are the most optimal. 149

9.11 Level 5 jet E_T vs jet $|\eta|$, with MET held constant at 20 GeV. The cross section used to generate our expected signal at each set of test cuts is now the measured value of 4.5 pb. It is quite clear that the most optimal point is still at jet E_T of 25 GeV, and the MET value does not change. Numbers in italics are the baseline, bold-faced numbers are the most optimal. 150

9.12 Level 5 jet E_T vs MET, with $|\eta|$ held constant at 2. The cross section used to generate our expected signal at each set of test cuts is the Standard Model cross section of 7 pb, but we have doubled the luminosity used. As with the Level 5 study done using our current luminosity, the point which is most optimal is found by increasing the jet E_T to 25 GeV and not changing the MET. While this point has a lower statistical significance than the point at 20 GeV, the signal to background and purity are much higher, and the total significance is comparable. Numbers in italics are the baseline, bold-faced numbers are the most optimal. 151

9.13 Level 5 jet E_T vs jet $|\eta|$, with MET held constant at 20 GeV. The cross section used to generate our expected signal at each set of test cuts is the Standard Model cross section of 7 pb, but we have doubled the luminosity used. Numbers in italics are the baseline, bold-faced numbers are the most optimal. 152

ABSTRACT

Measurement of the $t\bar{t}$ production cross section in $p\bar{p}$ collisions at $\sqrt{s} = 1.96$ TeV

by
Heather L. Ray

Chair: Dante Amidei

The direct observation of the top quark was first achieved at the Tevatron proton anti-proton collider at Fermilab. This discovery completed the third generation quark sector where the top quark is expected to accompany the bottom quark in the weak isospin doublet. This dissertation will discuss the experimental verification of the production cross section as predicted by the Standard Model. A measurement of the $t\bar{t}$ production cross section using 107.9 pb^{-1} of $p\bar{p}$ collisions at $\sqrt{s} = 1.96$ TeV collected with the Collider Detector at Fermilab between March of 2003 and June of 2003 is presented. The measurement focuses on the $t\bar{t}$ production in the "lepton plus jets" final state in which one of the W bosons from the $t\bar{t}$ decay subsequently decays leptonically to an electron or a muon, and the other decays hadronically. The B-tagging technique which utilizes the precision silicon detector tracking is used to enhance the signal for $t\bar{t}$ events relative to the background through identification of the bottom quark from its measurable lifetime. The $t\bar{t}$ production cross section is measured to be $\sigma_{t\bar{t}} = 4.5 \pm 1.4$ (stat) $\pm$ 0.8 (sys) pb.

CHAPTER I

Top Quark Physics

1.1 The Standard Model of Elementary Particle Physics

The "Standard Model" is a theory of fundamental particles and their interactions. A fundamental particle is one with no internal structure. [1] Fundamental particles form the building blocks for all matter. There are two categories of fundamental particles : fermions (leptons and quarks) and bosons. The leptons and quarks comprise everyday matter. They are held together by forces, represented by the bosons.

There are a total of 6 leptons, 6 quarks, and 4 bosons in the Standard Model. There are two types of leptons : those with charge (electron (e), muon (μ), and tau (τ)), and those which are neutral (neutrinos (ν)). There is one neutrino associated with each charged lepton. Quarks are particles which have a charge of either $+\frac{2}{3}$ or -$\frac{1}{3}$. The leptons and quarks are divided into three groups, or generations. The leptons are grouped such that one charged particle and its neutrino partner are in each generation. The quarks are grouped into pairs of one $+\frac{2}{3}$ and one -$\frac{1}{3}$ quark, arranged in order of increasing mass. (See Figure 1.1) The first generation contains an electron, the electron neutrino, an up quark, and a down quark. The second generation contains the muon and the muon neutrino, and the charm and strange quarks. The tau, tau neutrino, top, and bottom quarks make up the third generation.

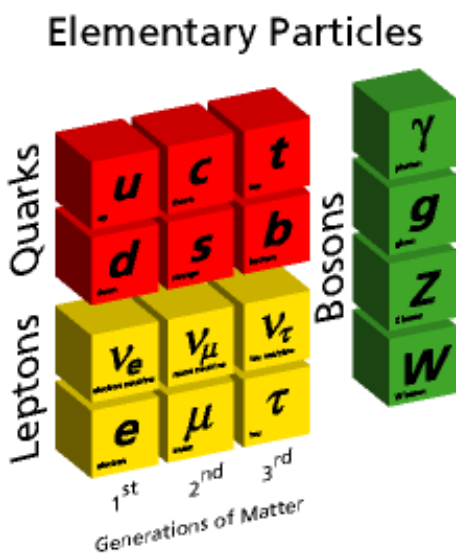

Figure 1.1: Standard Model particles. Generations are arranged so that the quark with $+\frac{2}{3}$ charge is on the top in each generation (up, charm, and top quarks), and the quarks carrying a $-\frac{1}{3}$ charge are on the bottom (down, strange, bottom quarks). [14]

Until 1975 scientists thought that there were only two generations of particles, and few took seriously the idea of there being more. In 1975 the τ lepton was first observed indirectly through the production of muon and electron events at the Stanford Linear Accelerator, at an electron-positron collider experiment. [4] These events signaled the production of a new heavy lepton that could decay to produce either electrons or muons, along with their associated neutrino. Following the trends of the other two generations, the third generation was expected to contain two additional undiscovered quarks. The charge $-\frac{1}{3}$ quark, the bottom quark, was first observed in 1977 at Fermi National Laboratory (Fermilab) through the observation of its decay products, a muon anti-muon pair.

Interactions between leptons, quarks, and bosons are dictated by the Standard Model Lagrangian (shown for the first generation only) [15] :

$$
\begin{aligned}
L = & \sum_{f=e,\nu_e,u,d} Q_f(\overline{f}\gamma^\mu f)A^\mu \\
& + \sum_{f=e,\nu_e,u,d} [\overline{f_L}\gamma^\mu f_L(T_f^3 - Q_f sin^2\theta_W) + \overline{f_R}\gamma^\mu f_R(-Q_f sin^2\theta_W)]Z_\mu \\
& + [(\overline{u_L}\gamma^\mu d_L + \overline{\mu_e L}\gamma^\mu e_L)W_\mu^+ + (\overline{d_L}\gamma^\mu u_L + \overline{e_L}\gamma^\mu \mu_{eL})W_\mu^-] \\
& + \sum_{f=u,d} \overline{q_\alpha}\gamma^\mu \lambda_{\alpha\beta}^\alpha q_\beta G_\mu^\alpha
\end{aligned}
\tag{1.1}
$$

where the subscript "L" refers to a left-handed state of the particle, which means it will exist in a doublet state (i.e. electron and electron neutrino pair, up and down quark). The subscript "R" is assigned for singlet states. Isospin, an internal coordinate of the particle which is analogous to spin, is 0 for particles in a singlet state and has an absolue value of $\frac{1}{2}$ for those in a doublet state. [21] There are constants multiplied by each of these terms which have been excluded for purposes of clarity. The first term containing A^μ is for interactions involving the electromagnetic force. The second term represents neutral current weak interactions between a particle and its own antiparticle. This interaction is mediated by the Z boson. The charged current weak interaction, mediated by the W boson, is shown in the third term. These interactions can occur between lepton neutrino pairs in the same generation, or charge -1/3 and +2/3 quark pairs. The final term, G_μ^α, describes interactions between quarks and anti-quarks, and is mediated by the gluon.

In the Standard Model quarks come in pairs, or doublets. As seen in Equation 1.1, quarks which are singlets (right-handed), with no generational partners, only interact with the Z boson. The bottom decays and couplings to the Z are different for a singlet or a doublet state. If the bottom quark were in a singlet state the width for the Z to decay into a bottom anti-bottom quark pair would be around 24 MeV. (See Section 1.2.3 for a discussion of width) If the bottom were in a doublet this value

would be around 384 MeV. The measured width of the Z decay into a $b\bar{b}$ pair is 381 MeV, proving that the bottom quark does come in a doublet state with a second quark, the top quark. [18] The top quark, if it followed the pattern of quarks in the other generations, was expected to be more massive than the bottom quark and to have a $+\frac{2}{3}$ charge.

1.2 The Top Quark

1.2.1 Discovery

The bottom quark was discovered in a fixed target experiment where highly energetic protons were directed onto a stationary atom. [5] Fixed target experiments transfer most of the energy of the incident particles into the motion of the outgoing particles which are produced, resulting in the creation of lighter particles. There had been no evidence of the top quarks' existence in accelerators up to that point. The discovery of the top quark needed to proceed in a situation where there would be more energy available for creation of heavier particles. Such conditions are met at a hadron collider, where protons and anti-protons traveling in opposite directions are made to collide head-on. (See Figure 1.2)

The top quark was first observed in 1995 at the Tevatron collider, a proton anti-proton collider ring located at Fermi National Laboratory. Discovery claims came from both experiments on the collider ring, CDF and D0. There were only $\sim$100 total top events found during this entire period of data taking which spanned 5 years (Run I).

1.2.2 Top Quark Production

$t\bar{t}$ pairs are produced at hadron colliders via the strong interaction. The two mechanisms for this production are $q\bar{q}$ annihilation and gluon fusion, as shown in

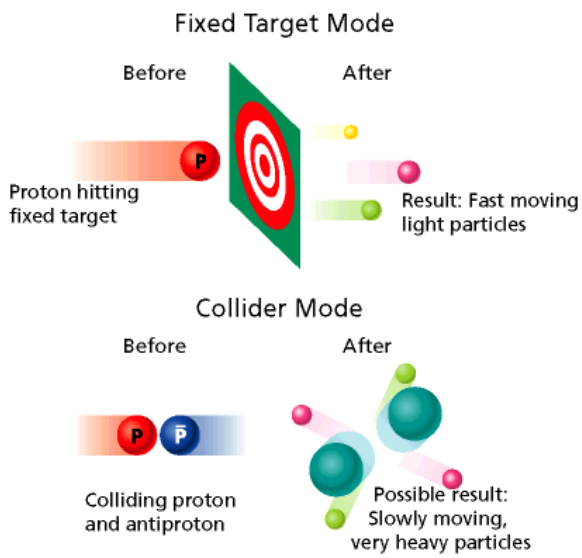

Figure 1.2: Differences in particle creation between fixed target and collider experiments. [16]

Figure 1.3.

The proton is a collection of partons, or quarks, anti-quarks, and gluons. In the parton model [21], each parton carries some fraction, x, of the protons' four momentum. (See Figure 1.4) If x_1 is the fraction of the proton four momentum carried by one parton and x_2 is the fraction of the anti-proton four momentum carried by another parton, the minimum energy required to produce a $t\bar{t}$ pair at rest is [2] :

$$x_1 \cdot x_2 \geq \frac{4 \cdot m_t^2}{s} \tag{1.2}$$

where s is the center of mass energy squared of the proton anti-proton collision. In the simple picture where the partons have equal and opposite momentum, we let $x_1 = x_2 = x_{min}$. The minimum momentum of the colliding partons which is needed to produce a $t\bar{t}$ pair is :

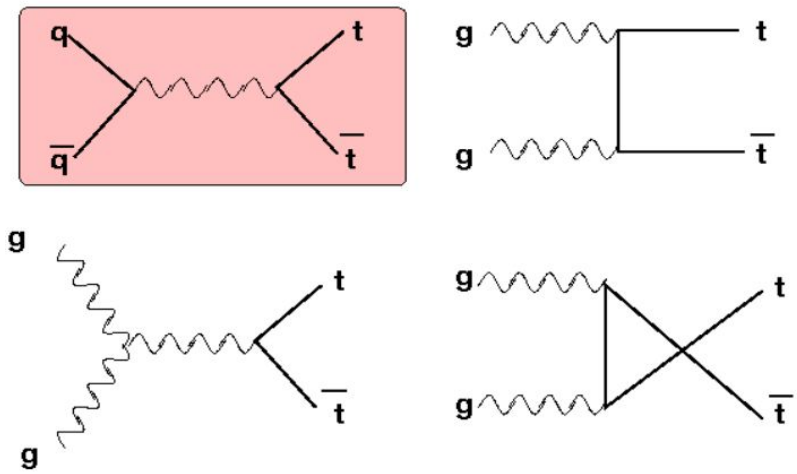

Figure 1.3: Production mechanisms of $t\bar{t}$ pairs at the Tevatron. The dominant production mechanism, $q\bar{q}$ annihilation is shown highlighted in the upper left-hand plot. This occurs approximately 85% of the time. The other three Feynman diagrams are from gluon fusion.

$$x_{min} = \frac{2 \cdot m_t}{\sqrt{s}} \tag{1.3}$$

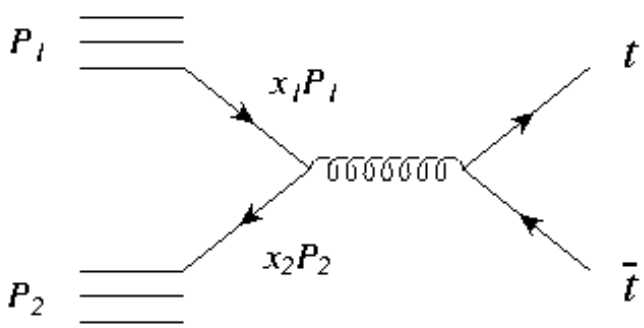

Figure 1.4: Visual description of parton-parton interactions in proton anti-proton collisions. [2]

Figure 1.5 shows the measured parton distribution functions versus x. At center of mass energies $\sqrt{s} = 1.96$ TeV x has a minimum value of 0.18. The distribution from the up and down quarks at this value of x_{min} is larger than that of the gluon. Thus, at the Tevatron, running at center of mass energies of $\sqrt{s} = 1.96$ TeV, $q\bar{q}$ annihilation

is the dominant production mechanism, occurring 85% of the time. Gluon fusion accounts for 15% of the production of $t\bar{t}$ pairs.

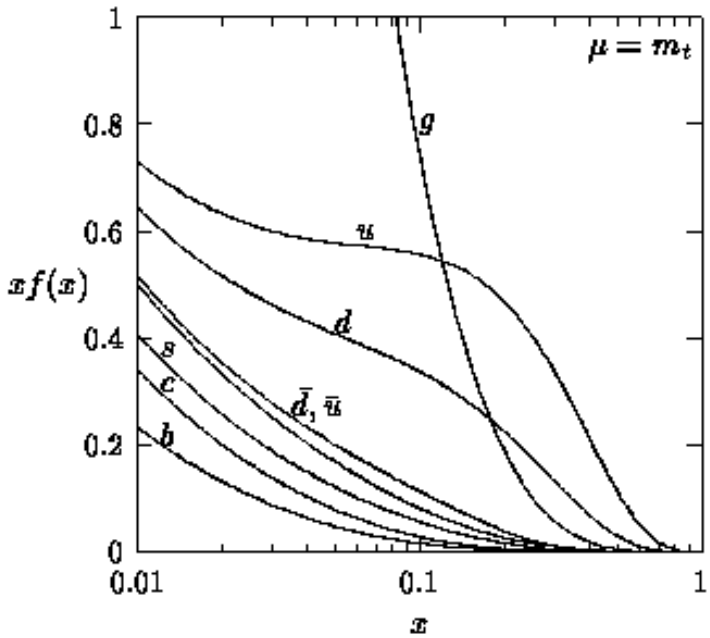

Figure 1.5: Parton distribution functions relevant for $t\bar{t}$ production. f(x) is the probability to find a given parton with momentum x. Plotted is x·f(x) as a function of x. x_{min} is 0.18 at the Tevatron, where $q\bar{q}$ annihilation dominates as the production mechanism of $t\bar{t}$ pairs. At the collider in CERN, due to begin running in 2008, x_{min} is 0.025 and gluon fusion dominates. [2]

1.2.3 Top Quark Properties

Mass

The top quark mass has been measured to be ∼175 GeV/c^2. [12] Its next nearest neighbor in mass is the bottom quark, which is ∼35 times less massive.(See Figure 1.6) In the Standard Model particles gain mass through electroweak symmetry breaking, brought about by the introduction of the Higgs boson (field) into the theory. Fermions gain mass through their Yukawa coupling to the Higgs field [2] :

$$M_{ij} = \Gamma_{ij} \cdot \frac{v}{\sqrt{2}} \tag{1.4}$$

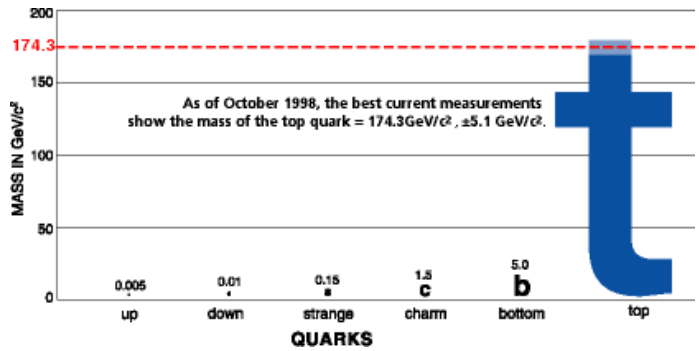

Figure 1.6: Comparison of masses of Standard Model quarks. [17]

where M_{ij} is the mass of the charged fermion (quark or lepton), Γ_{ij} is the Yukawa matrix parameter for the given fermion, and v is the vacuum expectation value of the Higgs field, approximately 246 GeV. The mass of the top quark and the value of v suggest that the top Yukawa coupling is 1.01. Thus, the top quark is strongly coupled to the Higgs boson.

Lifetime and Width

The Uncertainty Principle, $\triangle E \triangle t = \hbar$, expresses a linear relationship between the spread in energy of a given particle state and the time the particle will spend in that state. The energy spread of a decaying state is the width of the particle, Γ, and the time spent in a given state is the lifetime, τ. The width of a particle is directly related to the reaction rate (W) of the particle [6] :

$$\Gamma = \hbar \cdot W$$
$$W = \frac{2 \cdot \pi}{\hbar} \cdot \mid M_{if} \mid^2 \rho_f \tag{1.5}$$

where M_{if} is the matrix element connecting the initial and final states of the particle, and ρ is the energy density of the final states. For the top quark with a mass of 175 GeV the width, Γ_t, is approximately 1.5 GeV. [6]. Using the width of

1.5 GeV and the Uncertainty Principle, the lifetime of the top quark is calculated to be approximately 4x10^{-25} seconds.

Hadronization is the process by which a "free" or unbound quark combines with another one or two free quarks to form a bound state called a hadron. The timescale for QCD hadronization is on the order of 10^{-23} seconds, much longer than the top lifetime. The top quark is the only Standard Model quark which is unable to hadronize, and it decays at the point of creation.

Decays

Particles decay in the Standard Model through mixing with other quarks. This mixing is mediated by the W and Z gauge bosons (See Equation 1.1). The large mass of the top quark in relation to the Z boson mass makes coupling to an anti-top quark and the Z boson impossible. The top quark decays via the charged current weak interaction ($W^{\pm}$), coupling to a W boson and either a bottom, strange, or down quark. The decay of top into a W boson and a bottom quark occurs ~100% of the time. The top mass is much larger than the W boson, allowing the top to couple with a real, on-mass shell W boson.

W bosons decay into a lepton neutrino pair, or into a quark anti-quark pair. The frequency with which a W will decay into the various lepton neutrino or quark anti-quark pairs is shown in Table 1.1. The three ways to categorize a $t\bar{t}$ event are based on the way in which the two W bosons in the event will decay. These are : dilepton, in which both W's decay into a lepton neutrino pair, all-jets (hadronic), in which both W's decay into a $q\bar{q}$ pair, and lepton+jets, when one W decays into a lepton neutrino pair and the other W decays into a quark anti-quark pair. The branching ratios for these various combinations of $t\bar{t}$ events to occur are shown in Table 1.2.

W Decay	Branching Ratio
$e^+ \nu_e$	1/9 : 0.11
$\mu^+ \nu_\mu$	1/9 : 0.11
$\tau^+ \nu_\tau$	1/9 : 0.11
u $\overline{d}$	3/9 : 0.33
c $\overline{s}$	3/9 : 0.33

Table 1.1: Frequency (branching ratios) for the W boson to decay into the various combinations of lepton neutrino and quark anti-quark pairs

W_1 Decay	W_2 Decay	Branching Ratio
Dilepton Channel		
e ν	e ν	1/81 : 0.012
e ν	μ ν	2/81 : 0.025
e ν	τ ν	2/81 : 0.025
μ ν	μ ν	1/81 : 0.012
μ ν	τ ν	2/81 : 0.025
τ ν	τ ν	1/81 : 0.012
Total		0.111
All-Jets Channel		
$q\overline{q}$	$q\overline{q}$	36/81 : 0.444
Lepton+Jets Channel		
e ν	$q\overline{q}$	12/81 : 0.148
μ ν	$q\overline{q}$	12/81 : 0.148
τ ν	$q\overline{q}$	12/81 : 0.148
Total		0.444

Table 1.2: Frequency (branching ratios) for the two W bosons to decay into the various combinations of lepton neutrino and quark anti-quark pairs in $t\overline{t}$ events.

1.3 Production Cross Section

The first task in an experimental top physics program is to create $t\overline{t}$ pairs and to verify that they are made as expected. The measure of a particles' production rate is usually expressed in terms of the production cross section, σ.

1.3.1 Definition

The cross section is a measure of the probability for a certain process to occur. The cross section per target particle is a function of the beam flux and the production rate :

$$\sigma = \frac{W}{\phi} \tag{1.6}$$

where W, the reaction rate per target particle, is given in Equation 1.5, and ϕ is the flux of particles per unit area per unit time. The flux is defined as :

$$\phi = n_{incident} \cdot v_i \tag{1.7}$$

or, the density of particles in the incident beam, times the velocity of the incident beam relative to the target. The reaction rate, W, is essentially the number of observed processes (N). Luminosity is the equivalent of particle flux for colliding beams. Luminosity is essentially the number of particles which "see" other particles, per area, per time. For two oppositely directed beams of particles the luminosity is defined as :

$$L = f \cdot n \cdot \frac{N_1 \cdot N_2}{A} \tag{1.8}$$

where f is the revolution frequency of the beams, n is the number of bunches in the beam over the entire circumference of the accelerating ring, A is the cross sectional area of the beams, and N_1 and N_2 are the number of particles in each bunch. [6] Luminosity is measured in units of inverse barns, where one barn = $10^{-28}\ meters^2$.

Experimentally there are many different physics processes which will result in the same event signature. N, the number of observed processes, is really the number of observed events which have a signature similar to that from the process under study. N comprises events from the process you wish to study (in our case $t\bar{t}$ events), as well as events from these other sources. These other processes are called "backgrounds".

Experimentally one also needs to take into account the efficiency of the detector for capturing and recording the intended events. An additional term is included in the denominator of the cross section equation, for the event detection efficiency. The efficiency is the probability that a $t\bar{t}$ pair produced during collisions has passed all of the selection cuts and has been found in the detector.

The $t\bar{t}$ production cross section is measured using :

$$\sigma_{t\bar{t}} = \frac{N_{obs} - N_{bgd}}{\epsilon_{t\bar{t}} \cdot \int L dt} \tag{1.9}$$

i.e., it is the number of observed candidate events minus the prediction for observed events coming from background, or fake, sources, divided by the product of the event detection efficiency and the integrated luminosity of the data sample. [7], [8]

The cross section can be measured in three different channels characterized by the final decay products of the W bosons. All three channels were used in Run I to claim discovery. When deciding to undertake a cross section measurement it is prudent to choose the channel with a highest amount of statistics and lowest backgrounds, or physics process that can fake the signature.

Tau leptons as themselves are very difficult to observe. Taus also are capable of decaying into electrons and muons. When comparing the three channels we exclude taus from consideration of the branching ratios. The dilepton channel has a very low background rate but a branching ratio of 5%, making this a very statistics limited measurement. The all-jets channel has the highest branching ratio of all three channels, 40%, but is extremely background laden from QCD jet events. The final channel for consideration, the lepton+jets channel, has a branching ratio of 35%. This channel has a large background from real W plus multi-jet events. We can reduce the backgrounds in the lepton+jets channel by identifying the jets associated

with the decay of the bottom quark. (See Section IV) B-tagging allows us to increase our signal to background ratio from ~0.5 to 2. The leptons+jets channel with B-tagging offers a large amount of statistics with a manageable background. This thesis describes the measurement of the $t\bar{t}$ B-tagged lepton+jets cross section.

1.3.2 Theoretical Expectations

The cross section for a process to occur is illustrated in Equation 1.6. Using Equation 1.5 for the reaction rate and Equation 1.7 for the flux, we find in the center of momentum system (cms) of the reaction [6] :

$$\begin{aligned} \frac{d\sigma}{d\Omega} &= \frac{W}{\phi_i} \\ &= \frac{W}{v_i} \\ &= \frac{2 \cdot \pi}{\hbar \cdot v_i} \cdot \mid M_{if} \mid^2 \rho_f \\ &= \frac{2 \cdot \pi}{\hbar \cdot v_i} \cdot \mid M_{if} \mid^2 \cdot \frac{1}{(2 \cdot \pi \cdot \hbar)^3} \cdot p_f^2 \cdot \frac{dp_f}{dE_0} \end{aligned} \tag{1.10}$$

where the p_f is the cms momentum of each of the final state particles, and E_0 is the total cms energy. Here i and f refer to the initial and final states of the colliding particles, respectively. Conservation of energy requires that $\frac{dp_f}{dE_0} = \frac{1}{v_f}$, giving a final cross section of :

$$\frac{d\sigma}{d\omega} = \frac{1}{4 \cdot \pi^2 \cdot \hbar^4} \cdot \mid M_{if} \mid^2 \cdot \frac{p_f^2}{v_i \cdot v_f} \tag{1.11}$$

Protons, however, are comprised of partons. The cross section for a parton-parton collision requires the matrix elements include a term for the frequency with which the various partons carry a fraction x of the proton momentum. (See Section 1.2.2) This is expressed through the use of structure functions, F [19] :

$$\sigma \sim \int \mid M_{12} \mid^2 \cdot F_1 \cdot F_2 \tag{1.12}$$

where 1 and 2 are the indices of the colliding partons.

Calculation of the theoretical value of the cross section is carried out using perturbative QCD. At the lowest order there are two parton-parton subprocesses which produce $t\bar{t}$ pairs, $q\overline{q}$ annihilation and gluon fusion. (Section 1.2.2) Next-to-leading order, NLO, contributes the following processes to $t\bar{t}$ pair production :

- $q + \overline{q} = t + \bar{t} + g$
- $g + g = t + \bar{t} + g$
- $g + q = t + \bar{t} + q$
- $g + \overline{q} = t + \bar{t} + \overline{q}$

The gq and $g\overline{q}$ channels are negligible, but the $q\overline{q}$ and gg channels should be included in theoretical calculations. The radiative corrections attributed to the gg channel are numerically as important as the lower order cross section contributions. [22] The current theoretical calculation of the $t\bar{t}$ production cross section measurement at center of mass energy of $\sqrt{s} = 1.96$ TeV, with a top quark mass of 175 GeV, is approximately 6.7±0.9 pb. [20]

Results of the cross section measurements from Run I, where $\sqrt{s} = 1.8$ TeV, (5.1 ± 1.5 pb) showed no significant deviations from theory (4.75 to 5.5 pb) [12].

1.3.3 Other Motivation

QCD Standard Model theory predicts the production rate expected from $t\bar{t}$ pairs, given a mass of the top quark and the center of mass energy of the colliding beams. Any departures in the cross section measurement from these QCD predictions could indicate non-standard production mechanisms or couplings of the top quark.

Predictions for the cross section production rate are calculated to first order. Non-QCD radiative corrections would change the expected $t\bar{t}$ production rate. Non-QCD radiative corrections are predictions for the production processes of $q\bar{q}$ annihilation and gluon fusion carried out beyond the leading order calculations. For example, electroweak radiative corrections to the cross section can cause an enhancement of up to 30% in the observed production rate. [9]

The cross section could float high due to production from decays of heavy resonant states, or from anomalous couplings. If anomalous top quark couplings exist they will affect the top production and decay at high energies as well as precisely measured quantities with virtual top quark contributions, such as the W and Z masses. Overall we would expect a small effect in the observed cross section measurement due to these couplings. [9]

1.4 Summary

This analysis focuses on the $t\bar{t}$ production cross section measurement, in the B-tagged lepton+jets channel. An introduction to the experimental apparatus used in obtaining our candidate events is found in Chapter II. Chapters III and IV detail the selection criterion placed on candidate events. A discussion of the candidate events found in the data can be found in Chapter V. The primary components of the cross section measurement, the event detection efficiency and the background calculations, may be found in Chapters VI and VII, respectively. Final results of the $t\bar{t}$ production cross section measurement in the lepton+jets channel are presented in Chapter VIII. Finally, a study of the optimization of the cross section is presented in Chapter IX.

CHAPTER II

Experimental Design

2.1 Tevatron

The Tevatron is a proton-anti-proton accelerator located in Batavia, Illinois, at Fermi National Accelerator Laboratory (Fermilab).

Fermilab is a complex comprising several smaller accelerators and storage rings, which serve two main purposes. The accelerators supply particle beams to fixed target experiments, and they supply protons and anti-protons to the Tevatron colliding ring. (See Figure 2.1) Negatively charged hydrogen gas is produced in the magnetron, located inside the Cockcroft-Walton pre-accelerator. These ions are accelerated to an energy of approximately 750 keV before being sent into a linear accelerator. There the ions are accelerated to 400 MeV and sent through a carbon foil. The carbon foil traps the electrons attached to the ions and permits protons to pass on to the next step, the Booster Ring. In the Booster Ring the protons are accelerated until they reach peak energies of 8 GeV. The Main Injector accepts these protons and continues the acceleration process, increasing their energy to 150 GeV. In addition, the Main Injector accelerates a portion of the protons to 120 GeV for use in anti-proton production.

The 150 GeV protons from the Main Injector are delivered to the Tevatron ring.

The Tevatron is a superconducting proton anti-proton synchrotron located in a circular tunnel 4 miles in circumference, around which the protons and anti-protons travel. Various magnets placed around the ring bend, accelerate, and collimate the beams of particles. It is here that the particles are accelerated to their final energies of approximately 1 TeV (Tera-electronvolt) each, supplying collisions with center of mass energies ($\sqrt{s}$) of 1.96 TeV. Thirty-six bunches of protons (anti-protons) are distributed around the circumference of the ring which houses the Tevatron. For this reason the collisions are "36x36", i.e. 36 bunches of protons collide with 36 bunches of anti-protons. One bunch of protons collides with one bunch of anti-protons every 396 nanoseconds. The Tevatron is currently the worlds' highest energy collider.

Protons earmarked for use in anti-proton production are sent from the Main Injector to the anti-proton source where they collide with a nickel target. The secondary particles produced in these collisions are, in part, anti-protons. The collisions of the protons with the target cause the resulting anti-protons to have a large momentum spread. This momentum spread will lead to a large emittance of the anti-proton beam. The emittance is related to the luminosity of the beam by expanding Equation 1.8 :

$$L = f \cdot n \cdot \frac{N_1 \cdot N_2}{2 \cdot \pi \cdot \sqrt{\epsilon_p \cdot \epsilon_{\overline{p}}}} \tag{2.1}$$

where the ϵ are the emittance of the proton and anti-proton beams.

After creation the anti-protons are stored in the Accumulator ring. The process of "stochastic cooling" is introduced to reduce the momentum spread of the anti-proton beam. [43] When the intensity and emittance of the anti-protons meets the minimum requirements for collisions they are sent back into the Main Injector, to be accelerated and injected into the Tevatron. [23]

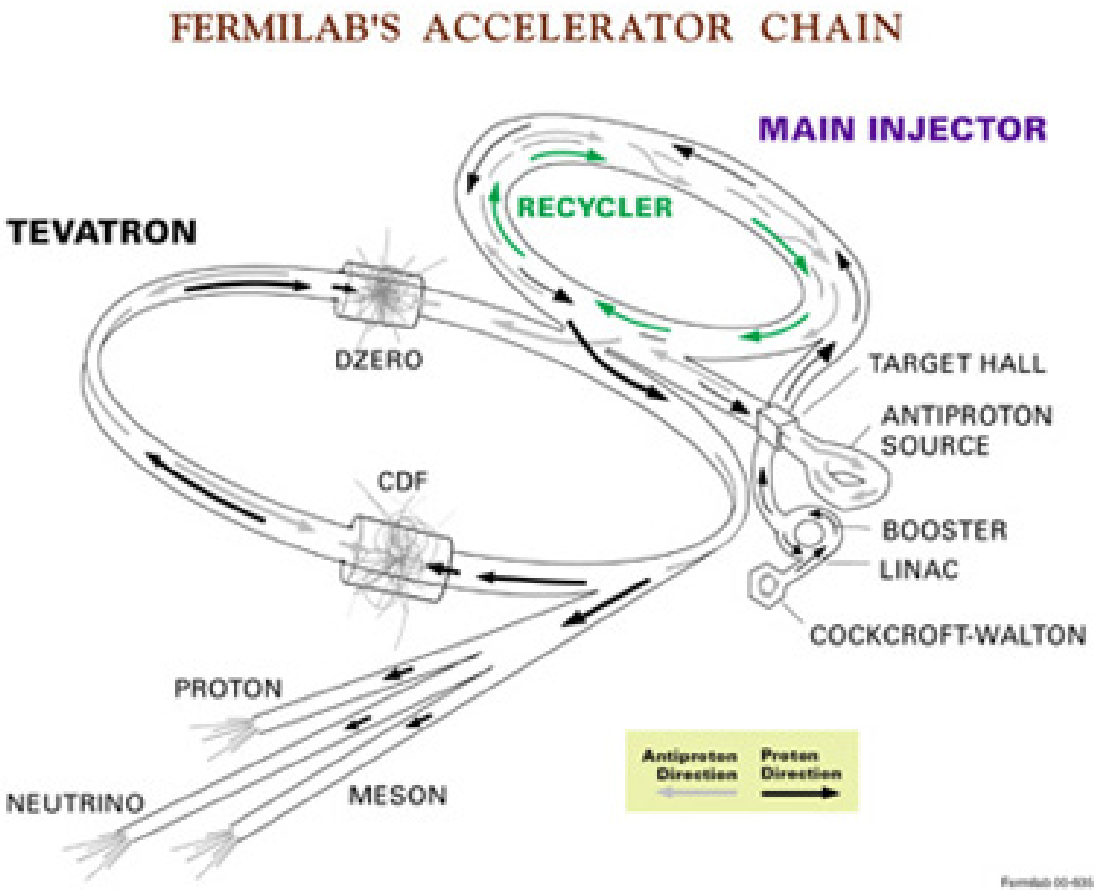

Figure 2.1: Chain of Accelerators at Fermilab [36]

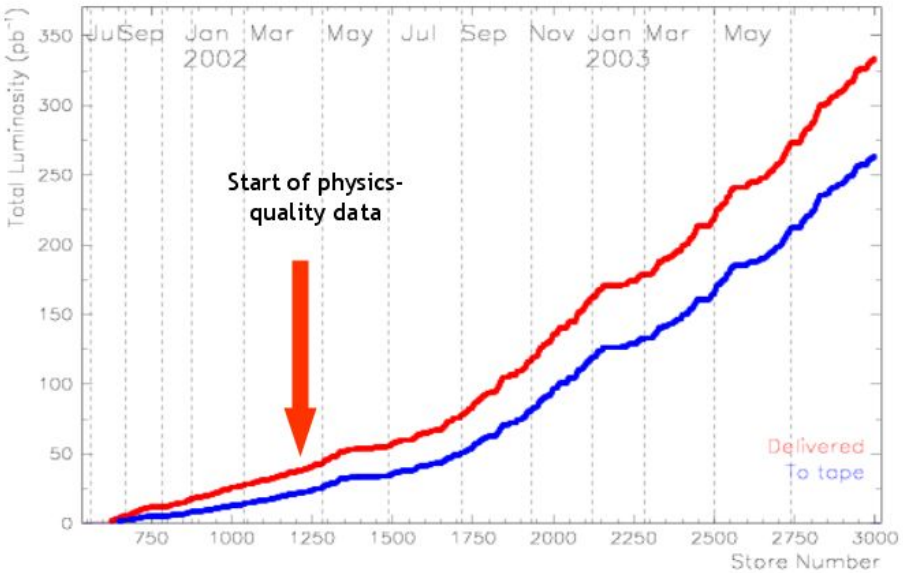

Figure 2.2: Total luminosity delivered and recorded at CDF, as a function of time [37]

There are two general purpose detectors at the Tevatron : the Collider Detector at Fermilab (CDF) and D0. Quadrapole magnets focus the proton and anti-proton beams so that they collide in the center of each of these detectors. The data used for this thesis were recorded at the CDF detector.

The amount of data received at the detector (and thus used in an analysis) is quantified in terms of the luminosity. (See Section 1.3.1) The average instantaneous luminosity of data runs used in this analysis is 2.0 x 10^{31} per cm^2, per second. At the time of writing the record instantaneous luminosity seen at CDF is 4.2 x 10^{31} per cm^2, per second. Since the start of physics-quality data taking at CDF in April, 2002, the Tevatron has delivered a total of 330 pb^{-1} to CDF, of which 200 pb^{-1} is declared to be good for analysis. (See Figure 2.2)

2.2 The CDF Detector

CDF is a general purpose detector containing several sub-detectors which identify a variety of particles. The detector is cylindrical in shape, with the beampipe running through the center of the detector along the z axis. The beampipe which houses the circulating particles is approximately 1 centimeter in radius at the interaction points. Collisions take place in the center of the detector. The coordinate system of CDF measures the azimuthal angle ϕ from the plane of the Tevatron, and polar angle θ from the proton direction, which is traveling from west to east through the detector. The angle θ is not invariant under boosts in the z-direction. There is a unit of measure, the pseudo-rapidity (η), which transforms linearly under boosts in the z-direction, and which is related to θ by [29] :

$$\eta = -ln(tan(\frac{\theta}{2})) \tag{2.2}$$

$\mid \eta \mid$ extends from 0 at the perpendicular to the beampipe to approximately 3.5 at the most forward part of the detector. (See Figure 2.4) The central portion of the detector spans $0 \leq \mid \eta \mid \leq 1$, while the forward(plug) detector is located at $1 \leq \mid \eta \mid \leq 3$. Sub-detectors are placed radially at varying distances from the collision point. Starting from the beampipe and expanding outward one finds the tracking systems, calorimetry systems, and muon systems. (See Figure 2.3)

2.2.1 CLC

The Cerenkov Luminosity Counters (CLC) are located inside 3 degree holes in the endplug calorimeters. [24] These monitors accomplish three jobs : they provide monitoring of beam data at CDF for the Tevatron operators, they provide on-line luminosity monitoring to CDF, and they provide off-line luminosity measurements for

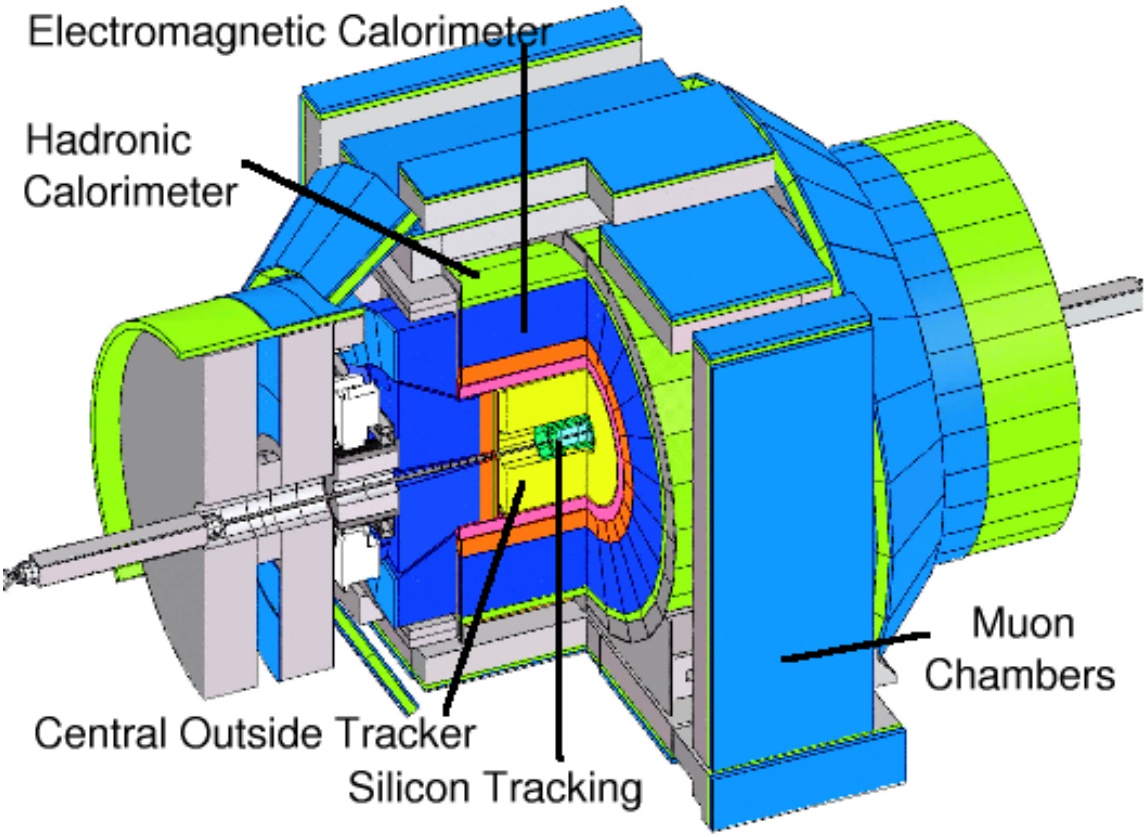

Figure 2.3: View of the CDF Run II Detector. The solenoid is located between the Central Outside Tracker and the Electromagnetic Calorimeter. [38]

CDF physics. The CLC records information on the individual bunch luminosities, the total instantaneous luminosity of the Tevatron, and the total integrated luminosity of the Tevatron. [25] This is done by measuring the average number of interactions per beam crossing, and using this information to calculate the luminosity [26] :

$$Luminosity = \frac{f \cdot \mu}{\epsilon_{CLC} \cdot \sigma_{p\overline{p}}} \tag{2.3}$$

where f is the frequency of bunch crossings, μ is the measured average interactions per crossing, ϵ_{CLC} is the CLC acceptance, and $\sigma_{p\overline{p}}$ is the total proton anti-proton interaction cross section.

2.2.2 Tracking Systems

Tracking detectors record the path of charged particles through the detector. CDFs tracking systems are contained inside a solenoid magnet (located between the Central Outside Tracker and the Electromagnetic Calorimeter in Figure 2.3). The solenoid produces a 1.4 Tesla magnetic field which runs parallel to the beam axis. The tracking detectors are arranged in the following order: the SVX (Silicon VerteX detector) extends from a radius of 2.4 to 10.7 cm, the ISL (Intermediate Silicon Layer) from 20 to 28 cm, and the COT (Central Outside Tracker) from 44 to 132 cm. (See Figure 2.4)

The SVX provides precision tracking information at the smallest possible radii. Information recorded in the SVX is used to reconstruct secondary vertices which come from heavy-flavor particle decays, such as bottom and charm hadrons. This is crucial for the B-tagging algorithm which is used in this thesis (Chapter IV). This detector provides tracking out to a pseudo-rapidity value of $\mid \eta \mid < 2.0$. The detector consists of three cylindrical barrels, each barrel comprising five concentric

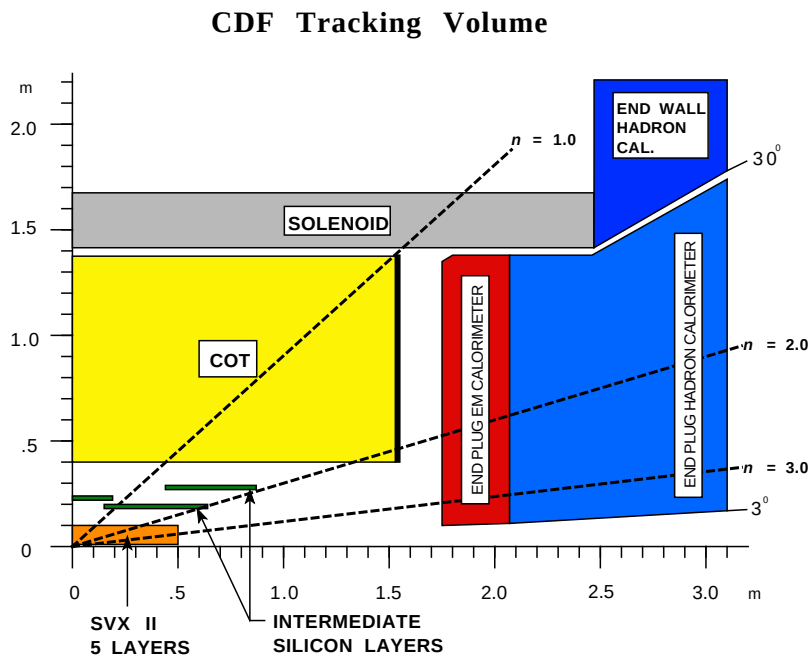

Figure 2.4: Schematic Drawing of Tracking Detectors in CDF [39]

layers of silicon microstrip detectors. These sensors are double sided. Sensors in all five layers have one side which carries out measurements in the r-ϕ plane. On three of the five layers the other side contains sensing strips, running perpendicular to the axial direction. This provides measurements in the r-z plane, or "90 degree stereo" measurements. The other two layers have a second side which has sensing strips which are tilted at an angle of 1.25 degrees in relation to the first set. This provides "small angle stereo" measurements. The stereo measurement in principle allows for excellent z-position measurements of secondary vertices. The z-position measurements are not used here, but will be implemented in future analyses. The impact parameter resolution achieved with the SVX, averaged over all $t\bar{t}$ decay tracks, is 24.8 μm. [44]

The ISL detector consists of three layers of concentric silicon strip detectors, located outside of the SVX detector. In the central portion of the detector there is one layer placed at 22 cm from the interaction point. The other two layers are

positioned at the same $\mid \eta \mid$ as the plug region of the detector, at distances of 20 and 28 cm. The ISL is used to improve the efficiency of 3-D tracking in the central region, and to add coverage in the forward region. These sensors are similar to those found in the SVX. One side allows for axial, or r-ϕ measurements, while the other has small angle capabilities. The SVX and ISL provide CDF with the ability to do stand-alone silicon tracking and B-tagging out to $\mid \eta \mid \leq 2$.

The COT detector is a drift chamber located in the central portion of the detector ($\mid \eta \mid < 1$), outside of the two silicon detectors. [10] There are 96 sense layers in the COT, grouped into 8 "superlayers" of 12 measurements each. There are 4 superlayers running parallel to the beampipe, providing $r - \phi$ information. The other sets of wires are placed at a 2 degree tilt to the z plane, providing stereo information. The chamber is filled with an Argon-Ethane-CF_4 gas mixture. Charged particles which pass through the drift chamber leave a trail of ionization along their path. Field shaping via cathode planes causes electrons to drift to the sense wires. The avalanche on the wire is registered as a pulse, and the drift time can be converted into a distance of closest approach of the particle to the wire. These distances allow for 3-D reconstruction of the path of a charged particle. The average drift velocity for the COT detector is $100\frac{\mu m}{ns}$. The average resolution per wire is 180 μm. [10]

The strong magnetic field inside the COT causes the charged particle to move in a helical path through the detector. [10] From the radius of the path it is possible to calculate the transverse momentum (P_T) of the particle [30]:

$$\begin{aligned} \alpha \cdot v_T \cdot B &= m \cdot \frac{v_T^2}{r} \\ r &= \frac{m \cdot v_T}{\alpha \cdot B} \\ &= \frac{P_T}{\alpha \cdot B} \end{aligned} \tag{2.4}$$

where α is a constant term, r is the radius of the path, B is the strength of the magnetic field which surrounds the tracking chambers, and the r is related to the curvature (C) through :

$$r = \frac{1}{2 \cdot C} \tag{2.5}$$

$$\begin{aligned} P_T &= r \cdot \alpha \cdot B \\ P_T &= \frac{\alpha \cdot B}{2 \cdot C} \end{aligned} \tag{2.6}$$

The trajectory of a charged particle through a uniform magnetic field is a helix. The projection of this trajectory onto the $r - \phi$ plane is a circle. COT measurements are primarily in the $r - \phi$ plane, so tracks are found in this detector by fitting to a circle [46] :

$$R = \frac{c \cdot B}{P_T} \tag{2.7}$$

where R is the radius of the circle, B is the magnetic field, and P_T is the transverse momentum of the particle (track). Once a track has been found in the $r - \phi$ plane, the stereo (z) position information from the COT is attached to make 3-D tracks. [47] The momentum resolution of the COT, $\frac{\delta_{P_T}}{P_T^2}$, is approximately 0.3% $(\frac{GeV}{c})^{-1}$. [10]

Silicon hits are attached to the COT tracks using an "outside-in" algorithm. Starting with a hit in the r-ϕ plane of the COT detector tracks are extrapolated back into the silicon detectors. At each step of the extrapolation multiple scattering considerations determine the region in which the algorithm looks for a track. Once a

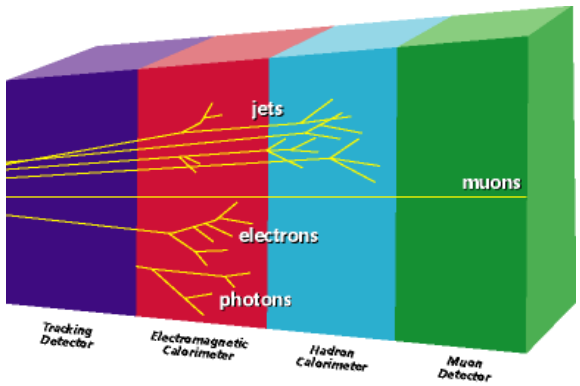

Figure 2.5: Particles path through the detector [40]

reconstructed track is found in the r-ϕ plane, z position information from the silicon detector is added to the track. This allows the track to be assigned a point of origin along the z axis (z0). [31]

2.2.3 Calorimeter

The tracking systems are contained inside of a magnetic field. Located just outside of the magnetic field is the calorimeter. The calorimeter is divided into two segments, each measuring a specific type of energy deposition. The first section of the calorimeter is the EM (electromagnetic), which is used primarily for the identification of electrons and photons. The second component is the HAD (hadronic), and is where high-energy jets deposit the majority of their energy. (See Figure 2.5)

High energy electrons and photons lose energy in the form of electromagnetic radiation caused by bremsstrahlung. One radiation length for these particles is the mean distance over which the particle loses all but $\frac{1}{e}$ of its energy. It is more appropriate to discuss the construction of the calorimeter in terms of radiation lengths instead of using standard units of thickness. The EM detector contains 23 layers of alternating lead and scintillator for a total of 21 radiation lengths of thickness. The E_T resolution of the EM calorimeter is approximately $\frac{16\%}{\sqrt{E}}$. [10] The first layer of the

EM calorimeter is made of a thicker scintillator and wire chamber which acts as a pre-shower detector (CPR). Located at a depth of approximately 6 radiation lengths is the Shower Max detector (CES). The Shower Max is a position detector used to match tracks found in the tracking systems to calorimeter energy deposits.

Instead of radiation lengths we describe the hadronic calorimeter in terms of nuclear absorption lengths. The HAD detector is made of 23 layers of iron and scintillator. The central HAD calorimeter is approximately 4.5 absorption lengths in thickness. The plug HAD calorimeter is 7 absorption lengths thick.

The calorimeter is made up of wedges, or "physical towers", measured in $\eta - \phi$ coordinates. Each tower uses a series of absorber and scintillator layers. Scintillator light is collected by a light pipe and a wavelength shifter that directs the energy into a photomultiplier tube. An r-z view of the detector shows the calorimeter wedges arranged as if a pie cut into slices, with each slice pointing back toward the interaction point. (See Figure 2.6) The central portion of the calorimeter has towers that span 15 degrees in ϕ and 0.11 in units of η, while the plug calorimeter towers span either 15 or 7.5 degrees in ϕ, and varying ranges in η.

2.2.4 Muon Detector

The muon detectors are located outside of the calorimeter, at the furthest reaches of the detector. Muons are minimum ionizing particles, which means they are capable of traveling through many interaction lengths before losing their energy and stopping. CDF uses the steel in the calorimeter, the magnet return yoke, and additional steel shielding to stop all other charged particles from entering the muon detectors. The muon chambers record hits from the path of the muon through the detector. This information, combined with tracks in the COT, results in an excellent muon identification.

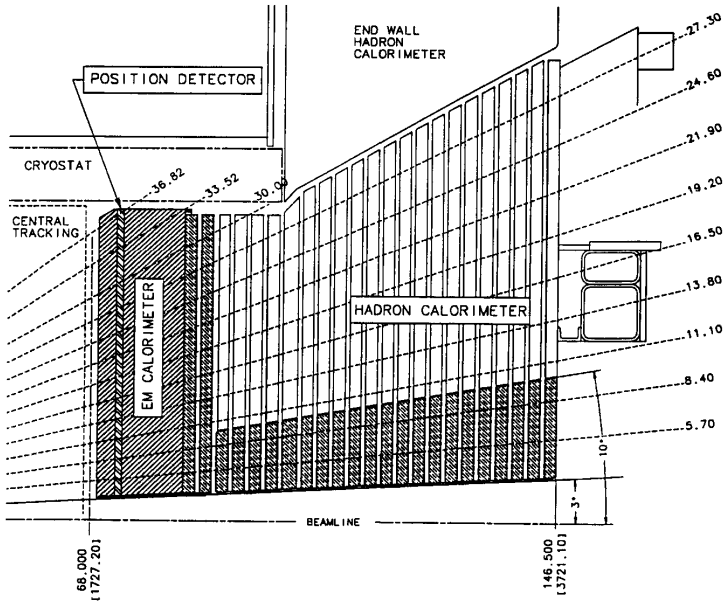

Figure 2.6: Schematic of Towers in the Calorimeter [41]

The muon detectors are four systems of scintillators and proportional wire chambers which extend out to $|\eta| \leq 2.0$. They are, moving outward from the interaction point, the CMU (Central MUon), CMP (Central Muon uPgrade), CMX/CSX (Central Muon eXtensions), and the IMU (Intermediate Muon System) detectors. The CMU and CMP extend out to $|\eta|$ of 0.6, the CMX spans a range of $0.6 \leq |\eta| \leq 1.0$, and the IMU finalizes the coverage from $1.0 \leq |\eta| \leq 2.0$.

The CMU are the original set of muon chambers which were used in Run I. They are located behind the central HAD calorimeter, which provides approximately 5.5 absorption lengths of material for muons. The CMP detectors are a fixed length in z, vary in η, and form a box around the CMU. They are located behind an additional 60 cm of steel absorber. The central muon extension detectors are located at each end of the central detector and range from $42 \leq \phi \leq 55$ degrees. They are actually two types of detectors - the CMX uses drift tubes to identify particles, and the

CSX uses scintillating counters. No additional absorbing material was added for this detector. The hadron calorimeter, magnet return yoke, and steel of the detector support structure supply more absorber for the CMX than for either the CMU and CMP. The IMU triggers on muons out to an $\mid \eta \mid$ value of 1.5 online during data taking, due to constraints on tracking. Muon objects are found by identifying stubs, or hits in at least 4 layers of the muon chambers which lie in a straight path through the detectors.

2.2.5 Online Data Acquisition

Collisions currently occur in the detector at a rate of approximately 2.5 MHz. The average event size is 250 kilobytes. With events occurring every 396 nanoseconds, our bandwith is 0.63 Tb per second. This is an extremely large rate, and the amount of disk space needed to store all of this information would be overwhelming. To reduce the amount of data stored on disk we implement an online selection, the trigger.

The detectors are read out into a three-tiered trigger system. Our trigger system is a deadtime-less trigger, with total trigger deadtime typically on the order of $\leq 5\%$. This means that the detector misses a collision due to latency in the online triggering and readout systems less than 5% of the time. Each level of trigger provides rate reduction and a pipeline for sequential event storage in order for there to be minimal deadtime. (See Figure 2.7)

At each level the trigger electronics examine the data to see if basic sets of requirements are met for an event to be considered interesting physics. Triggers are sets of requirements which are based on the identification of particles and their measured kinematics. (See Section 3.2 for a discussion of triggers used in this analysis) The Level 1, Level 2, and Level 3 trigger requirements are combined into a logical unit called a Trigger Path. Trigger Tables are made up of many Trigger Paths, to cover

the wide range of physics interests at CDF. We have many different trigger tables, each providing a different functionality.

Level 1 can make a decision to accept or reject an event based on calorimeter energy, muon depositions, or track information. At this stage the data rate is reduced from 2.5 MHz down less than 20 kHz. Level 2 currently provides rejection based on calorimeter energy and track information. Level 2 differs from Level 1 in that it is programmable. Level 2 combines information from all detector systems, with a processing time of 20 μs per event. Level 2 has access to data from the Shower Max for improved identification of electrons and photons, and jet reconstruction through a cluster finding algorithm in the Level 2 calorimeter boards.

Level 2 provides a factor of 100 reduction over Level 1, passing on a 300 Hz rate into Level 3. Once an event passes the Level 2 triggers the data acquisition system is told to read out and fully reassemble the event and to check the event against the Level 3 triggers. Level 3 is a farm of approximately 300 CPU's, each fully analyzing a single event. Triggers applied at Level 3 reduce the data stream by a factor of 2. Once an event passes Level 3 it is delivered to the data-logger subsystem, which sends the event out to be stored, and to online monitors which verify the entire detector and trigger systems are working properly. A maximum rate of 75 Hz can pass Level 3 and be written out to tape.

2.2.6 Detector Control

The CDF detector is run by a shift crew operating on 8 hour shifts. They are 2 ACES, 1 CO, and 1 Sci-Co. The Sci-Co (scientific coordinator) is a senior member of the collaboration who is in charge of the shift and makes all final decisions regarding data quality for their shift. The CO (Consumer Operator) observes the online monitors for any problems which may arise during run-time. The two ACES are required

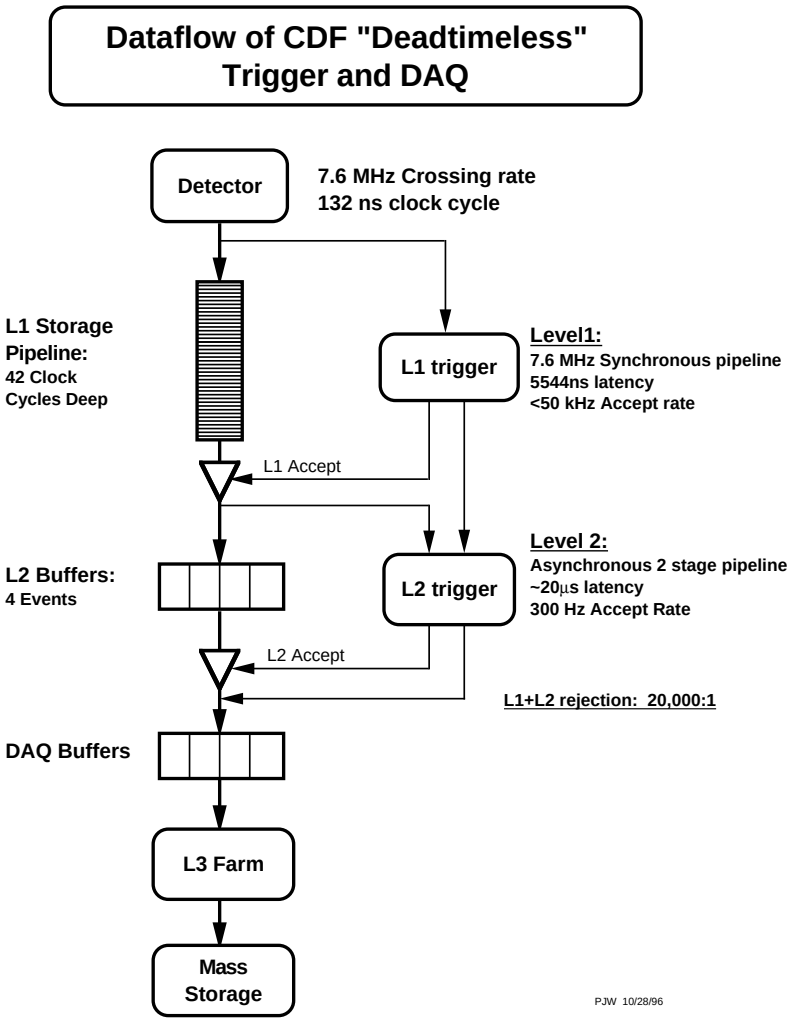

Figure 2.7: Trigger System Flowchart for CDF. This diagram shows the maximum rate which the trigger system was designed to handle. We are currently running at a 2.5 MHz input rate into Level 1, and a 20 kHz output rate from Level 1. [42]

to setup and start data taking runs, as well as debug any problems which can occur with the detector.

2.2.7 Offline Reconstruction

Data are re-processed offline before being used by the different physics groups. It is here that calibrations used online are checked and corrected, silicon alignment is corrected, tracks are re-fit, cluster energies are checked, leptons are found, and algorithms which "tag" secondary vertices in jets are run. (See Section 4.2 for a discussion on tagging) Data used in this analysis have been reprocessed using offline version 4.11.1. For consistency all Monte Carlo samples used for this analysis have also been created using the 4.11.1 code packages.

2.3 Data Samples

The data must go through a series of collection and refinement steps before we are able to apply the lepton+jets selection cuts. Data used is first identified online during data taking by requiring there be at least one high energy electron or muon in the event. See Section 3.2 for a discussion of these triggers. Offline the events which pass this requirement are more carefully manipulated during the production and reconstruction processes. It is during these processes that more precise calibrations are included for the detector components, and more detailed algorithms are applied to reconstruct tracks and calorimeter clusters in the data. Finally the data is stored into an easily manipulated format, the ntuple. Once data is in the ntuple format we then separate out the chunks which were obtained with all detector components collecting quality data. This occurs through the application of a "good-run" list. (See Section 2.3.1) We apply our lepton+jets event selection criterion only to those events passing both the online trigger and the good run requirements.

2.3.1 Good Run List

Once the bunches of protons and anti-protons are injected into the Tevatron they collide until the the instantaneous luminosity has fallen to the point at which it becomes difficult to collimate the two beams. This is a flexible end point, as determined by the Tevatron operations crew during running. This period of collisions is known as a store. Each store is broken up into several smaller chunks called runs. Runs begin with data taking online and are ended typically due to a detector subsystem pulling an error line, making data collection temporarily impossible. Several runs may be taken during one store. Once data for an analysis has passed the online trigger requirements the good-run list is applied as a check on data quality.

Runs are examined both online and offline to verify the quality of data recorded. The first step of examination occurs during run time via the ACES, who decide if the run is to be used for analysis purposes or for calibrations of the detector. At the end of each 8 hour shift the Sci-Co reviews all data runs and detector components that were active during the runs and decides if individual runs should be classified as "good". Each detector group then reviews these runs offline, running a standard set of checks to verify the quality of data in their portion of the detector. These runs are later reviewed by the "Good Run Czar(ina)", after hearing from representatives from all detector components. There are two good run lists currently in use at CDF - for analyses that do or do not require silicon tracking systems. This analysis relies heavily on the inclusion of silicon for tracking and identification of b-jets from top quark decays. Runs used have passed a set of requirements are included on the *good run list with silicon.*

2.3.2 Final Data Sample

Data used in this analysis spanned runs in the range 141544 - 163527 for the CEM and CMUP triggers, runs 150145 - 163527 for the CMX. This represents a total integrated luminosity of 107.9 $\pm$ 6.4 pb^{-1} for the CEM electrons and CMUP muons, and 98 $\pm$ 5.8 pb^{-1} for CMX muons. (See Section 6.5 for further details on the luminosity measurement and errors.)

2.4 Monte Carlo Samples

Throughout this analysis we rely on several collections of simulated data events. These samples are generated using a Monte Carlo simulation for both the $t\bar{t}$ signal and various background events. The events are first created using either ALPGEN [32], PYTHIA [33] or HERWIG (Hadron Emission Reactions With Interfering Gluons, [34]) event generators. These are general-purpose Monte Carlo event generators for high-energy processes. They offer a complete model of the physics of proton anti-proton collisions, with emphasis on detailed simulation of QCD parton showers. These generators include simulations of hard lepton-lepton, lepton-hadron, and hadron-hadron scattering, as well as soft hadron-hadron collisions. Output from these simulations is sent through a GEANT [35] detector simulation. GEANT describes the passage of particles through matter. It allows for a full simulation of the detector response to particles created during collisions. Once processed by GEANT, the simulated events can be manipulated in the same way as real data which has been collected by the detector. We use these Monte Carlo samples to understand the acceptance and efficiencies of event selection cuts on $t\bar{t}$ signal events. We also use simulated samples in part to calculate the expected backgrounds to this analysis. The various Monte Carlo samples used in this analysis are described in the appro-

priate sections. All Monte Carlo samples used in the calculation of backgrounds are shown in Table 7.21.

CHAPTER III

Event Selection

3.1 The Lepton+Jets Channel

Top events in the lepton+jets channel are identified by looking for the decay products of the two W bosons and the jets produced by the two b quarks which come from the top decay. In the lepton+jets channel one W decays into a lepton-neutrino pair and the other decays into a quark anti-quark pair, which produces two jets in our detector. The decay products from the leptonically decaying W are found by placing a lower limit on the event missing transverse energy ($\not\!\!E_T$) for the neutrino (See Section 3.6), and by requiring that there be one and only one *tight* electron or muon in the candidate event. Tight cuts are selection requirements applied to offline data which are stricter than those made online during data collection. [48] (See Table 3.1 for tight lepton and jet cuts.) In an ideal situation we expect exactly 4 jets in a lepton+jets $t\bar{t}$ event : two from the W decay and two from the b-jets. As shown in Figure 3.1, a small portion of $t\bar{t}$ events have some jets lost, resulting in only one or two tight jets being reconstructed in the event. The majority of $t\bar{t}$ events have at least three tight jets.

We examine events in the 1, 2, 3, and $\geq$4 tight jet bins. We require that of the tight jets in the event at least one must be identified as having come from the

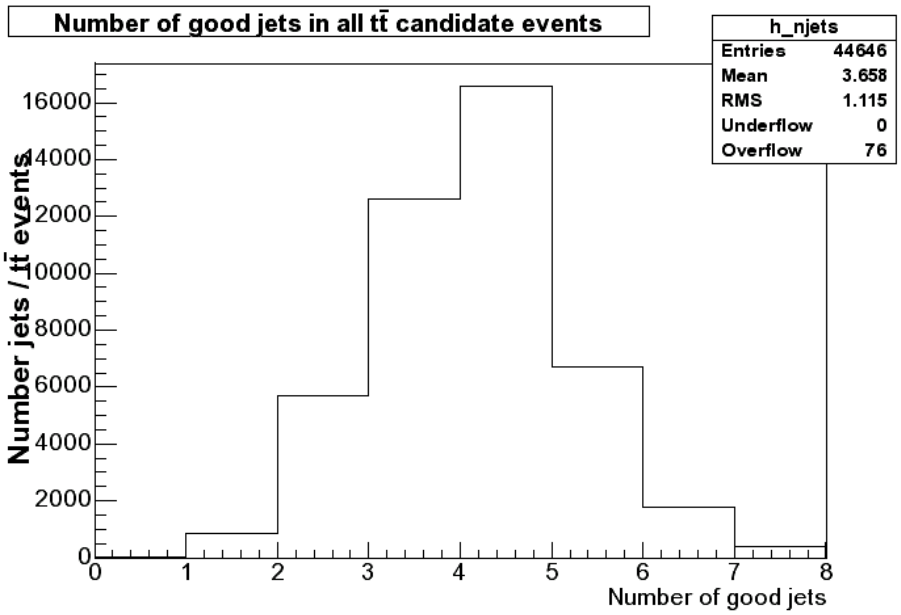

Figure 3.1: Number of Tight Jets in Lepton+Jets $t\bar{t}$ Monte Carlo Events

b-quark. This happens through the identification of a secondary vertex, i.e. a "B-tag". (See Chapter IV for a complete discussion on B-tagging) In the 1 and 2 jet bin region we expect the large number of background events will swamp the small top signal. In the ≥ 3 jet bins the background events form only a fraction of the observed events; the rest of the events are our top signal events. We only use events having at least three tight jets, of which at least one must be B-tagged, in this cross section measurement.

We apply three additional cuts to the events to reduce the number of background events contained in our set of candidate data events. These are the Z-veto, cosmic veto, and conversion removal cuts.

- Z Veto : The Z-veto cut rejects events in which the lepton and another object form an invariant mass in a window around that of the Z boson. This cut eliminates events which come from real Z decays, but which fake the lepton+jets signature when one of the leptons from the Z decay is lost. (See Section 3.7)

- Cosmic Veto : It is possible to reconstruct muons in our detector that did not come from the proton anti-proton interaction but instead came from cosmic rays. We apply a cosmic ray veto to all candidate events containing a tight muon. (See Section 3.4.2).
- Conversion Removal : Photons interacting with matter can produce electron-positron pairs, i.e. conversions. These can fake the lepton from the W decay. We apply a conversion removal algorithm to all candidate events containing a tight electron. (See Section 3.4.1)

The combination of cross section results from all three channels is simplified if there are no correlations between results. As a final cut we apply a dilepton veto to our candidate events. (See Section 3.8) This ensures that we do not have any events which overlap with the dilepton channel selection. Events which pass all of these lepton+jets selection cuts are referred to as the "W+jets" sample.

3.2 Online Triggers

Data used in this analysis must first pass the online requirement that there exists at least one high energy electron or high momentum muon in the event. This analysis uses one trigger path for central electrons, ELECTRON_CENTRAL_18. There are three parts to the muon detector : the CMU, CMP, and the CMX. The MUON_CMUP18 trigger path utilizes information from both the CMU and the CMP detector systems. Muons found in the CMX detector are also used in this analysis, via the MUON_CMX18 trigger path.

To use the energy of the particles for a trigger decision the calorimeter granularity is simplified into a 24 x 24 grid in η and ϕ. These divisions are called "trigger towers". Each trigger tower spans 15 degrees in ϕ and approximately 0.2 in eta, which covers

one or two physical towers. The readout electronics calculate the transverse energy, E_T, deposited in each trigger tower. Energies are reported in increments of 0.125 GeV, allowing a full scale range of 127.875 GeV per trigger tower. [27] [28]

The ELECTRON_CENTRAL_18 trigger path comprises three separate triggers : L1_CEM8_PT8, L2_CEM16_PT8, and L3_ELECTRON_CENTRAL_18.

- L1_CEM8_PT8
  - $\geq$ one deposition of energy in the Central calorimeter with $E_T > 8$ GeV, Hadronic to Electromagnetic energy ratio (HAD/EM) < 0.125
  - $\geq$ one COT track found having $P_T > 8.34$ GeV/c
- L2_CEM16_PT8
  - $\geq$ one deposit of energy in the Central calorimeter with $E_T > 16$ GeV, HAD/EM < 0.125
  - $\mid \eta \mid < 1.317$ is placed on the cluster centroid (seed), guaranteeing the cluster be located in the central portion of the calorimeter
  - Requires a match between tracks found in the COT at Level 1 to the cluster within a window of ϕ, as determined by multiple scattering interactions in the detector
  - Track $P_T > 8.34$ GeV/c
- L3_ELECTRON_CENTRAL_18
  - Uses primary interaction location as found by the track matched to the cluster to recalculate the cluster E_T
  - Cluster $E_T > 18$ GeV
  - Track $P_T > 9.00$ GeV/c

  - Level 3 also adds a cut on the lateral shower profile (Lshr) of the cluster. This quantity describes how well the energy deposit in the calorimeter matches one coming from an ideal electron.

The MUON_CMUP18 trigger path contains the L1_CMUP6_PT4, L2_TRK8_L1_CMUP6_PT4, and L3_MUON_CMUP_18 triggers.

- L1_CMUP6_PT4
  - Muon stub in the CMU detector having $P_T > 6$ GeV/c
  - Track in the COT with $P_T > 4.09$ GeV/c
  - Require an additional stub in the CMP detector
  - Matching is done at Level 1 between the stubs and the COT track, within a window of a few degrees
- L2_TRK8_L1_CMUP6_PT4
  - ≥ 1 COT track ranging between ϕ of 0 to 180 degrees
  - COT track $P_T > 8$ GeV/c
- L3_MUON_CMUP_18
  - Match between tracks and the CMU and CMUP stubs, allowing a window in r-$\Delta\phi$ of less than 20 cm for the CMU stub, 10 cm for the CMP stub

Our final trigger path is the MUON_CMX18 path, which has L1_CMX6_PT8_CSX, L2_AUTO_L1_CMX6_PT8_CSX, and L3_MUON_CMX18 triggers.

- L1_CMX6_PT8_CSX
  - Muon stub in the CMX detector having $P_T > 6$ GeV/C
  - Require hits in the CSX detector

  - Require a track in the COT passing through at least 4 layers of the COT detector
  - COT Track $P_T > 8.34$ GeV/c

- L2_AUTO_L1_CMX6_PT8_CSX
  - The Level 2 trigger requirement is an auto accept trigger, meaning that no additional manipulating of data occurs at this level

- L3_MUON_CMX18
  - Tracks matched to the CMX stub in a window of r-$\Delta\phi$ of less than 10 cm
  - COT track $P_T > 18$ GeV.

3.3 Primary Vertex

Many of the selections and calculations used in this analysis rely on knowing the position of the interaction point of the proton anti-proton collisions. This point is called the primary vertex. The calculations for the transverse energy of the calorimeter deposits (Section 3.5.1), and the $\not\!\!E_T$ in the event (Section 3.6) rely critically on knowing the z coordinate of the primary vertex.

The primary vertex z position is found early in the analysis. Stand-alone tracking is run in the silicon and COT detectors, in the r-z plane. Tracks passing minimal quality requirements are then used to triangulate vertex candidates in the event. These vertices will have a high efficiency but also a high fake rate. The primary vertex finder, ZVertexColl, "cleans-up" these pre-tracking vertices by requiring a certain number of tracks, which differs across analyses, with a minimum P_T of 300 MeV/c be associated with these vertices. The primary vertex finder can require the vertices contain either tracks which have silicon hits or COT hits associated with

the vertex. This analysis only considers vertices which have at least 2 tracks that contain COT hits. [54]

We assign a z0, or point of origin along the z axis, to all tracks in the event. (Section 2.2.2) A track is associated with a vertex if it is within 1 cm of a silicon standalone vertex, or 5 cm of a COT standalone vertex. The position of the vertex is then determined by weighting the z0 of all tracks in the vertex by their error :

$$z = \frac{\sum_i z_i^0/\delta_i^2}{\sum_i 1/\delta_i^2} \tag{3.1}$$

here the sum is over all tracks associated with the vertex, and δ_i is the error on the z0 of the ith track.

The x and y coordinates of the primary vertex, vital for the B-tagging algorithms, are found through the use of the PrimeVtx algorithm. [44] PrimeVtx calculates the primary vertex on an event-by-event basis, starting from an input vertex (seed), which has an initial $x_0, y_0,$ and z_0 position. The seed vertex is the beamline position, measured during collisions. All tracks which pass a cut in $\triangle z$ and d_0 from the seed vertex are ordered in decreasing P_T. These requirements are :

- $\mid z - z_{vertex} \mid < 1.0$ cm
- $\mid d_0 \mid < 1.0$ cm (with respect to the beamline)
- $\frac{|d_0|}{\sigma} < 3.0$ (with respect to the beamline)

The highest P_T tracks (maximum of 50 tracks) are used in a fit to a common vertex. PrimeVtx first removes the track with the worst χ^2 relative to the vertex, above a cut of > 10. The remaining tracks are fit again to a common point. This iterative process occurs until there are no tracks have a $\chi^2 > 10$ relative to the vertex.

Precision reached on the x and y coordinates of the vertex is a strong function of the z position of the primary vertex, and ranges from approximately 25μm to 30μm. [45]

3.4 Tight Lepton Selection

The lepton+jets cross section analysis uses events containing electrons or muons. General descriptions of the selection cuts applied to electrons can be found in Section 3.4.1, for muons in Section 3.4.2. Table 3.1 lists all lepton selection quantities along with the minimum or maximum value accepted for that quantity. [48].

3.4.1 Electron Selection

Electrons lose their energy in the form of radiation as they travel through material. The calorimeter is designed to have maximal energy deposition from electrons occur in the electromagnetic portion of the detector. Electrons are found by matching deposits of energy in the EM calorimeter to a track in the COT detector. A requirement is made during data collection via the triggers that the ratio of hadronic to electromagnetic energy of candidate calorimeter clusters be less than 0.125. This cut reduces the amount of jets which are misidentified as electrons. In addition, there are minimum E_T and P_T requirements on the cluster energy and track transverse momentum applied online.

Offline we apply a more rigorous set of cuts to the electron object. We require the minimum E_T of the calorimeter deposit to be at least 20 GeV. The shapes of the electron E_T and muon P_T from W decays in $t\bar{t}$ events are similar. (See Figure 3.3) The COT track P_T must be greater than 10 GeV. The requirement on HAD/EM is tightened to be less than $\sim$0.055. Additional cuts are placed on the ratio of total energy to total momentum, and the "fiduciality" of the electron. Fiduciality of an electron implies that the cluster centroid falls within the bounds of good coverage

by the CES, and in a region where the energy response from the CEM phototubes is well understood. In the central calorimeter the determination of fiduciality is made in the local wedge coordinate system. The cuts are :

- $\mid Local\ x \mid \leq 21.0$ cm
- 9.0 cm $\leq$ Local z $\leq$ 230.0 cm

The track matched to the calorimeter cluster is also re-examined. A cut on the absolute value of z0 of the track ($\leq$ 60 cm) guarantees that we use a COT track that has its origins within the most optimal portion of the tracking chambers. The track has a set of minimum requirements for the number of good segments in both the axial and stereo dimensions of the COT, and on the number of hits per segment. When matching the track to the electron cluster we extrapolate the COT track into the CES portion of the calorimeter and see if there are any hits in the CES that fall within this extrapolation window. A cut of Δz $\leq$ 3 cm ensures that we are using a CES track that falls within the extrapolation window in z. A cut on the charge times the Δx of the track confirms that we are using a CES track that falls within the extrapolation window in x. The strip chi squared (χ^2) is a cut on the quality of the shape of the cluster in the CES, when comparing to that coming from an ideal electron.

In addition we require that the electron calorimeter cluster is isolated. An electron is a point-like particle, and its passage through the calorimeter should leave a collimated energy deposit. In the decay $W \rightarrow e\nu$, there should be little hadronic energy surrounding the electron. Jets, on the other hand, tend to spread out, leaving a large calorimeter deposit. We can reject jets that fake electrons by looking at electron "isolation". The isolation is calculated by measuring all E_T, both electromagnetic and hadronic, in a cone of $\triangle$R $\leq$0.4 around the electron. See Equation 3.4

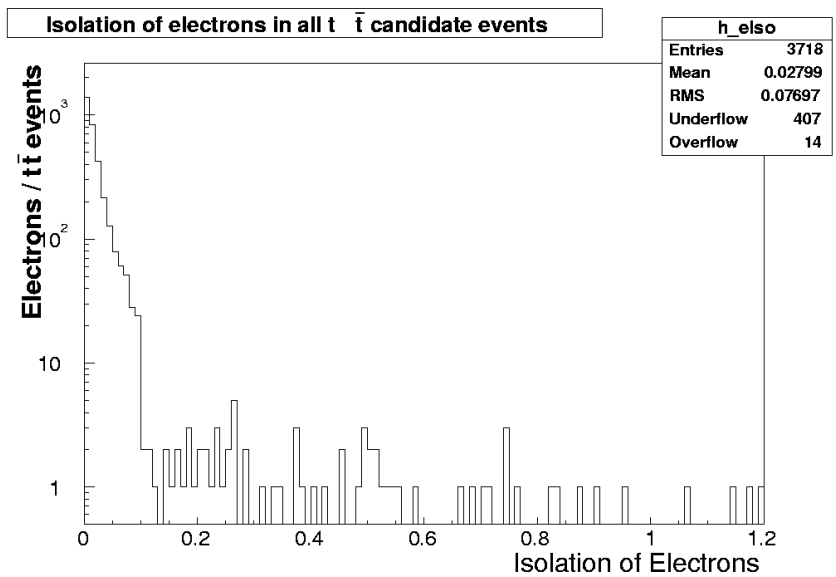

Figure 3.2: Isolation of Tight Electrons in Lepton+Jets $t\bar{t}$ Monte Carlo Events

for the definition of $\triangle$R. We subtract from this total E_T the E_T of the electron. This quantity is then divided by the E_T of the electron to give the isolation :

$$\text{isolation} = \frac{E_T \; in \; \triangle R \leq 0.4 - E_T \; electron}{E_T \; electron} \tag{3.2}$$

Figure 3.2 shows the isolation of electrons in candidate events which have passed all selection cuts, before applying the isolation requirement of < 0.1.

The final cut applied to electron-like objects is a conversion removal. The conversion finder looks for electrons that may have come from photon conversions in the material of the detector prior to the calorimeter. An electron coming from conversions would have separation in parallel tracks between itself and its conversion partner in the x-y plane of less than 0.2, and separation in the z direction of less than 0.004. Any electron falling within these bounds is labeled a conversion and rejected from consideration as our tight lepton in the event.

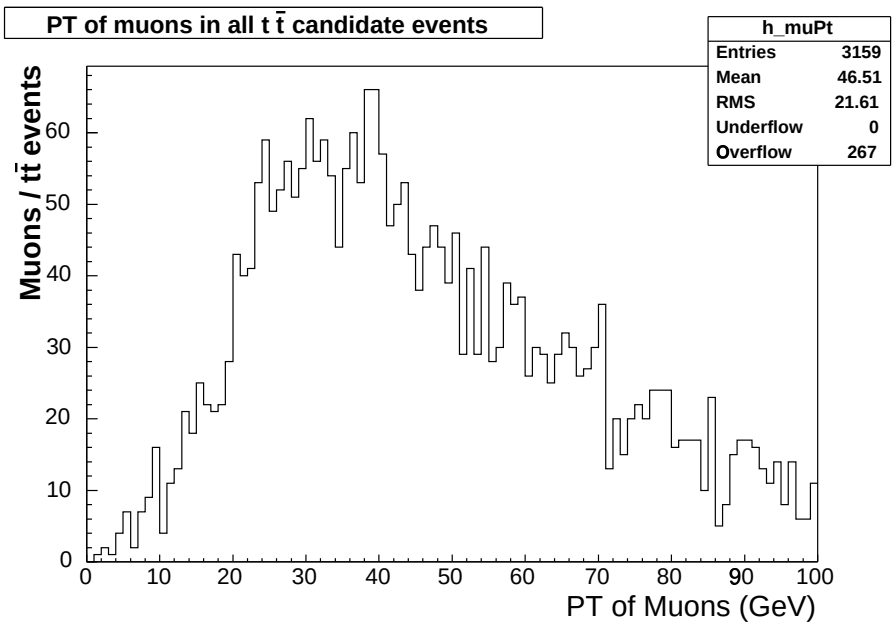

Figure 3.3: P_T of Tight Muons in Lepton+Jets $t\bar{t}$ Monte Carlo Events

It should be noted that while this analysis currently only considers tight electrons found in the central region of the calorimeter as one of the choices for the lepton requirement, plans are underway to include those found in the plug calorimeter. To that end we have already begun removing tight jets that can be matched to plug electrons in the event (Section 3.5.2), and are including plug electrons in our dilepton veto (Section 3.8).

3.4.2 Muon Selection

In the muon selection we start with a strict condition on the P_T of the track matched to the muon. Figure 3.3 shows muon P_T in candidate events after all other selection cuts have been applied. A natural division occurs around 20 to 25 GeV.

A muon is identified when a stub found in the muon detectors is matched to a track. There are several quality requirements placed on the track matched to the muon stub. There are a minimum number of good segments required in both the stereo and axial layers of the COT, as well as a minimum number of hits per segment.

A cut on the absolute value of z0 of the track guarantees that we use a COT track that has its origins within the most optimal portion of the tracking chambers. In addition, to help reject cosmic rays, we examine the impact parameter, d_0, of the track matched to the muon object. The precision of the impact parameter measurement depends on whether the tracks contains hits in the silicon detectors. We have two sets of cuts on the d_0, one cut for tracks which do have silicon hits, and one for tracks which do not. Tracks not having silicon hits must have a d_0 cut of ≤ 0.2 cm, while those with silicon hits must have $d_0 \leq 0.02$ cm.

We also place quality cuts on the match between the muon stub and the track. There is a maximum distance allowed in $r - \phi$ space (Δx) between the muon stub and the track extrapolation to the stub. For CMU muons this is ≤ 3.0 cm, for the CMP stubs it is ≤ 5.0 cm, and for the CMX detector we place a limit of ≤ 6.0 cm. Figure 3.4 shows the $\mid \Delta x \mid$ of muons in candidate events which have passed all cuts, before applying the $\mid \Delta x \mid$ cut. The left hand side of this figure is for CMU muons, the middle plots shows the $\mid \Delta x \mid$ value for CMP stubs, and the right hand plot is for CMX muon stubs. It is quite clear from these plots that the natural point to place the cut is at 3, 5, and 6 cm, respectively.

Muons are minimum ionizing particles. They deposit only a small amount of energy in the calorimeter. Using position information from the tracking detector and muon chambers we extrapolate the path of the muon through the calorimeter. Offline we apply requirements on the upper limits of the amount of electromagnetic and hadronic energy in the calorimeter towers associated with a given muon object.

As with electrons we apply an isolation cut to the muon objects. The isolation is calculated in a slightly different fashion from the electron isolation variable. The muon isolation is found by measuring all E_T, both electromagnetic and hadronic, in

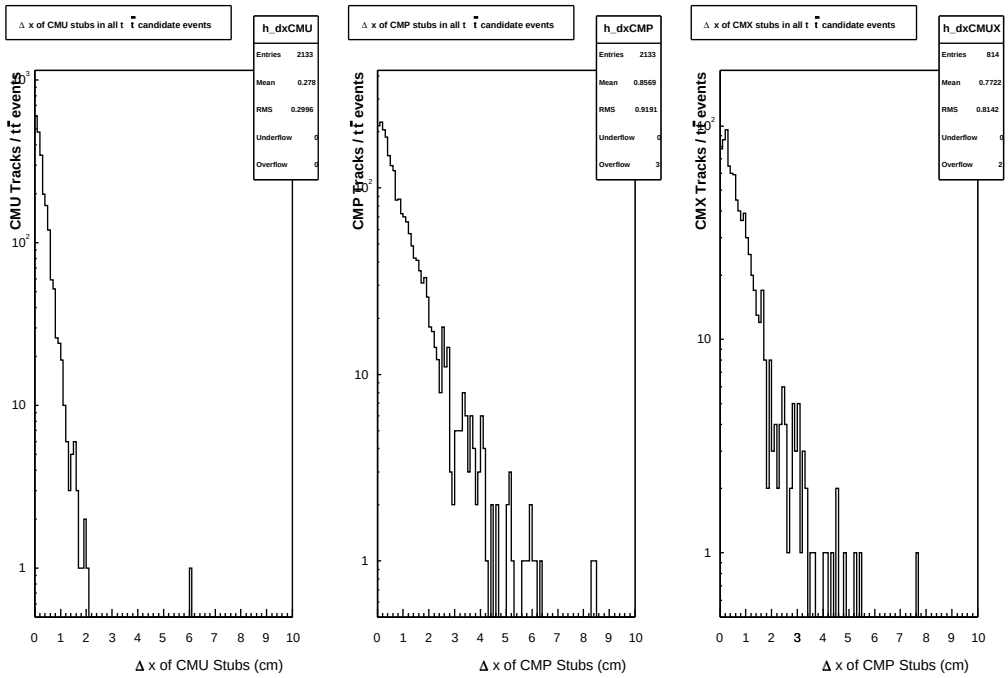

Figure 3.4: Δx between Muon Stubs and Tracks in Lepton+Jets $t\bar{t}$ Monte Carlo Events

a cone of $\triangle$R $\leq$0.4 around the track matched to the muon. See Equation 3.4 for the definition of $\triangle$R. This total E_T is then divided by the P_T of the muon track to give the isolation :

$$\text{isolation} = \frac{E_T \ in \ \triangle R \leq 0.4}{P_T \ muon} \tag{3.3}$$

Figure 3.5 shows the isolation of muons in candidate events which have passed all other selection cuts, before applying the isolation cut.

Finally, all events containing a tight muon are checked for signatures matching those coming from cosmic rays. [49] Cosmic ray muons ideally pass through the detector leaving two signatures in the muon chambers, separated spatially (by 180 degrees), and separated in time as they pass from one end of the detector to the other. Each of these signatures is referred to as a *leg*. The tracking systems record

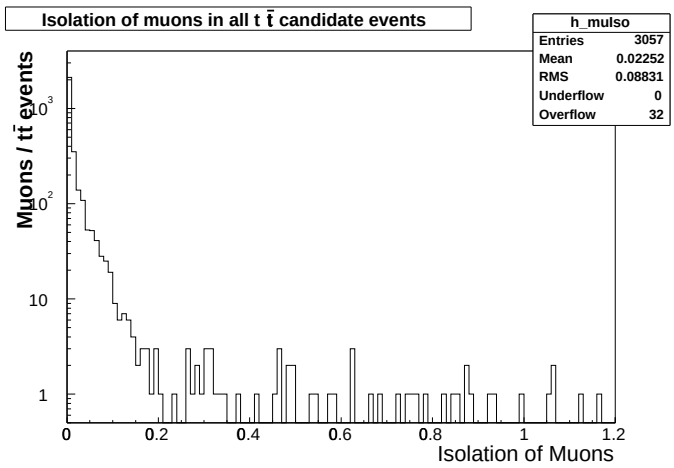

Figure 3.5: Isolation of Tight Muons in Lepton+Jets $t\bar{t}$ Monte Carlo Events

information on when tracks arrive in the detector. For particles coming from the collision point we expect the leg(legs) to occur in the same window in time. For particles which come from a cosmic ray event there will be a separation in time as the cosmic ray travels from one side of the detector to the other. In addition, the hadronic calorimeters are capable of recording when in time energy was deposited. A separation in time will also be observed for cosmic rays in the calorimeter, but not for particles coming from the proton anti-proton collisions.

There will be situations in which we are able to identify only one of the two legs in a cosmic ray event. The cosmic veto looks at one and two leg cases. The one leg check requires a cut on the $\Delta\phi$ between any reconstructed muon and any other muon stub found in the detector, and on the timing information acquired from the calorimeter and tracking systems. The two leg algorithm places a limit on the $\Delta\phi$ between either any two reconstructed muons in the event, or any reconstructed muon and muon stub matched to a track. The two leg algorithm also requires a cut on the timing information from calorimeter and tracking detectors. [50] Events which fail any of these scenarios are assumed to have come from cosmic rays and are rejected

from our candidate event selection.

3.5 Jet Selection

Quarks and gluons hadronize into sprays of charged and neutral particles which leave several neighboring energy deposits in the calorimeter. These showers of energy are called *jets*. Jets are identified by combining energy deposits in the individual calorimeter towers into a larger grouping known as a cluster. The jets used in this analysis are reconstructed offline using the JetClu clustering algorithm.

Energies recorded in the calorimeter towers are organized from largest to smallest. Seed towers are all towers which have an energy greater than 3 GeV. JetClu begins clustering around the highest E_T seed in an event. The seed is assumed to be the geometric center of the jet. Towers that lie within a cone of $\Delta R < 0.4$ from this center are included into the cluster. ΔR is defined as :

$$\Delta R = \sqrt{(\phi_{tower} - \phi_{centroid})^2 + (\eta_{tower} - \eta_{centroid})^2} \tag{3.4}$$

Once all deposits have been included an energy-weighted centroid is calculated. This new centroid is then used as the geometric center of the cone and the clustering begins again. This process continues until the energy weighted centroid of the cluster is aligned with the geometric axis of the previous cone. Once a tower has been used in a cluster, or jet, it is disallowed from participating in any other jet in the event. [51]

In the lepton+jets analysis we apply cuts to the E_T and the η of the jet objects in an event. We require that the jet be located in the central or plug portion of the detector ($\mid \eta \mid < 2$). The E_T requirement is not entirely straightforward. Various processes can skew the energy reported by the calorimeter during data taking. Energy measurements for the jets need to be corrected for these mismeasurements. (See

Section 3.5.1) In this analysis we first correct the energy of the jets, and then apply an E_T cut of > 15 GeV to the corrected jet energy.

3.5.1 Jet Energy Corrections

Jet energies measured by the calorimeter must be corrected for various detector effects before the jets may be used in analysis. [52] [53] These corrections are found via a program of study which examines the transverse energy balance in di-jet and γ+jet events. The γ+jet events are particularly useful because of the good calorimeter resolution on the photon.

A description of the jet energy corrections is listed below :

- Relative Energy : makes the calorimeter response uniform in η
- Time Dependence : corrects for the variation in phototube response due to aging effects
- Multiple Interactions : the current running conditions of the Tevatron (luminosity, 36x36 collisions) creates an environment in which we expect, on average, one interaction per crossing, or collision. The number of interactions has a Poisson distribution, and it is possible to have more than one interaction per collision. This correction takes into account these multiple interactions
- Absolute Energy Scale : jet energy measured by the calorimeter must be corrected for non-linearity and energy loss which occurs in areas of the calorimeter which are not fully instrumented, or covered by the phototubes. This correction converts the calorimeter cluster P_T to the $\sum P_T$ of particles in the jet cone
- Underlying Event : hadron collisions actually occur on the parton level - one parton from a proton interacts with a parton from the anti-proton. The additional partons in the event interact peripherally and project a low energy

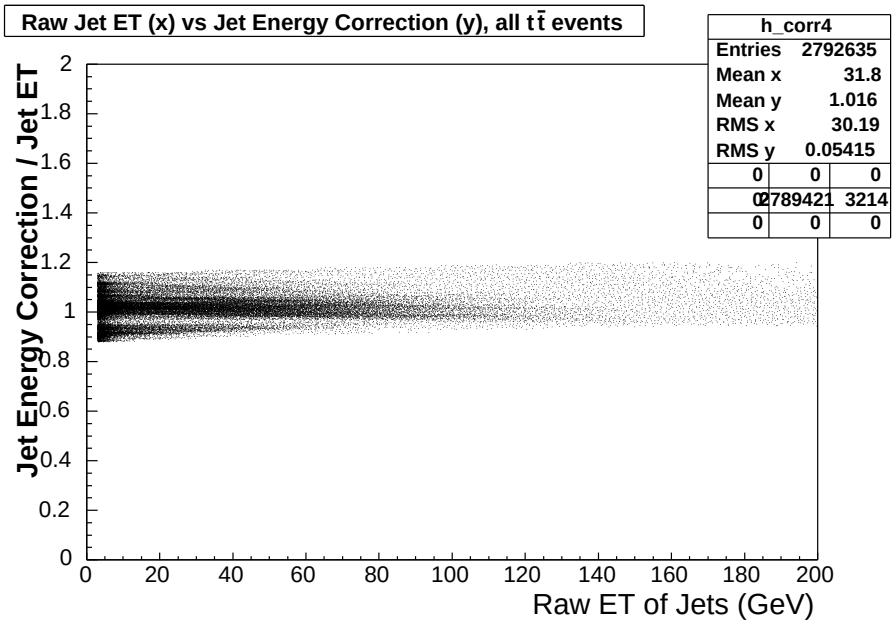

Figure 3.6: Jet corrections applied using level 4 corrections, as a function of uncorrected jet E_T.

background onto the event. Energy from these interactions may be included in the cone of our jets. We subtract this underlying event energy to obtain the particle level jet P_T

- Out-of-Cone : jet clustering may not include energy from the initial parton. This correction allows one to correct the particle level jet energy to the parton level

The lepton+jets cross section analysis currently applies corrections to the jet energy for relative energy, time dependence, and multiple interactions. This set of corrections is known internally as "level 4" corrections. Corrected jet E_T is found by multiplying the uncorrected E_T by a single multiplicative correction. The maximum correction applied at level 4 is ~20%. The correction applied as a function of uncorrected jet E_T is shown in Figure 3.6.

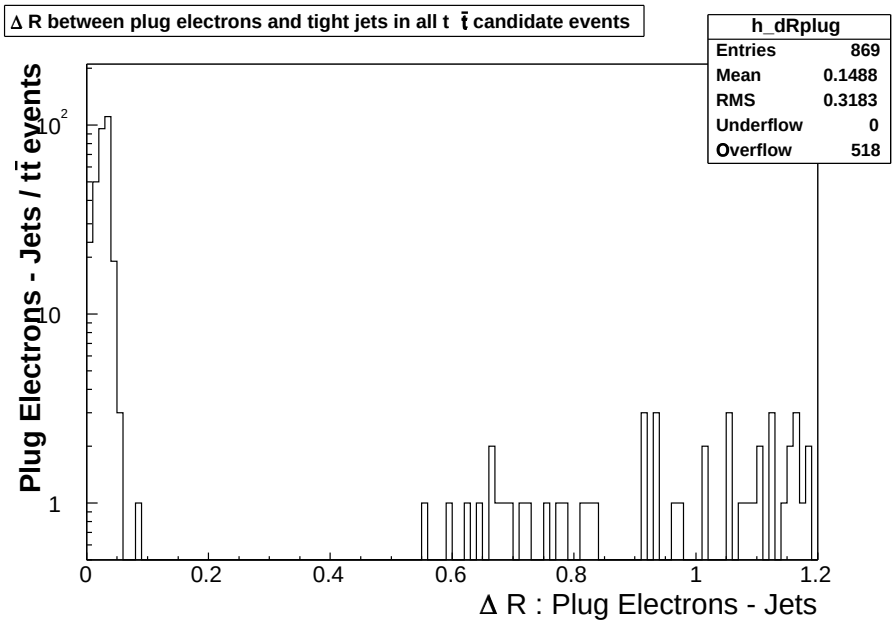

Figure 3.7: ΔR between Plug Electrons and Tight Jets in Lepton+Jets $t\bar{t}$ Monte Carlo Events

3.5.2 Plug Electron Removal

After finding our collection of good corrected jets offline for each event we then look for any plug electrons that may have been misidentified as jets. We match plug electrons to our collection of good jets in a cone of ΔR < 0.4 :

$$\Delta R = \sqrt{(\phi_{ele} - \phi_{jet})^2 + (\eta_{ele} - \eta_{jet})^2} \tag{3.5}$$

Any jets matched to a plug electron are then no longer considered in the tight jet collection for that event. Figure 3.7 shows the absolute value of ΔR between plug electrons and tight jets in candidate $t\bar{t}$ Monte Carlo events.

3.6 $\not{E}_T$ Measurement

In a proton anti-proton collision the total transverse momentum (energy) of the event should sum to zero. For each of our candidate events we create a vector sum of the transverse energy of all objects (calorimeter and muon) in the event. Any

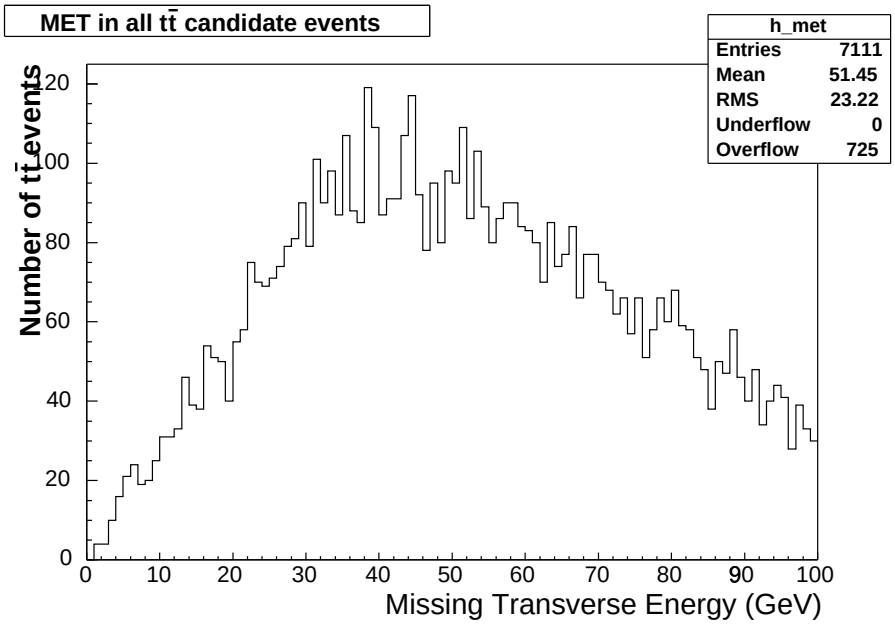

Figure 3.8: $\not\!\!E_T$ in Lepton+Jets $t\bar{t}$ Monte Carlo Events

additional amount left over is the "missing transverse energy", or the transverse energy imbalance in an event. $\not\!\!E_T$ can come from many sources such as neutrinos, loss of particles to cracks, and energy mismeasurement in an event. As part of the selection criterion for the lepton+jets channel we must identify a lepton and neutrino which came from a W boson decay. The identification of the neutrino occurs through the measurement of missing transverse energy in the event. Figure 3.8 shows the event $\not\!\!E_T$ for $t\bar{t}$ lepton+jets events.

$\not\!\!E_T$ is calculated by creating a vector sum of all calorimeter deposits and muon objects in the event. The $\not\!\!E_T$ calculation sums *transverse* energies, i.e. $E_T = \mathrm{E} \cdot \sin \theta$. If the primary point of interaction is not located in the center of the detector then the θ angle will be distorted, causing an incorrect E_T to be found. We assume the highest E_T tight lepton came from the true point of primary interaction. The $\not\!\!E_T$ is recalculated using the event z vertex, as determined by the z0 of the maximum E_T tight lepton. The $\not\!\!E_T$ is then corrected for any tight muons in the event; the muon p_x

and p_y components are subtracted and, to avoid double counting, the energy deposits left by the muon in calorimeter towers are added on a tower by tower basis.

In the final analysis, the data is processed more carefully. (Section 2.2.7) In addition to using more detailed algorithms to perform tracking and clustering, we also allow for a more thorough calculation of the primary vertex, The $\not{E}_T$ calculation must account for these corrections. For each event we first calculate the x and y components of the $\not{E}_T$ vector which was found during production :

$$\begin{aligned} \not{E}_{Tx} &= \not{E}_{Tonline} \cdot cos(\phi_{\not{E}_{Tonline}}) \\ \not{E}_{Ty} &= \not{E}_{Tonline} \cdot sin(\phi_{\not{E}_{Tonline}}) \end{aligned} \tag{3.6}$$

Reprocessing of tracks offline results in a curvature correction to the P_T of the muons. The x and y components of the $\not{E}_T$ are corrected for this effect :

$$\begin{aligned} \not{E}_{Tx} &= \not{E}_{Tx} + (P_{T_{uncorrected}} - P_{T_{corrected}}) \cdot cos(\phi_{uncorrected}) \\ \not{E}_{Ty} &= \not{E}_{Ty} + (P_{T_{uncorrected}} - P_{T_{corrected}}) \cdot sin(\phi_{uncorrected}) \end{aligned} \tag{3.7}$$

The $\not{E}_T$ is calculated using raw jet energies. As mentioned in Section 3.5.1 we need to correct the jet energy before applying the E_T cut to jets used in our analysis. The x and y components of the $\not{E}_T$ are corrected for the difference between the raw and corrected jet energies. This is done for all jets with a corrected $E_T \geq 8.0$ GeV, which fall within an $\mid \eta \mid$ range of ≤ 2.5.

$$\begin{aligned} \not{E}_{Tx} &= \not{E}_{Tx} + (E_{T_{raw}} - E_{T_{corrected}}) \cdot cos(\phi_{raw}) \\ \not{E}_{Ty} &= \not{E}_{Ty} + (E_{T_{raw}} - E_{T_{corrected}}) \cdot sin(\phi_{raw}) \end{aligned} \tag{3.8}$$

The final magnitude of the corrected $\not{E}_T$ vector is found by taking the square root of the sum of squares of the x and y components :

$$\not{E}_T = \sqrt{(\not{E}_{Tx} \cdot \not{E}_{Tx}) + (\not{E}_{Ty} \cdot \not{E}_{Ty})} \tag{3.9}$$

A plot of the reconstructed transverse mass of the W boson, found using the corrected $\not{E}_T$ and electron E_T, is shown in Figure 3.9. Here the W M_T is reconstructed in candidate electron $t\bar{t}$ events, using the electron E_T, electron ϕ, the $\not{E}_T$, and the $\not{E}_T$ ϕ :

$$\begin{aligned} \triangle\phi &= \mid \phi_{ele} - \phi_{\not{E}_T} \mid \\ WM_T &= \sqrt{2 \cdot E_{T_{ele}} \cdot \not{E}_T \cdot (1 - cos(\triangle\phi))} \end{aligned} \tag{3.10}$$

The peak of this plot occurs at 77.87 GeV. The world average mass of the W boson is 80.42 GeV. [64] The peak shown here is smeared due to the degradation of the $\not{E}_T$ resolution in $t\bar{t}$ events due to the presence of jets. However, in Figure 3.9 you can clearly see the edge of the Jacobian peak at 80 GeV.

3.7 Z Removal

The Z veto helps to reduce backgrounds coming from Z events. Z events can mimic W events when one of the legs, or leptons from the Z decay, are in some way misidentified. For example, in a Z→ee event one of the electrons could fall into a calorimeter crack, or be included in the jet collection. The Z veto removes events in which the tight lepton and any second object form an invariant mass between 76 and 106 GeV, a window of ± 15 GeV around the Z mass. The second object must be electron-like for events having an electron as the tight lepton; it must be muon-like for events having a muon as a tight lepton. For electrons this second object can be either an opposite sign electron, a reclustered jet with a small number of tracks, or

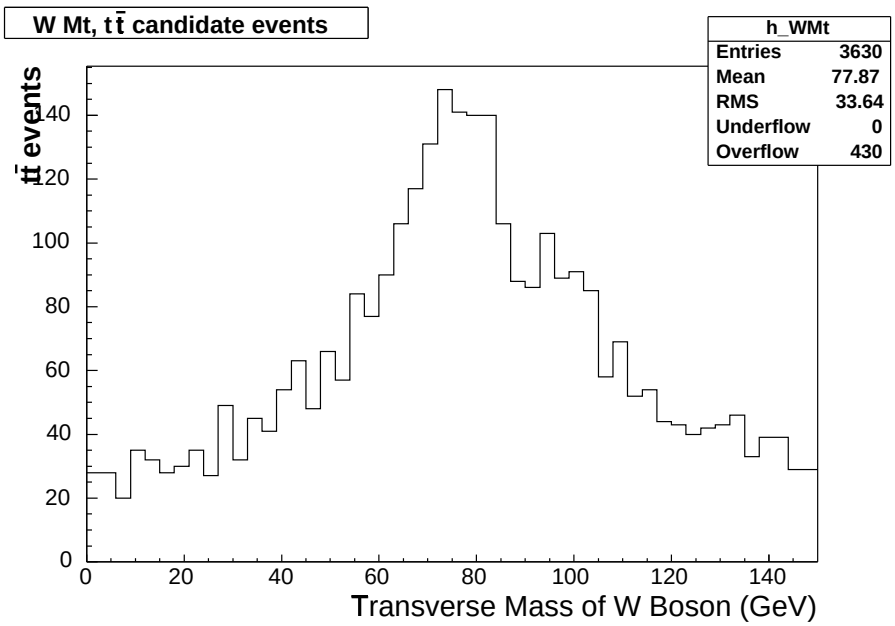

Figure 3.9: Transverse mass of W boson in candidate electron $t\bar{t}$ events, found using information from the electron and the $\not{E}_T$. The world average mass of the W boson is 80.42 GeV. [64]

an opposite signed track. For muons the second object can be an oppositely signed muon, an opposite signed stubless muon, or an opposite signed track.

3.8 Dilepton Veto

In order to avoid overlap between events used in the dilepton and lepton+jets analyses we apply a dilepton veto to our events. This veto requires that the sum of good tight leptons and plug electrons not matched to jets in each candidate event be equal to 1. Unfortunately, this veto is not entirely foolproof. The results presented in this document were found by using an event sample which has a one event overlap with events used in the dilepton cross section analysis.

Variable	Value
Global event quantities	
Z and cosmic veto	applied
Missing E_T	$\geq$ 20 GeV
# tight leptons	1
Jets	
E_T	$\geq$ 15 GeV
$\|\eta\|$	$<$ 2
Tight electrons	
Fiducial and CEM	= 1
E_T	$\geq$ 20 GeV
P_T	$\geq$ 10 GeV/c
E/P (if $P_T \leq$ 50 GeV/c)	$\leq$ 2.0
E_{had}/E_{EM}	$\leq$ 0.055 + 0.00045*E
L_{shr}	$\leq$ 0.2
$\|\Delta z\|$	$\leq$ 3 cm
$Q \times \Delta x$	$\geq$ -1.5 and $\leq$ 3.0 cm
χ^2_{Strip}	$\leq$ 10
$\|\Delta z_0\|$	$\leq$ 60 cm
# axial segments	$\geq$ 3
# stereo segments	$\geq$ 3
Isolation	$\leq$ 0.1
Not a conversion	$\Delta\Lambda > 0.03$ and $\Delta r > 0.3$
Tight muons	
Region	CMUP or CMX
P_T	$\geq$ 20 GeV/c
E_{EM}	$\leq$ max(2, 2 + 0.0115*(p-100))
E_{HAD}	$\leq$ max(6, 6 + 0.0280*(p-100))
$\|\Delta x\|_{CMU}$	$\leq$ 3.0 cm
$\|\Delta x\|_{CMP}$	$\leq$ 5.0 cm
$\|\Delta x\|_{CMX}$	$\leq$ 6.0 cm
$\|\Delta z_0\|$	$\leq$ 60 cm
$\|d_0\|$ if no Si hits	$\leq$ 0.2 cm
$\|d_0\|$ if Si hits	$\leq$ 0.02 cm
# axial segments	$\geq$ 3
# stereo segments	$\geq$ 3
Isolation	$\leq$ 0.1

Table 3.1: I.D and kinematic cuts for "tight" electrons, muons, and jets in the $t\bar{t}$ cross section analysis

CHAPTER IV

B-Tagging

4.1 Introduction

In the lepton+jets channel we have a final state signature of a lepton, a neutrino, two jets from a W decay, and two additional jets from the bottom quarks. There are many processes which mimic this lepton-neutrino-multijet signature. We can reduce these backgrounds by identifying the bottom jets in our candidate events using a technique called "B-tagging".

Bottom quarks hadronize, and then travel an observable distance before decaying. The average track multiplicity of a B hadron decay is approximately 5. Due to the long B hadron lifetime, these tracks will have a measurable impact parameter. The process of finding jets which have tracks displaced from the primary interaction point, which can be traced back to a secondary vertex, is called *B-tagging*.

4.2 The B-Tagging Algorithm

The distance a particle travels in the detector frame before decaying is the velocity of the particle ($\beta \cdot c$), multiplied by the time dilated lifetime of the particle, $\tau \cdot \gamma$:

$$distance = \gamma \cdot \tau \cdot \beta \cdot c \tag{4.1}$$

where, for b-jets coming from top decay at the Tevatron, the average P_T of the jets is around 65 GeV, β is $\sim$1, and γ is $\sim$ 15. The lifetime of a B hadron is, on average, 1.5 picoseconds, or $1.5 \cdot 10^{-12}$ seconds. Therefore, the average distance traveled before decaying is approximately 7.5 millimeters.

As seen in Figure 4.1, tracks in a secondary vertex will have a large impact parameter (d0), or perpendicular point of closest approach, with respect to the primary vertex. The average value of d0 is approximately $c \cdot \tau$, or the speed of light times the lifetime of the particle which has decayed. For B hadrons this value is $3 \cdot 10^8 \frac{meters}{seconds}$ times $1.5 \cdot 10^{-12}$ seconds, or 450 μm. The B-tagging algorithm, SECVTX, looks for tracks in the cone of each jet that have been so displaced from the primary vertex. Tracks must have a minimum number of silicon hits, and $\mid d_0 \mid \leq 0.3$ to be considered "good". If there are at least two good tracks in the jet the jet is then labeled "taggable", because a minimum of two tracks are required to form an intersection, or displaced vertex. A displaced vertex is required for a jet to potentially be tagged. A cut is then placed on the significance (≥ 2) of the d0 of each track. The significance ($s_{d0} = \mathrm{d0}/\sigma_{d0}$) is the ratio of the value of d0 and the error in its measurement. A vertex is then attempted to be reconstructed, using all of the "good" displaced tracks in the jet. Secondary vertices may be found using tracking information from the silicon detector. The impact parameter resolution achieved with the SVX detector is $\sim$28 μm. [10]

If there are at least two of these displaced tracks in the jet the tagging algorithm attempts to fit these tracks to a common vertex. The algorithm calculates the χ^2 value each track contributes to the fit. If the value is greater than 50 the track is no longer considered in the fit.

As a final step the tagging algorithm examines the distance between the primary

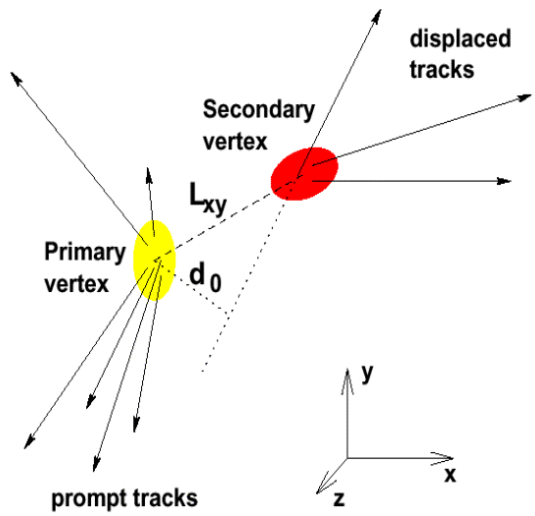

Figure 4.1: Illustration of displaced vertex

and secondary vertex in r-ϕ space, L_{xy}. [55] Figure 4.1 illustrates the concept of d0 and L_{xy}.

The L_{xy} cut requires the significance of the displacement be $\geq$3. Figure 4.2 shows typical L_{xy} and $\sigma_{L_{xy}}$ for taggable B-jets found in $t\bar{t}$ events. In these plots a B-jet is any tight jet which has been matched to a B hadron. The B hadron is found in the truth information retained in each Monte Carlo event.

Jets having vertices which pass this final L_{xy} requirement are B-tagged. The tags are classified depending on where the secondary vertex is located with relation to the jet cone axis. Secondary vertices found to be on the opposite side of the interaction point with respect to the jet cone axis are called "negative" tags. This situation can arise due to track mismeasurements in the detector. Secondary vertices on the same side of the interaction point as the jet cone axis are "positive" tags. Figure 4.3 illustrates the concept of positively and negatively tagged jets. The important thing to remember is that the positive or negative status of the tag does not depend on the direction of the jet itself, but where the secondary vertex is in relation to the jet direction. This analysis only considers positively tagged jets.

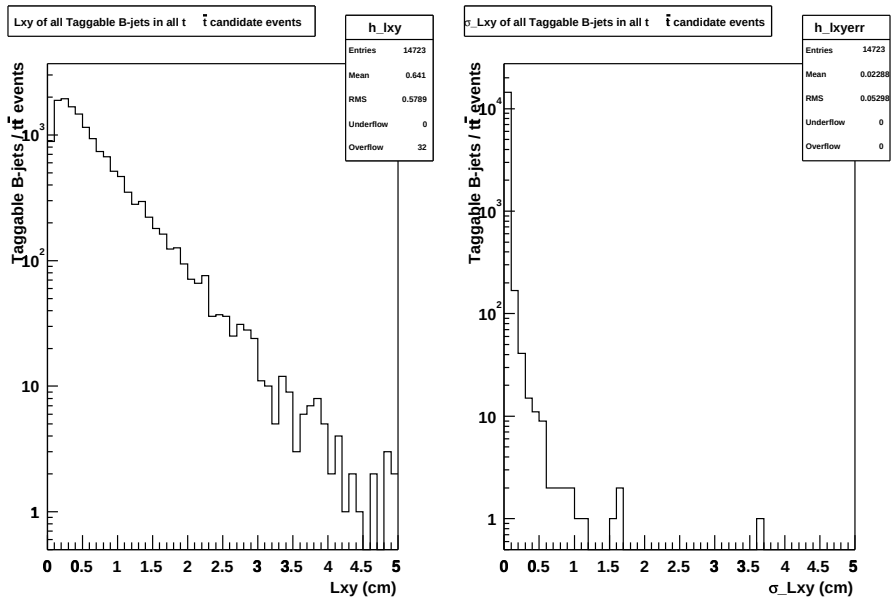

Figure 4.2: Typical values for the $\mid L_{xy} \mid$ (left) and $\sigma_{L_{xy}}$ (right) for taggable b-jets found in $t\bar{t}$ Monte Carlo events.

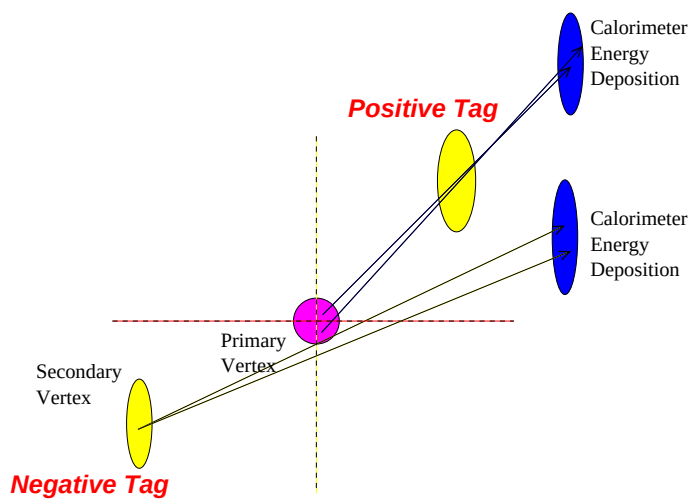

Figure 4.3: Illustration of positively and negatively tagged jets

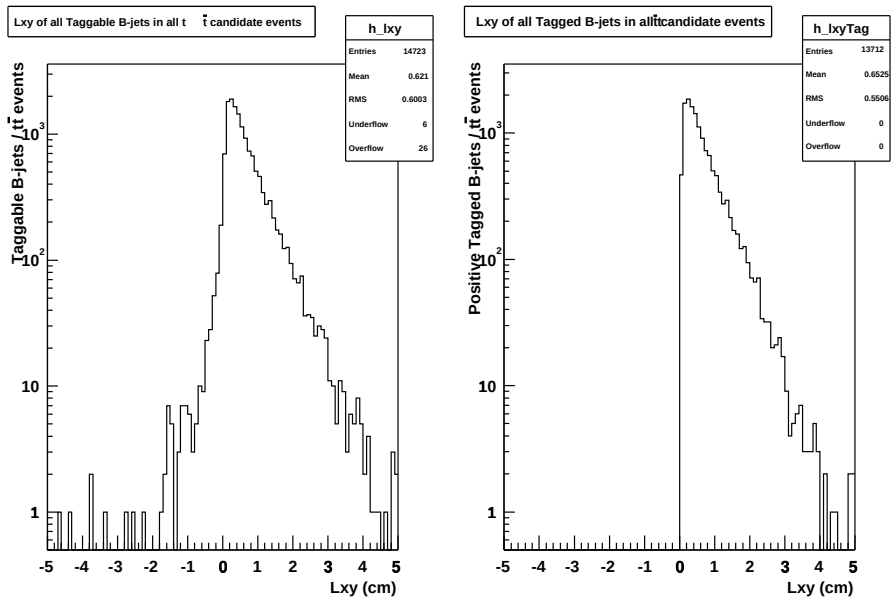

Figure 4.4: L_{xy} of Taggable (left) and Positively Tagged (right) B-jets in Lepton+Jets $t\bar{t}$ Monte Carlo Events

A plot of the L_{xy} for all taggable and positively tagged B-jets in $t\bar{t}$ Monte Carlo events is shown in Figure 4.4. The L_{xy} of positively tagged jets in all candidate data events is shown in Figure 8.4, overlayed with the shape expected from each of the background sources and the expected $t\bar{t}$ shape.

4.3 The B-Tagging Efficiency

The cross section measurement depends on the efficiencies of all of our event selection cuts on $t\bar{t}$ events. We measure the per-event efficiency to tag jets in $t\bar{t}$ events using a Monte Carlo sample. (See Section 6.6) However, what we really need to know is the per-event efficiency to tag a jet in $t\bar{t}$ *data* events.

We can measure the B-tag efficiency in a b-enriched data sample. Unfortunately, we have no data sample which we can use to model the B-tagging efficiency in top quark events, where the P_T of the b-jets is very high. To determine the per-event tagging efficiency in top data events we measure the tagging efficiency in a Monte

Carlo and calibrate this using the b-enriched data sample. We assume the efficiency in the Monte Carlo is linearly related to the efficiency in the data events by a single multiplicative constant, the scale factor :

$$\epsilon_{data} = \epsilon_{Monte\ Carlo} \cdot SF \tag{4.2}$$

The scale factor is measured using data and Monte Carlo samples which are enriched in heavy flavor. The Monte Carlo is a generic $p\overline{p} \rightarrow b\overline{b}$. The data sample is an inclusive electron sample, which means all events in this sample passed the ELECTRON_CENTRAL_8 trigger path. These events have at least one electron with $E_T > 8$ GeV and $P_T > 8$ GeV.

The bottom quarks in $b\overline{b}$ pairs produced in $p\overline{p}$ events travel in opposite directions. These bottom quarks then hadronize. We improve the purity of heavy flavor content in our event samples (both data and Monte Carlo) by choosing events which have back to back jets and evidence of a semi-leptonic decay of a B hadron. Events for both the inclusive electron data and Monte Carlo samples are chosen by requiring there be an electron, a jet associated with the electron (the "electron-jet"), and a jet on the opposite side of the detector from the electron jet, the "away-jet". Table 4.1 lists all of the cuts placed on the electron, electron-jet, and away-jet, along with the value of the cut. Figure 4.5 illustrates the concept of an electron-jet and away-jet.

We select electrons by applying cuts which are similar to some of those used in the tight electron selection : E_T, P_T, E/P ratio, HAD/EM ratio, L_{shr} profile, and a quality cut applied to the track matched to the electron. We include an additional selection cut on the difference between the z position of the electron track and the z position of the primary vertex. This ensures that we are finding an electron which came from the primary vertex. In this study we are looking for semi-leptonic decays

of B hadrons. We require that an electron be found within the cone of a jet. For this reason we place no requirement on the isolation of the electron.

The jet associated with the electron has a minimum E_T requirement. The electron must fall within a cone of $\triangle R < 0.4$ of the centroid of the jet. The away-jet also has a minimum E_T requirement. To ensure optimal tracking and calorimetry we apply a maximum $\mid \eta \mid$ cut on the jet. Finally, to verify that the away-jet is located opposite the electron-jet, we apply a cut on the difference in phi between the two jets. See Table 4.1 for the cut values.

Variable	Value
Good Electron	
E_T	$\geq$ 9.0 GeV
P_T	$\geq$ 4.5 GeV/c
E/P	0.5 $\geq$ E/P $\leq$ 2.0
E_{had}/E_{EM}	$\leq$ 0.05
L_{shr}	$\leq$ 0.2
$\|\Delta z\|$	$\leq$ 5.0 cm
$\|\Delta x\|$	$\leq$ 3.0 cm
$\|z_{ele} - z_{pvtx}\|$	$\leq$ 5.0 cm
Electron-Jets	
E_T	$\geq$ 10.0 GeV
$\triangle R_{electron-jet}$	$\leq$ 0.4
Away-Jets	
E_T	$\geq$ 12.0 GeV
$\|\eta\|$	$\leq$ 1.5
$\triangle\phi_{electron\ jet-away\ jet}$	$\leq$ 2.0 radians

Table 4.1: Selection cuts for electrons, electron-jets, and away-jets in the B-tagging scale factor measurement

Once we have our B-enriched event samples in both data and Monte Carlo we need to measure the B-tag efficiencies for use in the scale factor. This measurement was carried out by a dedicated team at CDF, and their result is used by all B-tagging analyses, including the one presented in this thesis. We briefly summarize the details here for completeness, and refer the interested reader to References [57] and [56].

One way to measure the B-tagging efficiency is by using a double-tag technique

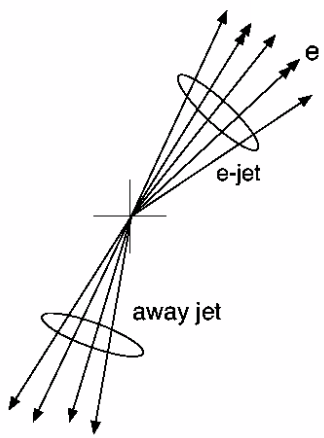

Figure 4.5: Illustration of b-enriched sample : electron, electron-jet, away-jet

that requires all starting events have a tag in the away-jet. We divide the number of events which also have an electron-jet tag by the total number of starting events with an away-jet tag. [57] If all of the events were from direct production of $b\bar{b}$, a tag in the away jet would mean that the electron jet was a b, and this fraction would be our final B-tagging efficiency. In practice, our samples also contains events where the away jet contains b and $\bar{b}$ from gluon splitting and the electron jet is not caused by a semileptonic decay of a B hadron, but is a fake electron from photon conversion. This effect is corrected for by measuring the actual b fraction (F_B) in the electron jets through the procedure of reconstructing $D^0 \rightarrow \pi$ K in the cone around the electron. [56] The above fraction is then multiplied by the b fraction for the final B-tagging efficiency :

$$\epsilon_{B-tag} = \frac{N_{e-jet\ tag\ +\ a-jet\ tag}}{N_{a-jet\ tag}} \cdot \frac{1}{F_B} \tag{4.3}$$

A check on this method is done using a single-tag technique. The single tag efficiency is the number of electron-jets which are tagged, divided by the total number of electron jets in the events.

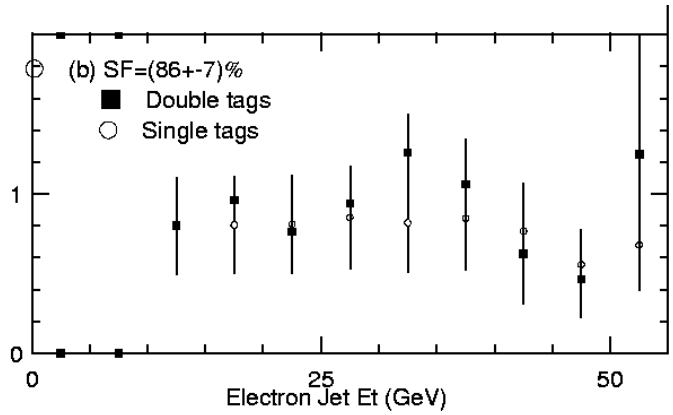

Figure 4.6: B-tagging Scale Factor as a function of jet E_T (GeV). Shown are the calculated scale factors for both the double tag method and the single tag method which is used as a check on the double tag. The scale factor is found to be flat across jet E_T. [7]

The final result of the B-tagging efficiency for the heavy-flavor enhanced data sample is 24.0±1.7%. The efficiency as measured in the Monte Carlo is 28.0±1.0%. The errors on these efficiencies are strictly statistical. The data to Monte Carlo scale factor for the SECVTX tagging algorithm is calculated to be 0.86±0.07. Figure 4.6 shows the scale factor as a function of jet E_T for both the single and double tag methods. The scale factor is considered to be flat across jet E_T. Limited statistics prevent a measurement of the scale factor at larger E_T values.

CHAPTER V

The Cross Section Measurement

5.1 Introduction

The top cross section is measured using :

$$\sigma_{t\bar{t}} = \frac{N_{obs} - N_{bgd}}{\epsilon_{t\bar{t}} \cdot \int Ldt} \tag{5.1}$$

(See Section 1.3.1)

5.2 Candidate Data Events

We use 107.9 pb^{-1} of data for the CEM electrons and CMUP muons and 98.0 pb^{-1} of data for the CMX muons. The number of starting candidate events which passed our trigger bit requirement and good run check is 608917. This is before any additional cuts have been applied to the event. When we require all event selection cuts, with the exception of B-tagging, we find there are only 326 total pre-tag candidate events in this sample. Applying the B-tagging requirement reduces our candidate events by a factor of 10; we are left with 35 total B-tagged candidate events in the ≥ 3 jet bin. These results are broken down into event count for electron and muon events in Table 5.1.

An example of a candidate electron event which has three tight jets, of which two are B-tagged, is shown in Figure 5.1. Starting at $\phi = 0$ and moving counter-clockwise

	Electrons	Muons
Pre-Tag Events	208	118
Single B-Tag Events	17	14
Double B-Tag Events	4	0
Total B-Tag Events	21	14

Table 5.1: Candidate Events

around the display we find a B-tagged jet, a tight jet, the tight electron, the second B-tagged jet, and finally the $\not\!\!E_T$ vector. The values of some kinematic variables for the tight electron and three jets are displayed in Table 5.2. The energy reported for these jets is the raw energy, before corrections. This event has a $\not\!\!E_T$ value of 41.43 GeV, pointing toward $\phi = 6.03$.

	E_T	P_T	$\mid \eta \mid$	ϕ
Electron	52.70 GeV	34.97 GeV	0.128	4.41
Tight Jet	65.21 GeV	64.77 GeV	0.010	2.45
Tagged Jet	60.81 GeV	59.88 GeV	0.808	0.52
Tagged Jet	27.37 GeV	27.24 GeV	1.244	4.53

Table 5.2: Kinematic quantities for the three tight jets and tight electron in the candidate event shown in Figure 5.1.

Table 5.1 values are the N_{obs} needed in Equation 5.1 to calculate the $t\bar{t}$ production cross section. In addition we also need to know N_{bgd}, the number of expected background events, and $\epsilon_{t\bar{t}}$, the total event detection efficiency. A discussion of these two quantities is presented in the following chapters.

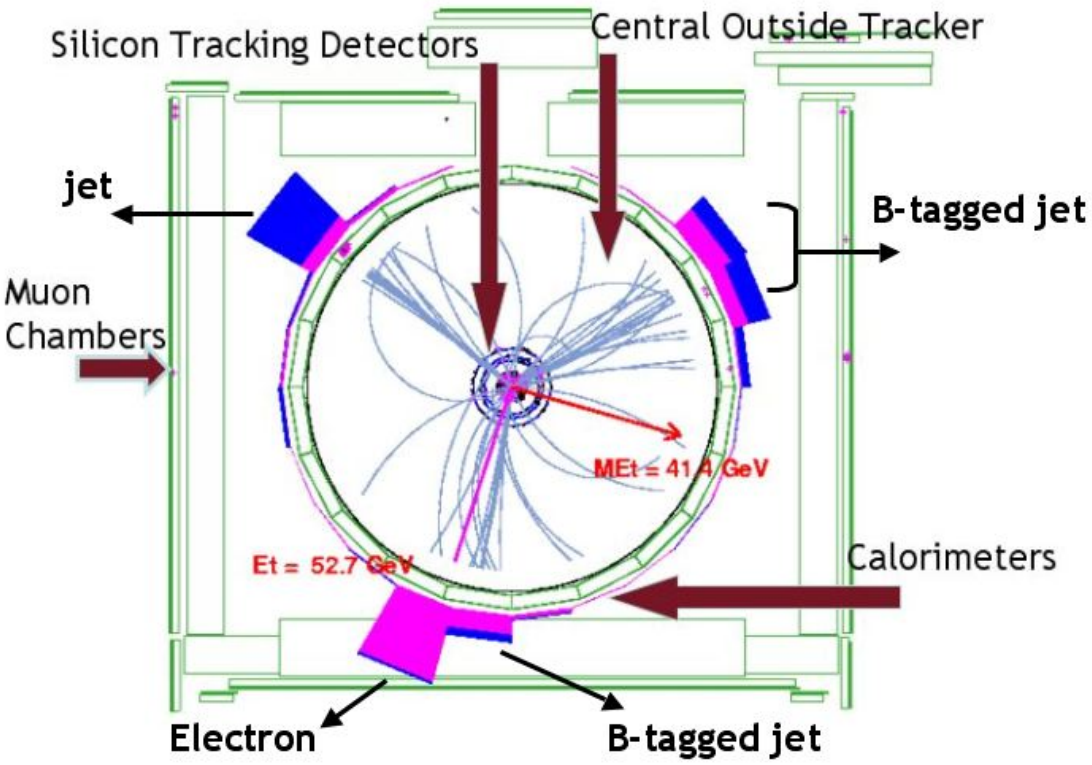

Figure 5.1: Candidate electron event with three tight jets. Two of the three tight jets are B-tagged.

CHAPTER VI

Event Detection Efficiency

6.1 Introduction

The cross section is measured using the following equation :

$$\sigma_{t\bar{t}} = \frac{N_{obs} - N_{bgd}}{\epsilon_{t\bar{t}} \cdot \int L dt} \tag{6.1}$$

$\epsilon_{t\bar{t}}$ is the total event detection efficiency for $t\bar{t}$ events. This is the product of efficiencies for each of the quality cuts made on our events.

$$\epsilon_{t\bar{t}} = A_{t\bar{t}} \cdot \epsilon_{\not{E}_T} \cdot \epsilon_{z0} \cdot \epsilon_{leptonID} \cdot \epsilon_{iso} \cdot \epsilon_{veto} \cdot \epsilon_{trig} \cdot \epsilon_{taggable} \cdot \epsilon_{tag} \tag{6.2}$$

Here $A_{t\bar{t}}$ is the geometric and kinematic acceptance, or fraction of $t\bar{t}$ events passing kinematic cuts and falling within the proper geometry of the detector. The ϵ are efficiencies of the missing E_T cut, z0 cut (applied to the tracks in the leptons, see Section 3.4.1 for details), lepton id cuts, isolation cuts in $t\bar{t}$ events, dilepton veto, Z-boson veto, conversion removal, cosmic veto, trigger efficiency for identifying high E_T/P_T leptons, to tag at least one taggable jet in the event, and to have at least one positive tag in the event.

These efficiencies are measured in Monte Carlo $t\bar{t}$ events which have been run through a detector simulation. They are then multiplied by scale factors to account for differences between the detector and Monte Carlo simulation :

$$\epsilon_{t\bar{t}} = \epsilon_{t\bar{t}}^{MC} \cdot \epsilon_{z0}^{data} \cdot \epsilon_{trig}^{data} \cdot \frac{\epsilon_{leptonID}^{data}}{\epsilon_{leptonID}^{MC}} \cdot \frac{\epsilon_{taggable}^{data}}{\epsilon_{taggable}^{MC}} \cdot \frac{\epsilon_{tag}^{data}}{\epsilon_{tag}^{MC}} \tag{6.3}$$

where $\epsilon_{t\bar{t}}^{MC}$ is the product of efficiencies from Equation 6.2, as measured in the $t\bar{t}$ Monte Carlo sample only.

The denominator of the cross section measurement, $\epsilon_{t\bar{t}} \cdot \int Ldt$, is evaluated separately for each lepton type (CEM electrons, CMUP muons, and CMX muons) :

$$\epsilon_{t\bar{t}} \cdot \int L = \epsilon_{t\bar{t}}^{CEM} \cdot \int L_{CEM} \; + \; \epsilon_{t\bar{t}}^{CMUP} \cdot \int L_{CMUP} \; + \; \epsilon_{t\bar{t}}^{CMX} \cdot \int L_{CMX} \tag{6.4}$$

where the $\epsilon_{t\bar{t}}^{LEP}$ are each the $\epsilon_{t\bar{t}}$ represented by Equation 6.3.

The $\epsilon_{t\bar{t}}^{LEP}$ terms contain several components which are common across all lepton types. These terms are factorized out in order to separate the scale factors and systematic errors which are correlated and uncorrelated :

(6.5)

$$\epsilon_{t\bar{t}} \cdot \int L = \epsilon^{common} \cdot (\epsilon_{t\bar{t}}^{CEM-only} \cdot \int L_{CEM} + \epsilon_{t\bar{t}}^{CMUP-only} \cdot \int L_{CMUP} + \epsilon_{t\bar{t}}^{CMX-only} \cdot \int L_{CMX})$$

In the following sections we will separately examine $\epsilon_{t\bar{t}}^{MC}$ for each of the lepton types, as well as ϵ^{common} and the $\epsilon_{t\bar{t}}^{LEP-only}$ factors.

6.2 $\epsilon_{t\bar{t}}^{MC}$

We measure $\epsilon_{t\bar{t}}$ (See Equation 6.2) in a Monte Carlo sample and then apply scale factors for data to Monte Carlo differences. [65] [66] We lump all terms *except* for ϵ_{tag} together into one product we colloquially call the acceptance. The efficiencies are measured by applying cuts in sequence to events in a $t\bar{t}$ Monte Carlo sample. The order of cuts is listed in Table 6.1, and a description of these cuts is shown below.

Cut	CEM	CMUP	CMX
N_{obsv}	384875	384875	384875
N_{geom}	169223	31688	13890
N_{lepid}	36048	22129	8154
N_{iso}	31685	19281	7183
$N_{\not{E}_T}$	28505	17290	6439
N_{jet}	20074	12136	4509
N_{diveto}	19578	11810	4372
N_{zveto}	18835	11538	4274
$N_{conv\ veto}$	18746	–	–
$\epsilon_{t\bar{t}}^{MC}$	0.0487±0.004	0.0300±0.003	0.0111±0.0002

Table 6.1: Acceptance efficiency cuts for each type of lepton. Quantities are measured in a $t\bar{t}$ Monte Carlo sample. Values shown are events left after applying each cut in sequence.

The Monte Carlo, being a simulation of real life, allows for the primary vertex to be formed along a wide range of z values. To mimic the z0 cut we apply to the data we start with a requirement that the observed particles in the Monte Carlo originate near the primary vertex. This cut is applied to the Monte Carlo truth information (OBSV). We require that the vertex fall within 60 centimeters of the origin of the detector. The number of events passing this veto forms the denominator for all efficiencies. N_{geom} is the number of events within the detector geometry and passing a few most basic cuts. For electrons this means that they are in the fiducial region of the CEM and have $E_T > 20$ GeV. Muons must have either a CMUP or CMX stub and track $P_T > 20$ GeV. Next we apply the remainder of the good lepton ID cuts (See Table 3.1), with the exception of isolation. The isolation cut is applied separately after all other lepton ID cuts. We then move on to event selection cuts : $\not{E}_T$, number of tight jets in the event, dilepton veto, z veto, and conversion removal for electrons. Muons have the cosmic ray veto applied as part of the lepton ID cuts.

6.3 Individual Lepton Scale Factors and Uncertainties ($\epsilon_{t\bar{t}}^{LEP-only}$)

We measure the trigger efficiency and ID efficiency for each of our lepton types. The high P_T central electron ID efficiencies are measured in Z→ee events. The event sample must be selected in such a way as to ensure that each event came from a real Z decay. Z events are selected by choosing events in which an electron and any second object in the event (opposite sign electron, reclustered jet with small number of tracks, opposite signed track) form an invariant mass in a window around the Z mass peak. In these events the first leg of the Z must be a tight electron and the second leg is used to measure the efficiency of tight and loose electron cuts. [67] The high E_T central electron trigger efficiency uses both the ELECTRON_CENTRAL_18 trigger path that is used in this analysis, and the "W-No Track" trigger. The W-No Track trigger has the same calorimeter requirements as the ELECTRON_CENTRAL_18 trigger path, but does not require a track be associated with the calorimeter cluster. This allows one to measure the trigger efficiency including tracking. [68]

The muon trigger efficiencies are measured in $Z \rightarrow \mu\mu$ events, where both muons pass the tight lepton cuts. Muon ID efficiencies are also measured in $Z \rightarrow \mu\mu$ events, where the first leg of the Z can be either a loose CMUP or CMX muon and the only requirement on the second leg is that it is of opposite sign and that the reconstructed Z mass of the pair fall within the Z mass window cut. The second leg of the Z is used to measure the efficiency. Muon reconstruction efficiencies are measured using J/ψ events which have been collected with a muon+silicon track trigger. These are cross-checked using $Z \rightarrow \mu\mu$ events. [69] [70]

We multiply these efficiencies by the $\epsilon_{t\bar{t}}^{MC}$ value shown in the last line of Table 6.1 to get our final result for each lepton type, $\epsilon_{t\bar{t}}^{LEP-only}$ (See Equation 6.5). Values for

the individual leptons are shown in Table 6.2.

	CEM	CMUP	CMX
$\epsilon_{t\bar{t}}^{MC}$	0.0487±0.004	0.0300±0.003	0.0111±0.0002
$\epsilon_{trigger}$	0.968±0.001	0.904±0.012	0.901±0.016
$\epsilon_{leptonID}$	0.990±0.008	0.937±0.011	1.005±0.013
Muon Reconstruction	—	0.962±0.022	0.978±0.025
$\epsilon_{t\bar{t}}^{LEP-only}$	0.0466±0.0009	0.0244±0.0008	0.0091±0.033

Table 6.2: Individual lepton efficiencies, including systematic errors

Sources of systematic uncertainties for the CEM electrons come from the conversion veto (1.5%), the E_T scale and resolution of the calorimeter, and the amount of material in the calorimeter (total 0.3%). These systematic uncertainties are studied in the $We\nu$ cross section analysis. [71] Systematic uncertainties on the muons come from uncertainties in the P_T scale and resolution, and from understanding the complicated muon geometry of our detector (1.2% for CMUP and CMX each). The systematic uncertainties from muon events is measured in the $W\mu\nu$ cross section analysis. [72]

6.4 Common Scale Factors and Systematic Uncertainties

The scale factors for the Z vertex cut and the track finding efficiency are common to electrons and muons. These scale factors are taken from W cross section analyses. [71] [73] The z0 efficiency is 0.951±0.001 (stat) ±0.005 (sys). The track finding efficiency is 1±0.004 for both electrons and muons. Systematic errors common to all leptons come from many sources : Monte Carlo generator differences, initial and final state radiation in our generators, particle distribution functions (PDF's), and from the jet energy scale.

A common source of systematic error is the Monte Carlo generator used to create our $t\bar{t}$ samples. Samples created with HERWIG and PYTHIA were compared for

this analysis. There are two main differences between these generators. HERWIG uses a theory value for the branching ratio of $W \rightarrow l\nu$ while PYTHIA uses a measured value from LEP. Electrons resulting from hadronic interactions are capable of radiating photons through the process of QED final-state radiation. PYTHIA allows electrons to radiate photons, while HERWIG does not. PYTHIA was used for our central values of the efficiency measurements and we assigned a 1.4% systematic error due to differences in these two generators. This error is found by weighting the individual uncertainties on PYTHIA and HERWIG by their contribution to the acceptance. Internal to PYTHIA we examined systematic errors due to initial and final state radiation. The amount of initial and final state radiation permitted is varied. The effect on the efficiency is found using a PYTHIA Monte Carlo which has no initial or final state radiation, and a sample which has both turned on. The systematic error is found by taking the difference of the efficiency found using these two samples and dividing by two. This systematic error is on the order of 2.6%. PDF's also contribute an additional 5.6% to our systematic error. These systematics were studied extensively by University of Michigan postdoctoral researcher, Dr. Ken Bloom. [48] The jet-energy scale contributes 2.5% uncertainty to the systematic error.

The final ϵ^{common} is calculated to be 0.951±0.062.

6.5 Final Acceptance and Luminosity Results

The luminosity for our data samples is calculated using information obtained from the CLC detector, and Equation 2.3. (See Section 2.2.1) The total error on the luminosity comes from a variety of sources. There is a 4.4% error associated with the uncertainty on the proton anti-proton inelastic cross section used to measure the

luminosity ($\sigma_{p\bar{p}}$). There are several other sources of error, each contributing less than 1% :

- Errors associated with the CLC acceptance measurement (ϵ_{CLC})
  - due to the Monte Carlo generator used to create the event sample which was used to measure the acceptance
  - due to parameters used for the CLC during generation time of the event sample
- The choice of the method used to calculate the luminosity
- Errors due to differences in beam conditions over time
- Errors due to gain changes in the PMTs over time
- Errors due to beam losses

The total contribution from these errors is 4%. Adding all errors in quadrature results in a total error on the luminosity measurement of 6%. The final results for each lepton type and the luminosity of the corresponding data sample are shown in Table 6.3. $\epsilon_{t\bar{t}}$ *does not* yet include the tagging efficiency.

Cut	CEM	CMUP	CMX
$\epsilon_{t\bar{t}}^{LEP-only}$	0.0466±0.0009	0.0244±0.0008	0.0091±0.033
ϵ^{common}		0.951±0.062	
$\epsilon_{t\bar{t}}$	0.044±0.003	0.023±0.002	0.009±0.0001
$\int L\ (pb^{-1})$	107.9±6.4	107.9±6.4	98.0±5.8

Table 6.3: Final acceptance and luminosity for each lepton type. *Results do not include the tagging efficiency*

6.6 Tagging Efficiency

ϵ_{tag} is the probability to tag at least one jet in a top event. Top events contain both jets coming from b decays and those coming from the W, which can have charm

or non-heavy flavor (up, down quarks). Because charm hadrons have a measurable lifetime, and because tagging mistakes can create false vertices, the SECVTX tagging algorithm will tag jets which did not come from B decays. The total event tagging efficiency, then, is the sum of the efficiency to tag a B-jet and the efficiency to tag a non-B jet. From this must be subtracted a correction factor to account for overlap between events which contain both b and non-B jets :

$$\epsilon_{tag} = \epsilon_{B-tag} + \epsilon_{non-B} - (\epsilon_{B-tag} \cdot \epsilon_{non-B}) \tag{6.6}$$

where the non-B efficiency is the probability to tag a charm jet plus the probability to tag a non-heavy flavor jet :

$$\epsilon_{non-B} = \epsilon_{ctag} + \epsilon_{nhf} \tag{6.7}$$

6.6.1 Measurement of ϵ_{tag}

For the B-jets, c-jets, and non-heavy flavor jets we measure the efficiency to identify these jets, find taggable jets, and find tagged jets, on a per-jet and per-event basis. The values reported are for events passing all of our selection criterion, with $\geq$ *3 tight jets*, where *tagged* refers only to positive tags.

Event B-Tagging Efficiency

The B-tagging efficiency may be further factorized. [74] [77] Top events should produce two b quarks, which should show up in our detector as two B-jets. Sometimes, however, only one B-jet will be contained in the central portion of our detector. The B-tagging efficiency needs to take into account situations where we find either one or both of the B-jets in a top event. The B-tagging efficiency is the sum of the

following probabilities : the probability to tag only one B-jet in the event when only one B-jet is found in the central portion of the detector, the probability to tag only one B-jet when two B-jets are found in the detector, and the probability to tag two B-jets when both are found.

The tagging efficiencies are measured in a $t\bar{t}$ Monte Carlo, where we know the flavor content of jets in top events. As discussed in Section 4.3, the SECVTX tagging algorithm will perform differently in data and Monte Carlo. We account for this difference by introducing a scale factor, or ratio of SECVTX tagging efficiencies between data and Monte Carlo. [57] The formula for the total B-tagging efficiency per event is then :

$$\epsilon_{B-tag}^{event} = F_{1b} \cdot \epsilon_{B-tag} \cdot SF + F_{2b} \cdot \epsilon_{B-tag}^{2} \cdot SF^{2} + 2 \cdot F_{2b} \cdot \epsilon_{B-tag} \cdot SF \cdot (1 - \epsilon_{B-tag}) \tag{6.8}$$

F_{1b} is the fraction of top events with 1 taggable B-jet, F_{2b} is the fraction of top events with 2 taggable B-jets, SF is the scale factor for the SECVTX tagging algorithm between data and Monte Carlo, and ϵ_{B-tag} is the per jet B-tagging efficiency, as measured in Monte Carlo.

- $F_{1b} \cdot \epsilon_{B-tag} \cdot SF$ is the probability to tag one B-jet when only one is found
- $F_{2b} \cdot \epsilon_{B-tag}^{2} \cdot SF^{2}$ is the probability to tag both B-jets when two are found
- $F_{2b} \cdot \epsilon_{B-tag} \cdot SF \cdot (1 - \epsilon_{B-tag})$ is the probability to tag one B-jet when two are found. This factor is multiplied by two, as there are two cases in which only one of the two B-jets found can be tagged.

B-jets are found by matching a B meson to a tight jet. We identify B mesons in the Monte Carlo by examining the truth (HEPG) information, where each particle is assigned a number which is directly related to its identity. [76] The matching is

done by requiring that the B meson fall within a cone of $\triangle R < 0.4$ of the jet axis. During the course of this analysis we measured the following efficiencies :

- Efficiency to find a B-jet
  - per jet: number of B's matched to jets / total number of B's to start
  - per event : number of events with ≥ 1 B matched to a jet / total pre-tag candidate events
- Efficiency to find a taggable B-jet
  - per jet: number of taggable B-jets / number of B's matched to jets
  - per event : number of events with ≥ 1 taggable B-jet / total pre-tag candidate events
- Efficiency to find a tagged B-jet
  - per jet : number of tagged B-jets / number of taggable B-jets
  - per event : number of events with ≥ 1 tagged B-jet / total pre-tag candidate events

The values for these efficiencies are displayed in Table 6.4, in percent. Errors included are strictly statistical. We find that our matching scheme is 88% efficient on a per-jet basis, and 99% efficient on a per-event basis. Our tagger is 50% efficient per B-jet to find a tag in the jet.

Values for each of the components from equation 6.8 are shown in Table 6.5, along with the final per-event B-tagging efficiency found using the factorization method. A discussion of the calculation of systematic errors may be found in Section 6.6.2. The final B-tagging efficiency is 53%. We applied a simple counting method as a check of our calculation of the event B-tagging efficiency. For this check we simply

B-jets	
	Efficiency to find jet (%)
per jet	87.6±0.48
per event	99.2±0.76
	Efficiency to find a taggable jet (%)
per jet	78.1±0.48
per event	88.7±0.70
	Efficiency to find a tagged jet (%)
per jet	53.9±0.42
per event	60.0±0.53

Table 6.4: Efficiencies measured during this analysis for B-jets. These efficiencies are shown on a per jet and per event basis. Errors shown are strictly statistical.

counted the number of events with at least one positively tagged B-jet, and divided by the number of pre-tag candidate events. Multiplying by the scale factor will, to first order, give us a good approximation of the event B-tagging efficiency. For this check we use the numbers quoted in table 6.4, "Efficiency to find a tagged jet : per event ". The only systematic uncertainty included on this number is that coming from the scale factor. We find a final value of 51.6±0.53±7%, in good agreement with 53.4±0.82±5.9% calculated using the factorization method.

Result	
F_{1b} (%)	39.3±0.40±0.95
F_{2b} (%)	49.4±0.46±1.65
SF	0.86 ± 0.07 (sys)
ϵ_{B-tag} (%)	53.9±0.42 (stat)
ϵ^{event}_{B-tag}	53.4±0.82($stat$)±5.9(sys)

Table 6.5: Per-Event B-tagging Efficiency (ϵ^{event}_{B-tag}).

Event Mistag Efficiency

For the charm-tagging efficiency and the non-heavy flavor efficiencies we perform a simple counting experiment : we count the number of total events with c-jets (non-hf jets) having positive tags, and divide by the number of pre-tag events with c-jets (non-hf jets). This number is then multiplied by the scale factor. It is important to

note that here we use the same scale factor as that for B-jets, 0.86±0.07.

Once we have a starting set of pre-tag candidate events we examine the quark content of the tight jets. We look at the Monte Carlo truth information and match B mesons to the tight jets with a cone of $\triangle$R < 0.4. (See equation 6.10) If we find a match we call the jet a B-jet, and use this jet to measure ϵ^{event}_{B-tag}. If there are no B's near the jet but we are instead able to match to a charm quark, we use this jet for ϵ_{ctag}. If we cannot match a heavy flavor particle (B hadron or charm quark) to the jet, then this jet is called a non-heavy flavor jet.

ϵ_{ctag} and ϵ_{nhftag} are measured in the following way :

$$\epsilon = \frac{Number\ events\ with\ P\ tagged\ jet}{Number\ pretag\ candidate\ events} \cdot SF \tag{6.9}$$

Each of these efficiencies contains systematic errors from calorimeter jet energy corrections and from matching the HEPG particle to jets. (See Section 6.6.2.)

Charm jets are identified by matching charm quarks in the HEPG bank to a tight, corrected jet in a cone of $\triangle$R < 0.4. During the course of this analysis we measured the following efficiencies :

- Efficiency to find a charm jet
  - per jet: number of charm quarks matched to jets / total number of charm quarks to start
  - per event : number of events with ≥ 1 charm quark matched to a jet / total pre-tag candidate events
- Efficiency to find a taggable charm jet
  - per jet: number of taggable charm jets / number of charm quarks matched to jets

- per event : number of events with ≥ 1 taggable charm jet / total pre-tag candidate events

- Efficiency to find a tagged charm jet
  - per jet : number of tagged charm jets / number of taggable charm jets
  - per event : number of events with ≥ 1 tagged charm jet / total pre-tag candidate events

The values for these efficiencies are displayed in Table 6.6, in percent. Errors included are strictly statistical. We find that our matching scheme is 82% efficient on a per-jet basis, and 34% efficient on a per-event basis. Our tagger is 12% efficient per charm jet to find a tag in the jet. The final per-event efficiency to tag a charm jet, including the scale factor for tagging, is shown in the last row of Table 6.6.

C-jets

	Efficiency to find jet (%)
per jet	82.2±1.00
per event	35.9 ±0.38
	Efficiency to find a taggable jet (%)
per jet	76.8±1.0
per event	27.6±0.32
	Efficiency to find a tagged jet (%)
per jet	12.0±0.38
per event	3.31±0.10
	Final Event Charm Jet Tagging Efficiency (%)
$\epsilon_{jet}\cdot$ SF	2.84±0.10 (stat)±0.14 (sys)

Table 6.6: Efficiencies measured during this analysis for charm jets. These efficiencies are shown on a per jet and per event basis. Errors shown are strictly statistical. The final per-event charm jet tagging efficiency is shown in the last row, and includes both statistical and systematic errors.

Non-heavy flavor jets are all jets *not* matched to a B meson or a charm quark. During the course of this analysis we measured the following efficiencies :

- Efficiency to find a non-heavy flavor jet
  - per jet : number of non-heavy flavor jets / total number of tight jets

  - per event : number of events with ≥ 1 non-heavy flavor jet / total pre-tag candidate events

- Efficiency to find a taggable non-heavy flavor jet
  - per jet : number of taggable non-heavy flavor jets / number of non-heavy flavor jets

- Efficiency to find a tagged non-heavy flavor jet
  - per jet : number of tagged non-heavy flavor jets / number of taggable non-heavy flavor jets
  - per event : number of events with ≥ 1 tagged non-heavy flavor jet / total pre-tag candidate events

The values for these efficiencies are displayed in Table 6.7, in percent. Errors included are strictly statistical. We find that 42% of the time we find a non-heavy flavor jet - i.e. 58% of the time we are able to match either a B meson or a charm quark to the tight, central jets in our $t\bar{t}$ events. Our tagger is less than 1% efficient in finding a tag in non-heavy flavor jets. The final per-event efficiency to tag a non-heavy flavor jet, including the scale factor for tagging, is shown in the last row of Table 6.7. We find a much higher systematic error due to matching in the non-heavy flavor jets. Please see Section 6.6.2 for a discussion of the systematic errors.

6.6.2 Systematic Uncertainties

This analysis relies on our ability to properly identify jets as coming from B's. One can imagine that tightening the cone around the jet when matching to a particle would affect our counting and thus our final result. To account for this we examine the $\triangle$R used when matching a HEPG particle to jets as one source of systematic error. $\triangle$R is defined as :

NHF-jets

	Efficiency to find jet (%)
per jet	42.4±0.22
per event	93.7±0.72
	Efficiency to find a taggable jet (%)
per jet	70.2±0.47
	Efficiency to find a tagged jet (%)
per jet	0.94±0.05
per event	1.03±0.055
	Final Event NHF-jet Tagging Efficiency (%)
$\epsilon_{jet}\cdot$ SF	0.89±0.055 (stat)±0.7(sys)

Table 6.7: Efficiencies measured during this analysis for non-Heavy Flavor jets. These efficiencies are shown on a per jet and per event basis. Errors shown are strictly statistical. The final per-event non-heavy flavor jet tagging efficiency is shown in the last row, and includes both statistical and systematic errors.

$$\triangle R = \sqrt{(\mid \phi_{B(c)} - \phi_{jet} \mid)^2 + (\mid \eta_{B(c)} - \eta_{jet} \mid)^2} \tag{6.10}$$

We calculate the systematic uncertainty on our matching by changing $\triangle$R to 0.2 and repeating the analysis. The systematic uncertainty is :

$$\sigma_{\triangle R}(sys) = \frac{Value\ using\ \triangle R < 0.4 - Value\ using\ \triangle R < 0.2}{2} \tag{6.11}$$

As we shrink the $\triangle$R used to match HEPG particles to jets we lower the number of bottom and charm quarks matched to jets. This increases the number of non-heavy flavor jets, thus increasing the systematic uncertainty on the non-heavy flavor tagging efficiency.

In addition, fluctuations in the energy scale of our calorimeter could allow jets to float around our E_T cut; jets that should be above our cut, for example, might have an E_T recorded that is below our threshold. We use a method prescribed for varying the jet energy corrections to find the systematic. [75]

We attach a systematic uncertainty from $\triangle$R and the jet energy corrections to ϵ_{ctag} and ϵ_{nhf}, and to F_{1b} and F_{2b} from our B-tagging efficiency. The per B-jet tagging

	Result
$\epsilon_{cjet}\cdot$ SF	2.84±0.10 (stat)±0.14 (sys)
$\epsilon_{nhfjet}\cdot$ SF	0.89±0.055 (stat)±0.7(sys)
$\epsilon_{non-Bjet}$	3.73±0.11(stat) ±0.71(sys)
ϵ^{event}_{B-tag}	53.4±0.82($stat$)±5.9(sys)
ϵ_{tag}	55.0±0.83 (stat)±6.0 (sys)

Table 6.8: Final efficiency to tag at least one jet in a top event.

efficiency, ϵ_{B-tag} should not exhibit any dependence on $\triangle$R. The scale factor we use is given to us with a systematic error due to the jet corrections already attached. The per-jet B-tagging efficiency, ϵ_{B-tag}, is always multiplied by the scale factor, and the systematic uncertainty on the scale factor dwarfs the small correction to ϵ_{B-tag} due to jet energy systematic uncertainty uncertainties. As a result, we quote no systematic errors for ϵ_{B-tag}.

6.6.3 Results

Table 6.8 shows our event B-tagging, c-tagging, and non-heavy flavor tagging efficiencies. The final row is our total event tagging efficiency, ϵ_{tag}, which is used in the denominator of the cross section. We find the efficiency to tag any jet in a $t\bar{t}$ event is 55%.

6.7 Event Detection Efficiency Final Result

The final result for the entire denominator of the cross section equation is shown in Table 6.9. We multiply the per-jet tagging efficiency, the luminosity, and the event detection efficiency for each of our three lepton types. These three numbers are then summed together and the individual errors are added in quadrature to get our final result of 4.47 ± 0.30 (stat) ± 0.49 (sys) pb^{-1}. The intermediate step of calculating $\epsilon_{t\bar{t}} \cdot \int Ldt$ without tagging has been shown in row three of Table 6.9.

Here all correlations due to luminosity have been accounted for. [65]

Cut	CEM	CMUP	CMX
$\epsilon_{t\bar{t}}$	0.044±0.003 (sys)	0.023±0.002 (sys)	0.009±0.0001 (sys)
$\int L\ (pb^{-1})$	107.9±6.4 (sys)	107.9±6.4 (sys)	98.0±5.8 (sys)
Before Tagging	8.14 ± 0.55 (stat) ± 0.49 (sys) pb^{-1}		
ϵ_{tag}	0.55 ± 0.0083 (stat) ± 0.06 (sys)		
$\epsilon_{t\bar{t}} \cdot \int Ldt$	4.47 ± 0.30 (stat) ± 0.49 (sys) pb^{-1}		

Table 6.9: Final event detection efficiency. The final row in this table corresponds to the entire denominator of Equation 1.9

CHAPTER VII

Backgrounds

Backgrounds are processes which produce signatures similar to those coming from lepton+jets $t\bar{t}$ events: large $\not\!\!E_T$, a tight lepton, and tagged jets. This signature may be produced from both QCD and electroweak processes, and can occur in events with and without a real W boson.

Our estimation and discussion of these backgrounds groups them by mechanism: backgrounds which arise due to electroweak processes (WW, WZ, ZZ, Z$\rightarrow \tau\tau$, single top), backgrounds from events with a real W from electroweak processes and heavy flavor due to QCD gluon fusion/splitting ($Wb\bar{b}, Wc\bar{c}, Wc$), backgrounds occurring due to mismeasurements in tracking (Mistags), and backgrounds due to QCD processes which do not contain a real W boson in the event (QCD).

A summary of expected contributions from each background, broken down by jet bin, is given in Table 7.20.

7.1 QCD

The QCD backgrounds are events which have a large $\not\!\!E_T$ and an identified lepton that did not result from a real W decay. The lepton can be faked in situations where a photon conversion is misidentified as an electron, or a pion travels through the calorimeter and arrives in the muon chambers with enough energy remaining to

cause it to be misidentified as a muon. One source of real leptons in these events are semi-leptonic B hadron decays, where the B hadron is not the result of a top quark decay. Large $\not\!\!E_T$ occurs in situations where jets are mismeasured, or when a portion of a jet lands in a crack between the wedges in the calorimeter. The size of the QCD background is estimated by examining the $\not\!\!E_T$ and isolation behavior of lepton candidate events in data. [63]

The measurement of this background relies on the fact that the isolation of the tight lepton and the event $\not\!\!E_T$ are uncorrelated in the background QCD events, but are highly correlated in $t\bar{t}$ events. This means that the $\not\!\!E_T$ spectrum of the non-isolated QCD background events looks the same as the $\not\!\!E_T$ spectrum found in isolated QCD background events. The non-isolated events are enriched in QCD events. This allows us to study the event distribution across $\not\!\!E_T$ for the non-isolated QCD events, and extrapolate this information into the isolated, or signal, region. This method is the "$\not\!\!E_T$ vs Isolation" method.

The "$\not\!\!E_T$ vs Isolation" calculation divides the $\not\!\!E_T$ and lepton isolation plane into four quadrants:

- A : non-isolated lepton, low $\not\!\!E_T$
- C : non-isolated lepton, high $\not\!\!E_T$
- B : isolated lepton, low $\not\!\!E_T$
- D : isolated lepton, high $\not\!\!E_T$

where isolated is defined as <0.1, non-isolation occurs at > 0.2, low $\not\!\!E_T$ is $<$ 15 GeV, and high $\not\!\!E_T$ is > 20 GeV. (See Figure 7.1) Region D contains the signal events. These quadrants are populated by high P_T lepton candidate events in the data, before applying the $\not\!\!E_T$ or lepton isolation cuts.

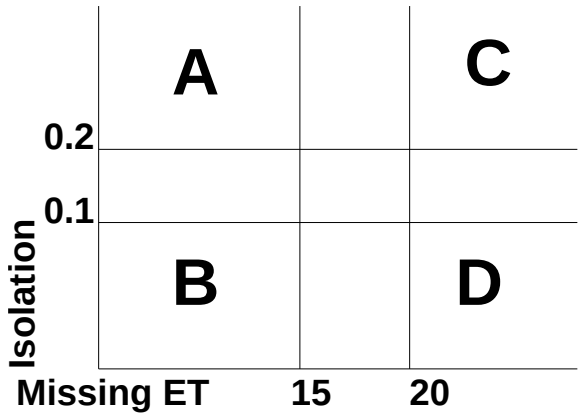

Figure 7.1: $\not\!\!E_T$ vs Isolation space for QCD background estimate

The presumption of the method is that the number of background events in region D, relative to region C, is the same as the ratio of events in the "all-background" regions B and A :

$$\frac{N_D}{N_C} = \frac{N_B}{N_A} \tag{7.1}$$

We need to understand, however, how much of the pre-tag background feeds into the tagged sample. We do this in two ways.

1. We calculate how many of the pre-tag QCD events in region D would be tagged. This requires a tagging rate which is appropriate for the b-fraction of events found in region D. We will assume this is the same as the tag rate in region B, as the events in regions D and B will be affected by the isolation cut in the same way. The tagging efficiency as measured in region B is shown in Table 7.1, for muon and electron events separately.

The number of tagged events expected from the QCD background is then found using the following equation :

$$N_{QCD} = F_{QCD} \cdot \epsilon_B \cdot N_D \tag{7.2}$$

$$\sigma^2_{N_{QCD}} = N^2_{QCD} \cdot [(\frac{\sigma_{F_{QCD}}}{F_{QCD}})^2 + (\frac{\sigma_{\epsilon_B}}{\epsilon_B})^2 + (\frac{\sigma_{N_D}}{N_D})^2] \tag{7.3}$$

F_{QCD} is the fraction of QCD events in the data sample which pass all event cuts except those on $\not\!\!E_T$ and lepton isolation, ϵ_B is the tagging rate in region B, and N_D is the number of taggable jets in region D. ϵ_B is measured by dividing the number of tagged jets found in region B by the number of taggable jets in region B. F_{QCD} is found by taking the ratio of events in regions B and C to those found in regions A and D :

$$F_{QCD} = \frac{B \cdot C}{A \cdot D} \tag{7.4}$$

Strictly speaking, Equation 7.3 is not the proper way to calculate the error; F_{QCD} and N_D are correlated, and F_{QCD} and ϵ_{tag} are correlated. However, we assign a 50% systematic error to F_{QCD}. This allows F_{QCD} to be considered uncorrelated with N_D and ϵ_{tag}, and Equation 7.3 to stand as a valid method of calculating the error on this background.

Components of Equation 7.3 are shown in Table 7.1 for the pre-tag data sample. Information is separated by jet bin and by lepton type.

2. We don't really know if the tagging efficiency in region B represents the tag rate in region D. The second way in which the QCD background is measured is to apply the $\not\!\!E_T$ versus Isolation method to the tagged events found in the W+jets data sample. The limited statistics in this method require that the isolation cuts be

	1 Jet	2 Jet	3 Jet	≥3 Jet
	Electrons			
F_{QCD}	0.135 ± 0.068	0.18 ± 0.09	0.20 ± 0.10	0.20 ± 0.10
ϵ_B	0.021 ± 0.001	0.026 ± 0.003		
N_D	3374	1101	290	158
$N_{QCD\ ele}$	9.57 ± 4.84	5.15 ± 2.65	1.51 ± 0.78	0.82 ± 0.43
	Muons			
F_{QCD}	0.04 ± 0.02	0.05 ± 0.02	0.10 ± 0.05	0.10 ± 0.05
ϵ_B	0.030 ± 0.004	0.04 ± 0.01		
N_D	2423	810	169	65
$N_{QCD\ muo}$	2.91 ± 1.51	1.62 ± 0.77	0.68 ± 0.38	0.26 ± 0.15

Table 7.1: QCD background estimates for electrons and muons, found using the pre-tag data sample. Results are separated by jet bin.

changed slightly from the values used for the pre-tag sample. The isolated region is defined as that with isolation < 0.1, while non-isolated leptons have isolation of $>$ 0.1. Final results using this sample are shown in Table 7.2.

	1 Jet	2 Jet	3 Jet	≥3 Jet
	Electrons			
$N_{QCD\ ele}$	13.8 ± 2.1	6.3 ± 1.5	2.8 ± 0.7	1.5 ± 0.4
	Muons			
$N_{QCD\ muo}$	3.1 ± 0.7	2.2 ± 0.7	1.0 ± 0.4	0.40 ± 0.10

Table 7.2: QCD background estimates for electrons and muons, found using the tagged data sample. Results are separated by jet bin.

To get the final estimated QCD background for the electron(muon) events, we create a weighted sum of the electron(muon) estimates found using the pre-tag and tagged data samples [62] :

$$N_{QCD\ weighted} = \frac{N_{QCD\ pre-tagged} \cdot \sigma^2_{N_{QCD\ tagged}} + N_{QCD\ tagged} \cdot \sigma^2_{N_{QCD\ pre-tagged}}}{\sigma^2_{N_{QCD\ tagged}} + \sigma^2_{N_{QCD\ pre-tagged}}} \tag{7.5}$$

$$\sigma^2_{N_{QCD\ weighted}} = \frac{\sigma^2_{N_{QCD\ pre-tagged}} \cdot \sigma^2_{N_{QCD\ tagged}}}{\sigma^2_{N_{QCD\ tagged}} + \sigma^2_{N_{QCD\ pre-tagged}}} \tag{7.6}$$

The electron and muon weighted sums are then summed linearly to give our final result:

$$N_{QCD\ total} = N_{QCD\ weighted\ electrons} + N_{QCD\ weighted\ muons} \tag{7.7}$$

$$\sigma^2_{N_{QCD\ total}} = \sigma^2_{N_{QCD\ weighted\ electrons}} + \sigma^2_{N_{QCD\ weighted\ muons}} \tag{7.8}$$

Results for the weighted sum of the electron and muon QCD events, as well as the final expected QCD background, per jet bin, are shown in Table 7.3.

	1 Jet	2 Jet	3 Jet	≥3 Jet
N_{QCD} (Electrons)	13.13 ± 1.93	6.02 ± 1.31	2.22 ± 0.52	1.18 ± 0.29
N_{QCD} (Muons)	3.07 ± 0.64	1.94 ± 0.52	0.83 ± 0.28	0.36 ± 0.08
$N_{QCD\ total}$	16.20 ± 2.03	7.96 ± 1.40	3.05 ± 0.59	1.54 ± 0.30

Table 7.3: Final results for the expected contribution from the QCD background, as a function of jet bin. These final results are found by combining the results from the pre-tagged and tagged data samples, for electrons and muons separately, using a weighted average. The two weighted averages are then summed together linearly.

7.2 Real W + Heavy Flavor

7.2.1 Basic Strategy

W+heavy flavor backgrounds are events which contain a real W boson and QCD processes which produce heavy flavor (bottom or charm) in the event. There are three such backgrounds to the $t\bar{t}$ production cross section measurement : W$b\bar{b}$, W$c\bar{c}$, and Wc.

An example of $Wb\bar{b}$ production is shown in Figure 7.2, which displays the zeroth order production of $Wb\bar{b}$ due to gluon splitting. More complicated diagrams with additional gluons are also possible. Gluons couple strongly, so the addition of higher orders does not necessarily allow a calculated cross section to converge in perturbation theory. For this reason it is very difficult to precisely calculate an absolute QCD cross section. To determine the number of expected events from each of these backgrounds we cannot use the calculated theoretical cross section.

However, a ratio of W+heavy flavor and inclusive W+jets cross sections should cancel these complications. This ratio, called the heavy flavor fraction, allows us to predict the amount of heavy flavor backgrounds expected using the measured event rates. The number of pre-tag W candidate events observed in data in each jet bin is multiplied by the heavy flavor fraction to give the expected amount of each background event. Further, multiplying by the heavy flavor tagging rate and the B-tag scale factor gives us the expected contribution in the final tagged sample :

$$N_{WHF} = N_W \cdot (1 - F_{QCD}) \cdot F_{WHF} \cdot \epsilon_{tag} \cdot SF \tag{7.9}$$

- N_{WHF} is the number of expected background events from W+heavy flavor (W+HF) : W$b\bar{b}$, W$c\bar{c}$, or Wc
- N_W is the total number of pre-tag candidate events found in our W+jets data sample (See Table 7.4)
- (1 - F_{QCD}) is the fraction of pre-tag candidate events which contain real W's (See Table 7.1 for F_{QCD})
- F_{WHF} is the heavy flavor fraction, or fraction of W+HF events in all W+jet events
- ϵ_{tag} is the tagging efficiency as measured in the W+HF Monte Carlo sample
- SF is the data to Monte Carlo scale factor for the SECVTX B-tagging algorithm (See Section 4.3)

N_W and (1 - F_{QCD}) are calculated separately for each jet bin, as a function of lepton type. F_{WHF} and ϵ_{tag} are calculated separately for each jet bin, across all leptons. The resulting final answer in each jet bin is the sum of the electron and muon components. The number of pre-tag data events (N_W) is the same for each of

these three backgrounds. These numbers are shown in Table 7.4. For the $Wb\bar{b}$ and $Wc\bar{c}$ backgrounds there are two different F_{WHF} and ϵ_{tag} for each lepton : for the case when we only find 1 heavy flavor jet in the event, and for the case when we find both heavy flavor jets in the event.

	1 Jet	2 Jet	3 Jet	$\geq$3 Jet
CMUP muons	2809	458	60	19
CMX muons	1470	221	32	5
Muons total	4279	679	92	24
CEM electrons	5865	935	157	52

Table 7.4: Pre-tag data events (N_W) for electrons and muons, as a function of jet bin. These numbers are used for each of the three W+heavy flavor backgrounds.

The number of pre-tag candidate events which contain a real W boson, (1 - F_{QCD}), can be calculated using values for F_{QCD} found in Table 7.1. The heavy flavor fractions, F_{WHF}, are derived strictly from Monte Carlo samples. The heavy flavor fraction is found using both a W+heavy flavor Monte Carlo (W$b\bar{b}$, W$c\bar{c}$, or Wc) and W+light flavor Monte Carlo sample :

$$F_{WHF} = \frac{\sigma_{W+HF}}{\sigma_{W+jets\ inclusive}} \cdot \frac{\epsilon^{b,cjet}_{W+HF}}{\epsilon_{W+jets\ inclusive}} \tag{7.10}$$

σ is the calculated theoretical cross section of the W+heavy flavor and W+jets inclusive Monte Carlo samples. To measure the heavy flavor fraction it is necessary to find the heavy flavor jets in the Monte Carlo samples. $\epsilon^{b,cjet}$ is the efficiency to match a bottom (charm) quark to a tight jet in a cone of $\triangle R < 0.4$, for all pre-tag candidate events in the Monte Carlo samples.

The F_{WHF} and tagging efficiency are the same for all lepton types in each jet bin, internal to each background. The particular treatment for each background is described in the following sections.

7.2.2 Calculation of Background Contributions

We calculate the expected contribution from each of the three W+heavy flavor backgrounds using Equation 7.9. The error propagation requires careful bookkeeping, and is included here for completeness. The discussion of results from the W+heavy flavor backgrounds is continued in Section 7.2.3.

Equation 7.9 is of the form Y = A · B. If A and B are not correlated, we have the following :

$$\text{in general, if } Y = A \cdot B \tag{7.11}$$

$$\sigma_Y^2 = (\frac{\partial Y}{\partial A})^2 \cdot \sigma_A^2 + (\frac{\partial Y}{\partial B})^2 \cdot \sigma_B^2 \tag{7.12}$$

$$= (B^2 \cdot \sigma_A^2) + (A^2 \cdot \sigma_B^2) \tag{7.13}$$

$$= Y^2 \cdot [(\frac{\sigma_A}{A})^2 + (\frac{\sigma_B}{B})^2] \tag{7.14}$$

$$\begin{aligned} N_{WHF\ total} &= \underbrace{(N_{W_{ele}} \cdot (1 - F_{QCD_{ele}}) + N_{W_{muo}} \cdot (1 - F_{QCD_{muo}}))} \cdot \underbrace{F_{WHF} \cdot \epsilon_{tag}} \\ &= A \cdot B \\ \sigma^2_{N_{WHF\ total}} &= N^2_{WHF\ total} \cdot [(\frac{\sigma_A}{A})^2 + (\frac{\sigma_B}{B})^2] \end{aligned} \tag{7.15}$$

where ϵ_{tag} has already been multiplied by the scale factor (SF). Examining the "A" and "B" pieces separately, we find :

$$
\begin{aligned}
A &= [\underbrace{N_{W_{ele}}} \cdot \underbrace{(1 - F_{QCD_{ele}})}] + [\underbrace{N_{W_{muo}}} \cdot \underbrace{(1 - F_{QCD_{muo}})}] \\
&= (c \cdot d) + (e \cdot f) \\
\sigma_A^2 &= \sigma_{c \cdot d}^2 + \sigma_{e \cdot f}^2 \\
where\ \sigma_{c \cdot d, e \cdot f}^2 &= [N_W \cdot (1 - F_{QCD})]^2 \cdot [(\frac{\sigma_{N_W}}{N_W})^2 + (\frac{\sigma_{F_{QCD}}}{1 - F_{QCD}})^2]
\end{aligned}
\tag{7.16}
$$

$$
\begin{aligned}
B &= F_{WHF} \cdot \epsilon_{tag} \\
\sigma_B^2 &= (F_{WHF} \cdot \epsilon_{tag})^2 \cdot [(\frac{\sigma_{F_{WHF}}}{F_{WHF}})^2 + (\frac{\sigma_{\epsilon_{tag}}}{\epsilon_{tag}})^2]
\end{aligned}
\tag{7.17}
$$

In the $Wb\bar{b}$ and $Wc\bar{c}$ backgrounds, where you can tag either one or both of the heavy flavor jets in an event, part "A" of Equation 7.15 remains the same, while part "B" has an additional piece added. Here "_1" is for events which tag one heavy flavor jet, "_2" is for events which tag both :

$$
\begin{aligned}
B &= [\underbrace{F_{WHF_1}} \cdot \underbrace{\epsilon_{tag_1}}] + [\underbrace{F_{WHF_2}} \cdot \underbrace{\epsilon_{tag_2}}] \\
&= (g \cdot h) + (i \cdot j) \\
\sigma_B^2 &= \sigma_{g \cdot h}^2 + \sigma_{i \cdot j}^2 \\
where\ \sigma_{g \cdot h, i \cdot j}^2 &= (F_{WHF} \cdot \epsilon_{tag})^2 \cdot [(\frac{\sigma_{F_{WHF}}}{F_{WHF}})^2 + (\frac{\sigma_{\epsilon_{tag}}}{\epsilon_{tag}})^2]
\end{aligned}
\tag{7.18}
$$

7.2.3 $Wb\bar{b}$

$Wb\bar{b}$ events arise from QCD processes in real W events, where gluon splitting produces a heavy flavor quark anti-quark pair. (See Figure 7.2) The presence of additional gluons can promote this process into our W+3 and W+4 jet bins. Therefore, three $Wb\bar{b}$ Monte Carlo samples were used to calculate this background : $Wb\bar{b}$

plus 0, 1 and 2 additional partons in the event. [59] The denominator for the heavy flavor fraction uses Monte Carlo samples for both W+light flavor and W+heavy flavor (W+jets inclusive). The heavy flavor fractions used in calculating this background are the same as those used in the Run I analysis. [59] The tagging efficiency is measured directly in the Run II $Wb\bar{b}$ Monte Carlo sample.

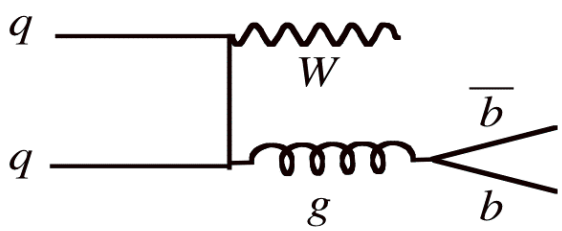

Figure 7.2: Production of W+heavy flavor backgrounds via gluon splitting in real W events

The $Wb\bar{b}$ heavy flavor fraction and tagging efficiencies are shown in Table 7.5. These numbers are separated based on the number of heavy flavor jets found in the event (1 or 2), per jet bin. The tagging efficiency shown in Table 7.5 has the scale factor (SF) of 0.86 already included.

The last row in Table 7.5 shows the final result for part B of Equation 7.9, with errors. Table 7.6 presents results from part A, as well as the final expected background contribution from $Wb\bar{b}$ events, as a function of jet bin.

	1 Jet	2 Jet	3 Jet	≥3 Jet
$F_{Wb\bar{b}}$ (1 B)	0.0058±0.0020	0.0092±0.0032	0.0135±0.0050	0.026±0.011
ϵ_{tag} (1 B)	0.281±0.023	0.292±0.025	0.308±0.029	0.292±0.041
part B (1 B)	0.0016 ± 0.0006	0.0027 ± 0.0010	0.0042 ± 0.0016	0.0076 ± 0.0034
$F_{Wb\bar{b}}$ (2 B)	0	0.0085±0.0025	0.014 ± 0.0004	0.017±0.005
ϵ_{tag} (2 B)	0	0.505±0.043	0.532±0.050	0.523±0.058
part B (2 B)	0	0.0043 ± 0.0013	0.0074 ± 0.0022	0.0089 ± 0.0028
total B	0.0016 ± 0.0006	0.0070 ± 0.0016	0.0116 ± 0.0027	0.0165 ± 0.0044

Table 7.5: Heavy flavor fraction and tagging efficiency for W$b\bar{b}$ events, as a function of jet bin. Please note the tagging efficiency shown here has the scale factor of 0.86 included. (part B = $F_{WHF} \cdot \epsilon_{tag}$)

	1 Jet	2 Jet	3 Jet	≥3 Jet
A_{ele}	5073 ± 404.3	766.70 ± 87.81	125.60 ± 18.63	41.60 ± 7.77
A_{muo}	4108 ± 106.1	645 ± 28.23	82.80 ± 9.78	21.60 ± 4.57
part A	9181 ± 418	1412 ± 92.23	208.4 ± 21.04	63.2 ± 9.01
total B	0.0016 ± 0.0006	0.0070 ± 0.0016	0.0116 ± 0.0027	0.0165 ± 0.0044
$N_{Wb\bar{b}}$ Total	14.96 ± 5.35	9.85 ± 2.39	2.42 ± 0.62	1.04 ± 0.32

Table 7.6: Results for the $Wb\bar{b}$ background, from part A of Equation 7.9. These results are presented separately for electron and muon events, as a function of jet bin. The last row in this table is the final expected background contribution from $Wb\bar{b}$ events. (part A = $N_W \cdot (1 - F_{QCD})$)

7.2.4 $Wc\bar{c}$

As with the $Wb\bar{b}$ events, $Wc\bar{c}$ events occur with gluon splitting in real W events. We also use $Wc\bar{c}$ plus 0, 1, and 2 additional partons to calculate this background contribution, in a fashion similar to $Wb\bar{b}$. The heavy flavor fractions used in calculating this background are the same as those used in the Run I analysis. [59] The tagging efficiency is measured directly in the Run II $Wc\bar{c}$ Monte Carlo sample.

The $Wc\bar{c}$ heavy flavor fraction and tagging efficiencies are shown in Table 7.7. These numbers are separated based on the number of heavy flavor jets found in the event (1 or 2), per jet bin. The tagging efficiency shown in Table 7.7 has the scale factor of 0.86 already included.

The last row in Table 7.7 shows the final result for part B of Equation 7.9, with errors. Table 7.8 presents results from part A, as well as the final expected background contribution from $Wc\bar{c}$ events, as a function of jet bin.

7.2.5 Wc

Wc backgrounds come from the flavor excitation process, $sg \rightarrow Wc, dg \rightarrow Wc$. The heavy flavor fractions used in calculating this background are the same as those used in the Run I analysis. The tagging efficiency has been measured using Run II ALPGEN Monte Carlo samples.

	1 Jet	2 Jet	3 Jet	≥3 Jet
$F_{Wc\bar{c}}$ (1 C)	0.0128±0.005	0.024±0.010	0.034±0.014	0.039±0.019
ϵ_{tag} (1 C)	0.065±0.011	0.070±0.012	0.064±0.012	0.080±0.021
part B (1 C)	0.0008 ± 0.0004	0.0017 ± 0.0008	0.0022 ± 0.0010	0.0031 ± 0.0017
$F_{Wc\bar{c}}$ (2 C)	0	0.0104±0.0027	0.017±0.0050	0.022±0.0060
ϵ_{tag} (2 C)	0	0.129±0.022	0.122±0.023	0.110±0.027
part B (2 C)	0	0.0013 ± 0.0004	0.0021 ± 0.0007	0.0024 ± 0.0009
total B	0.0008 ± 0.0004	0.0030 ± 0.0009	0.0043 ± 0.0012	0.0055 ± 0.0019

Table 7.7: Heavy flavor fraction and tagging efficiency for $Wc\bar{c}$ events, as a function of jet bin. Please note the tagging efficiency shown here has the scale factor of 0.86 included.

	1 Jet	2 Jet	3 Jet	≥3 Jet
A_{ele}	5073 ± 404.3	766.70 ± 87.81	125.60 ± 18.63	41.60 ± 7.77
A_{muo}	4108 ± 106.1	645 ± 28.23	82.80 ± 9.78	21.60 ± 4.57
part A	9181 ± 418	1412 ± 92.23	208.4 ± 21.04	63.2 ± 9.01
total B	0.0008 ± 0.0004	0.0030 ± 0.0009	0.0043 ± 0.0012	0.0055 ± 0.0019
$N_{Wc\bar{c}}$ Total	7.64 ± 3.27	4.27 ± 1.25	0.89 ± 0.27	0.35 ± 0.13

Table 7.8: Results for the $Wc\bar{c}$ background, from part A of Equation 7.9. These results are presented separately for electron and muon events, as a function of jet bin. The last row in this table is the final expected background contribution from $Wc\bar{c}$ events.

The Wc heavy flavor fraction and tagging efficiencies are shown in Table 7.9. The tagging efficiency shown in Table 7.9 has the scale factor of 0.86 already included.

The last row in Table 7.9 shows the final result for part B of Equation 7.9, with errors. Table 7.10 presents results from part A, as well as the final expected background contribution from Wc events, as a function of jet bin.

	1 Jet	2 Jet	3 Jet	≥3 Jet
F_{Wc}	0.048±0.013	0.072±0.022	0.75±0.23	0.75±0.23
ϵ_{tag}	0.061±0.010	0.065±0.011	0.064±0.013	0.064±0.013
part B	0.0029 ± 0.0009	0.0047 ± 0.0016	0.0048 ± 0.0018	0.0048 ± 0.0018

Table 7.9: Heavy flavor fraction and tagging efficiency, for Wc events, as a function of jet bin. Please note the tagging efficiency shown here has the scale factor of 0.86 included.

7.2.6 Corrections due to Pre-Tag $t\bar{t}$ Events

The W+heavy flavor backgrounds are normalized to *all* pre-tag candidate events found in data, which contain a real W boson. These pre-tag events are a mixture of

	1 Jet	2 Jet	3 Jet	≥3 Jet
A_{ele}	5073 ± 404.3	766.70 ± 87.81	125.60 ± 18.63	41.60 ± 7.77
A_{muo}	4108 ± 106.1	645 ± 28.23	82.80 ± 9.78	21.60 ± 4.57
part A	9181 ± 418	1412 ± 92.23	208.4 ± 21.04	63.2 ± 9.01
part B	0.0029 ± 0.0009	0.0047 ± 0.0016	0.0048 ± 0.0018	0.0048 ± 0.0018
N_{Wc} Total	26.88 ± 8.60	6.61 ± 2.35	1.00 ± 0.38	0.30 ± 0.12

Table 7.10: Results for the Wc background, from part A of Equation 7.9. These results are presented separately for electron and muon events, as a function of jet bin. The last row in this table is the final expected background contribution from Wc events.

background events and $t\bar{t}$ signal events. We really want to normalize the W+heavy flavor backgrounds to the number of non-top pre-tag events, excluding the WW, WZ, and single top backgrounds. The correction from WW, WZ, and single top is less than 1%, and is not included here. The heavy flavor backgrounds are corrected for the $t\bar{t}$ present in the pre-tag sample through an iterative process. The iteration is as follows : [61]

- 1. Start with the number of observed tagged events in data. From this subtract the total expected *uncorrected* background sum (the first time through). The resulting value is your number of tagged $t\bar{t}$ events.

$$N_{tag\ t\bar{t}} = N_{tag\ total} - N_{total\ expected\ WHF\ bgd} - N_{total\ expected\ other\ bgd} \tag{7.19}$$

- 2. Divide the number of tagged $t\bar{t}$ events by the per-event tagging efficiency for $t\bar{t}$ events (0.55, See Table 6.8). This will give you the number of pre-tag $t\bar{t}$ events expected.

$$N_{pre-tag\ t\bar{t}\ events} = \frac{N_{tag\ t\bar{t}}}{\epsilon_{tag}} \tag{7.20}$$

- 3. Subtract this number from the *total* number of pre-tag W events (i.e. $N_W \cdot$

$(1 - F_{QCD}))$. The result is the number of pre-tag W candidate events which do not contain $t\bar{t}$.

$$N_{pre-tag\ W\ no\ t\bar{t}} = N_{pre-tag\ W} - N_{pre-tag\ t\bar{t}\ events} \tag{7.21}$$

- 4. Multiply this number by the sum of the product of the heavy flavor fraction and tagging efficiency, for all three W+heavy flavor backgrounds (ϵ_{total}). This gives you the new number of total W+heavy flavor backgrounds expected. This new number will now be used in step 1 when subtracting the backgrounds from observed tags.

$$\epsilon_{total} = (F_{Wc} \cdot \epsilon_{tag\ Wc}) \tag{7.22}$$

$$+ \{(F_{Wb\bar{b}_1B} \cdot \epsilon_{tag\ Wb\bar{b}_1B}) + (F_{Wb\bar{b}_2B} \cdot \epsilon_{tag\ Wb\bar{b}_2B})\} \tag{7.23}$$

$$+ \{(F_{Wc\bar{c}_1C} \cdot \epsilon_{tag\ Wc\bar{c}_1C}) + (F_{Wc\bar{c}_2C} \cdot \epsilon_{tag\ Wc\bar{c}_2C})\} \tag{7.24}$$

$$N_{total\ expected\ WHF\ bgd} = N_{pre-tag\ W\ no\ t\bar{t}} \cdot \epsilon_{total} \tag{7.25}$$

- 5. Repeat this process until the change in the number of pre-tagged $t\bar{t}$ events is less than 1%.

$$\text{require} : \frac{N_{pre-tag\ t\bar{t}\ events(i+1)} - N_{pre-tag\ t\bar{t}\ events(i)}}{N_{pre-tag\ t\bar{t}\ events(i+1)}} < 0.01 \tag{7.26}$$

- 6. This will give you your final W+heavy flavor background. The change to the individual backgrounds is found by multiplying each uncorrected background

(Tables 7.6, 7.8, 7.10) by the ratio of the new corrected W+HF sum and the original uncorrected W+HF sum.

$$N_{corrected\ Wc} = N_{uncorrected\ Wc} \cdot \frac{N_{corrected\ total\ expected\ WHF\ bgd}}{N_{uncorrected\ total\ expected\ WHF\ bgd}} \tag{7.27}$$

- 7. The error on the new W+heavy flavor background is found by assuming that the fractional error, that is the error on the background divided by the background, remains constant :

$$\frac{\sigma_{Wc}}{Wc} = \frac{\sigma_{Wc\ corrected}}{Wc\ corrected} \tag{7.28}$$

7.2.7 Results

Results for all three W+heavy flavor backgrounds are shown in Table 7.11, before and after correction. The correction has a larger effect as we increase the jet bin, due to an increase in $t\bar{t}$ content. (See Figure 3.1)

	1 Jet	2 Jet	3 Jet	$\geq$3 Jet
$N_{Wb\bar{b}}$	14.96 ± 5.35	9.85 ± 2.39	2.42 ± 0.62	1.04 ± 0.32
Corrected	14.94 ± 5.34	9.81 ± 2.38	2.40 ± 0.62	0.56 ± 0.17
$N_{Wc\bar{c}}$	7.64 ± 3.27	4.27 ± 1.25	0.89 ± 0.27	0.35 ± 0.13
Corrected	7.62 ± 3.26	4.25 ± 1.25	0.88 ± 0.27	0.19 ± 0.07
N_{Wc}	26.88 ± 8.60	6.61 ± 2.35	1.00 ± 0.38	0.30 ± 0.12
Corrected	26.83 ± 8.58	6.58 ± 2.34	0.99 ± 0.38	0.16 ± 0.07
$\sum_{old}$	49.48	20.73	4.31	1.69
$\sum_{corr}$	49.39	20.64	4.27	0.91

Table 7.11: Final results for the W+heavy flavor backgrounds, after corrections for $t\bar{t}$, as a function of jet bin.

7.3 Electroweak Backgrounds

There are five backgrounds to the $t\bar{t}$ production cross section measurement which are due to electroweak processes. These are the diboson, Z$\rightarrow$ $\tau\tau$, and single top

backgrounds. There are three flavors of diboson backgrounds : WW, WZ, and ZZ.

As stated in the previous section, the cross section calculations for electroweak processes are much more precise and trustworthy than those from QCD processes. This allows us to calculate the expected contributions from each of these backgrounds in a straightforward fashion, normalizing the luminosity of our data sample to the theoretical cross section of a given process.

We use the following equation to measure the expected contribution for each of these background sources :

$$N_{bgd} = \sigma \cdot BR \cdot SF \cdot (\sum_{lepton} \int L \cdot \epsilon_{accep} \cdot \epsilon_{tag}) \tag{7.29}$$

where the cross section is the NLO theoretical cross section. The branching ratio is the fraction of the time that one boson decays into a lepton neutrino pair and the other boson decays into a quark anti-quark pair. The scale factor is required when using a tagging efficiency, as described in Chapter IV. The second half of this equation is the sum over all three lepton types (central electrons, CMUP muons and CMX muons) of the product of the luminosity of the data sample, the acceptance, and the tagging efficiency for that lepton. The acceptance and tagging efficiency are measured in Monte Carlo samples for each of these backgrounds, for each type of lepton.

The acceptance is the number of events passing the kinematic cuts and falling within the proper geometry of the detector (ϵ_{evtsel}), multiplied by the lepton ID cut efficiency and the lepton trigger efficiency. The denominator for the acceptance is the number of events passing the OBSV cut only (See Section 6.2) :

$$\epsilon_{accep} = \frac{\#\ events\ passing\ kin\ cuts}{\#\ events\ passing\ OBSV\ cut} \cdot \epsilon_{leptonID} \cdot \epsilon_{trigger} \tag{7.30}$$

The tagging efficiency is per-event, and is the number of events with a tagged jet divided by the number passing the kinematic cuts and located in the central portion of the detector:

$$\epsilon_{tag} = \frac{\#\ events\ with \geq 1\ tagged\ jet}{\#\ events\ passing\ kin\ cuts} \tag{7.31}$$

The error propagation for both the tagging efficiency and the acceptance is binomial, because the numbers in the numerator are a subset of those found in the denominator :

$$\sigma^2_{\epsilon_{tag}} = \frac{\epsilon_{tag} \cdot (1 - \epsilon_{tag})}{\#\ events\ passing\ kin\ cuts} \tag{7.32}$$

$$\begin{aligned} \sigma_{\epsilon_{accep}} &= \epsilon_{accep} \cdot \{(\frac{\sigma_{\epsilon_{evtsel}}}{\epsilon_{evtsel}})^2 + (\frac{\sigma_{\epsilon_{leptonID}}}{\epsilon_{leptonID}})^2 + (\frac{\sigma_{\epsilon_{trigger}}}{\epsilon_{trigger}})^2\} \\ \text{where } \sigma^2_{\epsilon_{evtsel}} &= \frac{\epsilon_{evtsel} \cdot (1 - \epsilon_{evtsel})}{\#\ events\ passing\ OBSV\ cut} \end{aligned} \tag{7.33}$$

7.3.1 WW

In the WW background one W decays into a lepton-neutrino pair and the other W decays into a $c\overline{s}$ quark anti-quark pair. In the generation of the WW Monte Carlo sample one of the W bosons was forced to decay into a lepton neutrino pair. The output from this Monte Carlo does not have an even mix of true WW event decays

as found in nature. This means that the theoretical cross section for all WW decays, 13.25 ± 0.25, is not applicable to this sample. We solve this problem by multiplying the theoretical cross section by the branching ratio for one W to decay into any lepton neutrino pair. This value is 3 times the branching ratio for a W to decay into one of the lepton neutrino pairs. Theoretically this number is 1/9. We use the measured world average branching ratio of 0.1068. [64] Values used in Equation 7.29 for calculation of the WW expected background contribution are shown in Table 7.12, along with the final expected background, per jet bin.

	1 Jet	2 Jet	3 Jet	≥3 Jet
	Theoretical Cross Section 13.25 ± 0.25 pb			
	Branching Ratio $3 \cdot 0.1068$			
	ϵ_{tag}			
CEM	0.0175 ± 0.0007	0.0374 ± 0.0011	0.0494 ± 0.0026	0.0652 ± 0.0079
CMUP	0.0166 ± 0.0009	0.0357 ± 0.0014	0.0413 ± 0.0032	0.0531 ± 0.0096
CMX	0.0192 ± 0.0014	0.0392 ± 0.0022	0.0393 ± 0.0046	0.0643 ± 0.016
	ϵ_{accep}			
CEM	0.0395 ± 0.0009	0.0347 ± 0.0008	0.0074 ± 0.0002	0.0011 ± 0.00004
CMUP	0.0200 ± 0.0007	0.0172 ± 0.0006	0.0037 ± 0.0001	0.0005 ± 0.00003
CMX	0.0093 ± 0.0004	0.0078 ± 0.0003	0.0018 ± 0.00009	0.0003 ± 0.00002
	$\int L$			
CEM	107.9 pb^{-1}			
CMUP	107.9 pb^{-1}			
CMX	98.0 pb^{-1}			
	$\int L \cdot \epsilon_{accep} \cdot \epsilon_{tag}$			
CEM	0.0744 ± 0.0029	0.1400 ± 0.0040	0.0393 ± 0.0021	0.0076 ± 0.0009
CMUP	0.0358 ± 0.0019	0.0665 ± 0.0026	0.0163 ± 0.0013	0.0029 ± 0.0005
CMX	0.0174 ± 0.0013	0.0301 ± 0.0017	0.0070 ± 0.0008	0.0016 ± 0.0004
	$\sum_{lepton}$			
	0.1277 ± 0.0037	0.2366 ± 0.0050	0.0626 ± 0.0026	0.0121 ± 0.0011
	Final WW result			
	0.44 ± 0.06	0.81 ± 0.12	0.22 ± 0.03	0.04 ± 0.01

Table 7.12: Components used in the calculation of the WW background, as a function of jet bin and lepton type. Final estimates for the WW background contribution are shown in the last row.

7.3.2 WZ

In the WZ background the W boson decays into a lepton-neutrino pair while the Z decays into a heavy flavor ($b\bar{b}, c\bar{c}$) quark pair. The WZ Monte Carlo did not place any initial requirements on the decay of these bosons. The theoretical cross section for WZ production, 3.96±0.06 pb, is used in place of the quantity "$\sigma \cdot BR$" in Equation 7.29. Values used in Equation 7.29 for calculation of the WZ expected background contribution are shown in Table 7.13, along with the final expected background, per jet bin.

	1 Jet	2 Jet	3 Jet	≥3 Jet
	$\sigma \cdot BR$			
	3.96±0.06 pb			
	ϵ_{tag}			
CEM	0.0686 ± 0.0068	0.1096 ± 0.0078	0.1142 ± 0.0154	0.1017 ± 0.0394
CMUP	0.0557 ± 0.0077	0.1197 ± 0.0102	0.1143 ± 0.0203	0.0769 ± 0.0427
CMX	0.0633 ± 0.0120	0.1263 ± 0.0152	0.1226 ± 0.0319	0.0714 ± 0.0487
	ϵ_{accep}			
CEM	0.0091 ± 0.0003	0.0108 ± 0.0003	0.0029 ± 0.0002	0.0004 ± 0.00005
CMUP	0.0051 ± 0.0002	0.0058 ± 0.0003	0.0014 ± 0.0001	0.0002 ± 0.00003
CMX	0.0025 ± 0.0002	0.0029 ± 0.0002	0.0007 ± 0.00007	0.0002 ± 0.00003
	$\int L$			
CEM	107.9 pb^{-1}			
CMUP	107.9 pb^{-1}			
CMX	98.0 pb^{-1}			
	$\int L \cdot \epsilon_{accep} \cdot \epsilon_{tag}$			
CEM	0.0675 ± 0.0067	0.1278 ± 0.0090	0.0352 ± 0.0047	0.0043 ± 0.0017
CMUP	0.0307 ± 0.0042	0.0749 ± 0.0064	0.0172 ± 0.0031	0.0018 ± 0.0010
CMX	0.0157 ± 0.0030	0.0361 ± 0.0044	0.0078 ± 0.0020	0.0012 ± 0.0008
	$\sum_{lepton}$			
	0.1138 ± 0.0085	0.2388 ± 0.0119	0.0602 ± 0.0060	0.0074 ± 0.0021
	Final WZ result			
	0.37 ± 0.06	0.77 ± 0.11	0.20 ± 0.03	0.02 ± 0.01

Table 7.13: Components used in the calculation of the WZ background, as a function of jet bin and lepton type. Final estimates for the WZ background contribution are shown in the last row.

7.3.3 ZZ

In ZZ background events one of the Z bosons will decay into a heavy flavor quark anti-quark pair, such as $b\overline{b}$, or $c\overline{c}$. The other Z will decay into either a lepton anti-lepton pair or a neutrino anti-neutrino pair. Generation of the ZZ Monte Carlo was also done with no restrictions placed on the decay of the bosons. "$\sigma \cdot BR$" from Equation 7.29 is the theoretical cross section for ZZ decays, or 1.58±0.02 pb. Values used in Equation 7.29 for calculation of the ZZ expected background contribution are shown in Table 7.14, along with the final expected background, per jet bin. The ZZ background is negligible but is shown here for completeness.

	1 Jet	2 Jet	3 Jet	≥3 Jet
	$\sigma \cdot BR$			
	1.58±0.02 pb			
	ϵ_{tag}			
CEM	0.0608 ± 0.0163	0.1280 ± 0.0211	0.0949 ± 0.0250	0.0790 ± 0.0437
CMUP	0.0843 ± 0.0153	0.1067 ± 0.0146	0.0725 ± 0.0221	0.1667 ± 0.0761
CMX	0.0769 ± 0.0213	0.0960 ± 0.0209	0.2051 ± 0.0457	0.0833 ± 0.0780
	ϵ_{accep}			
CEM	0.0010 ± 0.00007	0.0012 ± 0.00008	0.0006 ± 0.00006	0.0002 ±0.00003
CMUP	0.0013 ± 0.00009	0.0018 ± 0.0001	0.0006 ± 0.00005	0.0001 ± 0.00002
CMX	0.0007 ± 0.00006	0.0009 ± 0.00007	0.0003 ± 0.00004	0.00005 ± 0.00002
	$\int L$			
CEM	107.9 pb^{-1}			
CMUP	107.9 pb^{-1}			
CMX	98.0 pb^{-1}			
	$\int L \cdot \epsilon_{accep} \cdot \epsilon_{tag}$			
CEM	0.0065 ± 0.0018	0.0160 ± 0.0026	0.0065 ± 0.0017	0.0015 ± 0.0008
CMUP	0.0120 ± 0.0022	0.0206 ± 0.0028	0.0043 ± 0.0013	0.0017 ± 0.0008
CMX	0.0050 ± 0.0014	0.0078 ± 0.0017	0.0067 ± 0.0015	0.0004 ± 0.0004
	$\sum_{lepton}$			
	0.0235 ± 0.0031	0.0446 ± 0.0042	0.0175 ± 0.0026	0.0036 ± 0.0012
	Final ZZ result			
	0.03 ± 0.01	0.06 ± 0.01	0.02 ± 0.004	0.01 ± 0.002

Table 7.14: Components used in the calculation of the ZZ background, as a function of jet bin and lepton type. Final estimates for the ZZ background contribution are shown in the last row.

7.3.4 $Z \to \tau\tau$

Z$\to$ $\tau\tau$ events mimic $t\bar{t}$ events when one of the τ decays into a lepton and the other τ decay produces a tagged jet. The leptonic decay of the τ, $\tau \to \nu_\tau l \nu_l$, is called a one prong decay. This means that there is one charged particle in the final state. The tagged jet is produced by a three prong decay, for instance $\tau \to \pi^-\pi^+\pi^-\nu_\tau$, which provides three charged particles in the final state. The longer lifetime of the tau (10^{-13} seconds) allows the τ to travel before decaying, the result of which is a displaced vertex containing three charged tracks. If Z$\to$ $\tau\tau$ events are produced in association with other jets, it could contribute to the tagging rate in our W+jets selection. Figure 7.3 illustrates the Feynman diagram for a three prong Z$\to$ $\tau\tau$ decay.

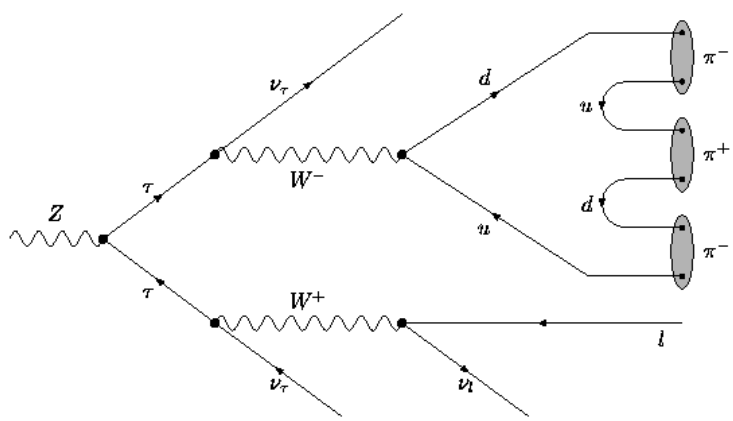

Figure 7.3: Lepton + three prong decay of Z$\to$ $\tau\tau$

The theoretical cross section for $Z \to \tau\tau$ is 0.26$\pm$0.03 nb. The branching ratio for a $Z \to \tau\tau \to e\nu\nu$ + 3 prong decay is is 0.05. We assume that the tagging efficiency for three prong events is similar to that from charm, so we use the SECVTX scale factor for B-jets and double the error (0.86$\pm$0.14). Values used in the calculation for this background are shown in Table 7.15, as a function of jet bin. Final results from this background are shown in the last row of Table 7.15.

	1 jet	2 jets	3 jets	≥4 jets
Cross Section	0.26±0.03 nb			
Branching Ratio	0.05			
Total Acceptance (%)	0.29±0.03	0.08±0.01	0.01±0.01	0.01±0.01
Tagging Efficiency (%)	11±2	11±2	11±2	11±2
Final Result	0.77 ± 0.13	0.21 ± 0.06	0.02 ± 0.02	0.006 ± 0.006

Table 7.15: $Z \to \tau\tau$ background

7.3.5 Combined Results

We combine the results from the WW, WZ, ZZ, and $Z \to \tau\tau$ into one background estimate. These results are correlated between the electron and muon components. In the case of 100% correlation the correlation terms are equal to the sum of the product of the errors :

$$cov(x, y, z) = \sigma_x \cdot \sigma_y + \sigma_x \cdot \sigma_z + \sigma_y \cdot \sigma_z \tag{7.34}$$

The WW, WZ, ZZ, and Z→ $\tau\tau$ backgrounds are correlated with each other, due to normalizing to the integrated luminosity of the data sample, and the use of the same B-tagging scale factor. To combine the backgrounds from WW, WZ, ZZ, and Z→ $\tau\tau$ we use the following error propagation :

(7.35)

$$\begin{aligned}
\sigma_{\sum}^2 &= \sigma_{WW}^2 + \sigma_{WZ}^2 + \sigma_{ZZ}^2 + \sigma_{Z\tau\tau}^2 + 2 \cdot cov(WW, WZ, ZZ, Z\tau\tau) \\
&= \sigma_{WW}^2 + \sigma_{WZ}^2 + \sigma_{ZZ}^2 + \sigma_{Z\tau\tau}^2 \\
&+ 2 \cdot (\sigma_{WW} \cdot \sigma_{WZ} + \sigma_{WW} \cdot \sigma_{ZZ} + \sigma_{WW} \cdot \sigma_{Z\tau\tau} + \sigma_{WZ} \cdot \sigma_{ZZ} + \sigma_{WZ} \cdot \sigma_{Z\tau\tau} + \sigma_{ZZ} \cdot \sigma_{Z\tau\tau}) \\
&= (\sigma_{WW} + \sigma_{WZ} + \sigma_{ZZ} + \sigma_{Z\tau\tau})^2 \\
\therefore\ \sigma_{\sum} &= \sigma_{WW} + \sigma_{WZ} + \sigma_{ZZ} + \sigma_{Z\tau\tau}
\end{aligned}$$

Results from the combination of these four electroweak backgrounds are shown in Table 7.16.

	1 jet	2 jets	3 jets	≥4 jets
WW	0.44 ± 0.06	0.81 ± 0.12	0.22 ± 0.03	0.04 ± 0.01
WZ	0.37 ± 0.06	0.77 ± 0.11	0.20 ± 0.03	0.02 ± 0.01
ZZ	0.03 ± 0.01	0.06 ± 0.01	0.02 ± 0.004	0.01 ± 0.002
Z→ $\tau\tau$	0.77 ± 0.13	0.21 ± 0.06	0.02 ± 0.02	0.006 ± 0.006
Total	1.61 ± 0.26	1.85 ± 0.30	0.46 ± 0.08	0.08 ± 0.03

Table 7.16: Total expected contribution from WW, WZ, ZZ, and $Z \to \tau\tau$ backgrounds.

7.3.6 Single Top

In addition to the $t\bar{t}$ production which is the focus of this thesis, top quarks can also be produced singly, in association with a b quark. This process occurs via electroweak interactions. Single top quarks are produced via two such mechanisms at the Tevatron, through either the off-mass shell W production (s-channel), or through the W-gluon fusion (t-channel) process. (See Figure 7.4)

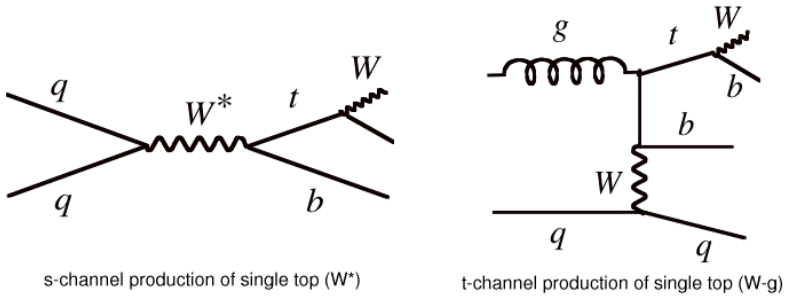

Figure 7.4: Two production mechanisms of single top at the Tevatron : off-shell W production (left) and W-gluon fusion (right).

We calculate the expected contribution from each of these production mechanisms separately, using 440K of s-channel and 500K of t-channel Monte Carlo samples. The theoretical cross section at the Tevatron for Run II for off-mass shell production is

	1 Jet	2 Jet	3 Jet	≥3 Jet
	$\sigma \cdot BR$			
	0.884 ± 0.004 pb			
	ϵ_{tag}			
CEM	0.374 ± 0.0079	0.5855 ± 0.0056	0.6059 ± 0.0105	0.6127 ± 0.0221
CMUP	0.385 ± 0.0106	0.5989 ± 0.0072	0.5878 ± 0.0138	0.5828 ± 0.0278
CMX	0.374 ± 0.0161	0.6184 ± 0.0115	0.5806 ± 0.0215	0.6250 ± 0.0442
	ϵ_{accep}			
CEM	0.0088 ± 0.0002	0.0183 ± 0.0004	0.0051 ± 0.0002	0.0012 ± 0.00006
CMUP	0.0043 ± 0.0002	0.0092 ± 0.0004	0.0026 ± 0.0001	0.0006 ± 0.00004
CMX	0.0020 ± 0.0001	0.0039 ± 0.0002	0.0011 ± 0.00007	0.0003 ± 0.00003
	$\int L$			
CEM	107.9 pb^{-1}			
CMUP	107.9 pb^{-1}			
CMX	98.0 pb^{-1}			
	$\int L \cdot \epsilon_{accep} \cdot \epsilon_{tag}$			
CEM	0.3540 ± 0.0075	1.157 ± 0.0111	0.3354 ± 0.0058	0.0762 ± 0.0027
CMUP	0.1778 ± 0.0049	0.597 ± 0.0072	0.1635 ± 0.0038	0.0399 ± 0.0019
CMX	0.0720 ± 0.0031	0.236 ± 0.0044	0.0654 ± 0.0024	0.0160 ± 0.0011
	$\sum_{lepton}$			
	0.6039 ± 0.0095	1.9910 ± 0.0139	0.5642 ± 0.0074	0.1321 ± 0.0035
	Final S-Channel Single Top result			
	0.43 ± 0.06	1.43 ± 0.20	0.41 ± 0.06	0.10 ± 0.01

Table 7.17: Final results for the S-Channel Single Top backgrounds, as a function of jet bin.

0.884 ± 0.004 (stat) ± 0.050 (NLO) pb, and 1.980 ± 0.004 (stat) ± 0.113 (NLO) pb for W-gluon fusion. The "BR" factor in Equation 7.29 is set to 1 for these calculations. Results from the s-channel are shown in Table 7.17, from the t-channel in Table 7.18. The final result for the single top background expectation is a linear sum of the s and t-channel values, per jet bin. As in the diboson case, the t-channel and s-channel results are 100% correlated. Please refer to Equation 7.35 as an example of the error propagation. (See Table 7.19)

7.4 Mistags

A "mistag" occurs when the SECVTX tagging algorithm finds a secondary vertex in a jet that doesn't really have one. Mistags come from track mismeasurements and can cause a jet to be falsely tagged as positive or negative. We assume that the rate

	1 Jet	2 Jet	3 Jet	≥3 Jet
	$\sigma \cdot BR$			
	1.980 ± 0.004 pb			
	ϵ_{tag}			
CEM	0.3309 ± 0.0055	0.406 ± 0.0057	0.4606 ± 0.0132	0.4190 ± 0.0369
CMUP	0.3298 ± 0.0070	0.399 ± 0.0072	0.4241 ± 0.0176	0.4688 ± 0.0441
CMX	0.3372 ± 0.0114	0.383 ± 0.0118	0.4069 ± 0.0276	0.5172 ± 0.0928
	ϵ_{accep}			
CEM	0.0154 ± 0.0004	0.0156 ± 0.0004	0.0030 ± 0.0001	0.0004 ± 0.00003
CMUP	0.0080 ± 0.0003	0.0082 ± 0.0003	0.0014 ± 0.00007	0.0002 ± 0.00002
CMX	0.0033 ± 0.0002	0.0033 ± 0.0002	0.0006 ± 0.00004	0.00006 ± 0.00001
	$\int L$			
CEM	107.9 pb^{-1}			
CMUP	107.9 pb^{-1}			
CMX	98.0 pb^{-1}			
	$\int L \cdot \epsilon_{accep} \cdot \epsilon_{tag}$			
CEM	0.5513 ± 0.0091	0.6823 ± 0.0095	0.1472 ± 0.0042	0.0169 ± 0.0015
CMUP	0.2864 ± 0.0061	0.3546 ± 0.0064	0.0634 ± 0.0027	0.0115 ± 0.0011
CMX	0.1092 ± 0.0037	0.1230 ± 0.0038	0.0243 ± 0.0017	0.0028 ± 0.0005
	$\sum_{lepton}$			
	0.9470 ± 0.0116	1.1600 ± 0.0121	0.2358 ± 0.0053	0.0312 ± 0.0019
	Final T-Channel Single Top result			
	1.53 ± 0.21	1.88 ± 0.26	0.38 ± 0.05	0.05 ± 0.01

Table 7.18: Final results for the T-Channel Single Top backgrounds, as a function of jet bin.

1 Jet	2 Jet	3 Jet	≥3 Jet
S-Channel Single Top result			
0.43 ± 0.06	1.43 ± 0.20	0.41 ± 0.06	0.10 ± 0.01
T-Channel Single Top result			
1.53 ± 0.21	1.88 ± 0.26	0.38 ± 0.05	0.05 ± 0.01
Final Single Top			
1.96 ± 0.27	3.31 ± 0.46	0.79 ± 0.11	0.15 ± 0.02

Table 7.19: Final results for the Single Top background, as a function of jet bin.

to incorrectly tag a jet is the same for both negative and positive tags. The rate of negative tags is measured in a large inclusive jet sample. It is assumed that the rate of negative tags in the jet data is the same as the rate to fake a positive tag due to mistags in the W+jets sample.

The probability to tag a jet is measured in the jet data set, and is parameterized as a function of several kinematic variables of the jet: η, ϕ, jet E_T, track multiplicity of the jet, and total event E_T. This parameterization is the *mistag matrix*. [60] The matrix gives us the ability to predict the number of tags in any jet sample. Figure 7.5 compares the predicted positive and negative tag rates found using the mistag matrix to those observed in a high E_T jet sample. There is excellent agreement shown between the expected and observed rates, for both positive and negative tags.

To calculate the number of expected events from the background of incorrectly tagged jets we apply the mistag matrix to all taggable jets in our pre-tag candidate events. The per-jet result is summed on an event by event basis. The individual event mistag rates are then summed for all candidate events, separated by jet bin and lepton type. To avoid double counting with events already included in the QCD background estimate, we multiply each of the total event lepton results by the fraction (1 - F_{QCD}), to give the final mistag background estimate per lepton type. The final mistag rate is found by summing the muon and electron estimate. The double mistag rate is small so this sum gives us a good approximation of the event tag rate. Results from the mistag background are shown in Table 7.20.

7.5 Results

Final results for each background, separated by jet bin, are shown in Table 7.20. Numbers shown in the table for the W+heavy flavor backgrounds are *before* correc-

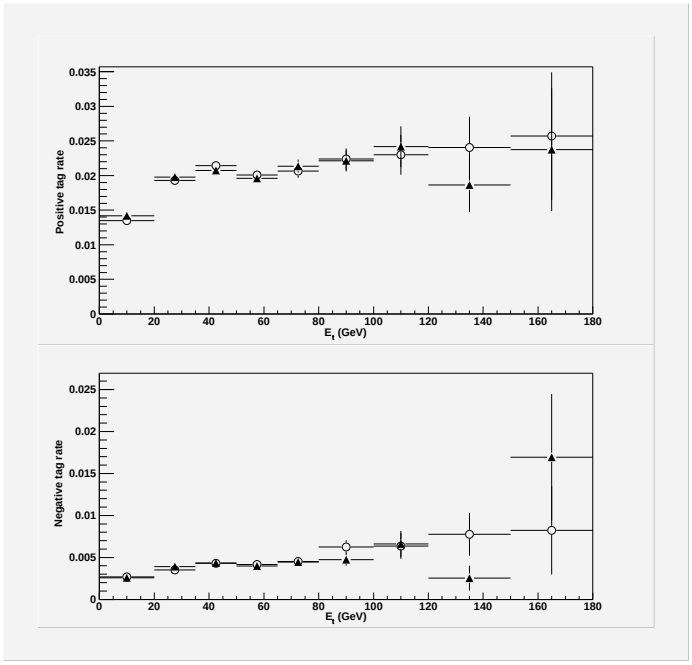

Figure 7.5: Positive and Negative Tags, expected (open circles) versus observed (filled circles), as a function of jet E_T. [60]

tions due to the $t\bar{t}$ contribution in the pre-tagged event sample. Final results before corrections are shown in the row labeled "Total". We find, in the ≥ 3 jet bin, 16.27 uncorrected background events and 15.45 corrected background events. Correlations exist between several of the backgrounds. We combine the errors in the following fashion :

$$\sigma^2_{total} = \sigma^2_{QCD} + (\sigma_{Wb\bar{b}} + \sigma_{Wc\bar{c}})^2 + (\sigma_{Wc} + \sigma_{WW/WZ/ZZ,Z\tau\tau} + \sigma_{single\ top})^2 + \sigma^2_{mistags} \quad (7.36)$$

Where the QED backgrounds (WW, WZ, ZZ, Z$\rightarrow \tau\tau$, and single top) and the Wc background are 100% correlated due to use of the tagging scale factor. The two W+heavy flavor backgrounds, $Wb\bar{b}$ and $Wc\bar{c}$, are correlated due to the production mechanism (gluon splitting) and the heavy flavor fraction measurement.

Table 7.21 lists all Monte Carlo samples used in calculation of the backgrounds.

Background	W + 1 jet	W + 2 jets	W + 3 jets	W + $\geq$ 4jets
Events before tagging	10078	1609	252	74
QCD	16.20 ± 2.03	7.96 ± 1.40	3.05 ± 0.59	1.54 ± 0.30
$Wb\bar{b}$	14.96 ± 5.35	9.85 ± 2.39	2.42 ± 0.62	1.04 ± 0.32
$Wc\bar{c}$	7.64 ± 3.27	4.27 ± 1.25	0.89 ± 0.27	0.35 ± 0.13
Wc	26.88 ± 8.60	6.61 ± 2.35	1.00 ± 0.38	0.30 ± 0.12
$WW/WZ/ZZ$, $Z \to \tau\tau$	1.61 ± 0.26	1.85 ± 0.30	0.46 ± 0.08	0.08 ± 0.03
single top	1.96 ± 0.27	3.31 ± 0.46	0.79 ± 0.11	0.15 ± 0.02
mistags	22.80 ± 3.30	9.20 ± 1.50	2.70 ± 0.40	1.50 ± 0.30
Total	92.05 ± 13.14	43.05 ± 5.21	11.31 ± 1.27	4.96 ± 0.64
Corrected Total	91.96 ± 13.11	42.96 ± 5.20	11.27 ± 1.27	4.18 ± 0.50
Observed positive tags	102	45	14	21

Table 7.20: The number of observed positive tagged events and the background summary for an integrated luminosity of 108 pb^{-1}. The corrected total refers to the background estimate after accounting for the $t\bar{t}$ contribution to the pre-tagged W+jets data sample.

Background	Generator	Samples
$Wb\bar{b}$	ALPGEN + HERWIG	WevBB+0p, 1p, 2p
$Wc\bar{c}$	ALPGEN + HERWIG	WevCC+0p, 1p, 2p
	ALPGEN + HERWIG	WmvCC+0p, 1p, 2p
Wc	ALPGEN + HERWIG	WevC+0p, 1p, 2p
W+light flavor	ALPGEN + HERWIG	Wev+1p, 2p, 3p, 4p
	ALPGEN + HERWIG	Wmv+1p, 2p, 3p, 4p
	ALPGEN + HERWIG	Wtv+1p, 2p, 3p, 4p
WW	ALPGEN + HERWIG	WW+0p, 1p, 2p
WZ	ALPGEN + HERWIG	WZ+0p, 1p, 2p
ZZ	ALPGEN + HERWIG	ZZ+0p
$Z \to \tau\tau$	ALPGEN + HERWIG	Z$\to \tau\tau$+1p, 2p
single top	PYTHIA	s, t channel

Table 7.21: Monte Carlo samples used for background calculations. The W+light flavor Monte Carlo samples are used in the calculation of the heavy flavor fraction.

CHAPTER VIII

Results

The top cross section is measured using :

$$\sigma_{t\bar{t}} = \frac{N_{obs} - N_{bgd}}{\epsilon_{t\bar{t}} \cdot \int Ldt} \tag{8.1}$$

Our final value for the denominator, including tagging efficiencies, is 4.47 ± 0.30 (stat) ± 0.49 (sys) pb^{-1} The number of observed events in data is 35 total (Table 5.1). The number of expected background events is 15.1 (Table 7.20). Putting this all together gives us a final result of :

$$\sigma_{t\bar{t}} = 4.5 \pm 1.4(stat) \pm 0.8(sys)\ pb \tag{8.2}$$

Figure 8.1 shows the distribution per jet bin of all backgrounds and observed data points, for events containing positively tagged jets. As shown in Figure 3.1, we expect the 1 and 2 jet bins to be dominated by events coming from background sources. In the ≥ 3 jet bin we expect to see an excess of events over those coming from background sources. This excess is attributed to $t\bar{t}$ events. [1]

It is instructive to compare our distribution of observed events to that expected from theory. Figure 8.2 shows the sum of all calculated backgrounds (blue line), and

[1] The error bars in Figures 8.1 and 8.2 are sometimes displayed incorrectly in ghostview. Please turn off the Antialias state to view these figures correctly

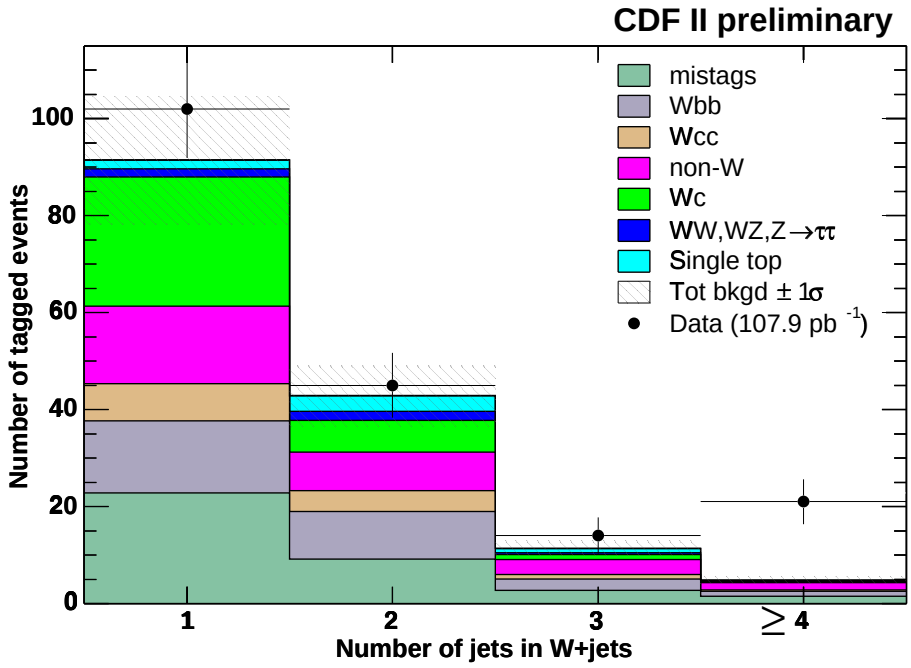

Figure 8.1: Positively tagged data events (points) with the expected contribution from our various background sources, per jet bin.

the sum of all backgrounds plus the expected distribution of $t\bar{t}$ events (red line), as calculated from Standard Model theory expectation of 6.7 pb. In the ≥ 4 jet bin we find the number of observed events falls exactly on the line of Standard Model theory and background expectations. In the 3 jet bin we find the number of expected events from our calculated backgrounds and Standard Model expectations from $t\bar{t}$ events to be 23.8 $\pm$ 2.8. We observe 14.0 $\pm$ 3.7 events. There is an observed fluctuation of 2 σ between these two numbers.

An overall view of the $t\bar{t}$ cross section measurements, both for Run I and Run II of the Tevatron, is shown in Figure 8.3. The results from Run I are combined across all three channels internal to each collider experiment. The red dot at $\sqrt{s}$ = 1.96 TeV is from the current lepton+jets B-tagged cross section measurement, from CDF. The upside down triangles are the current Run II dilepton cross section

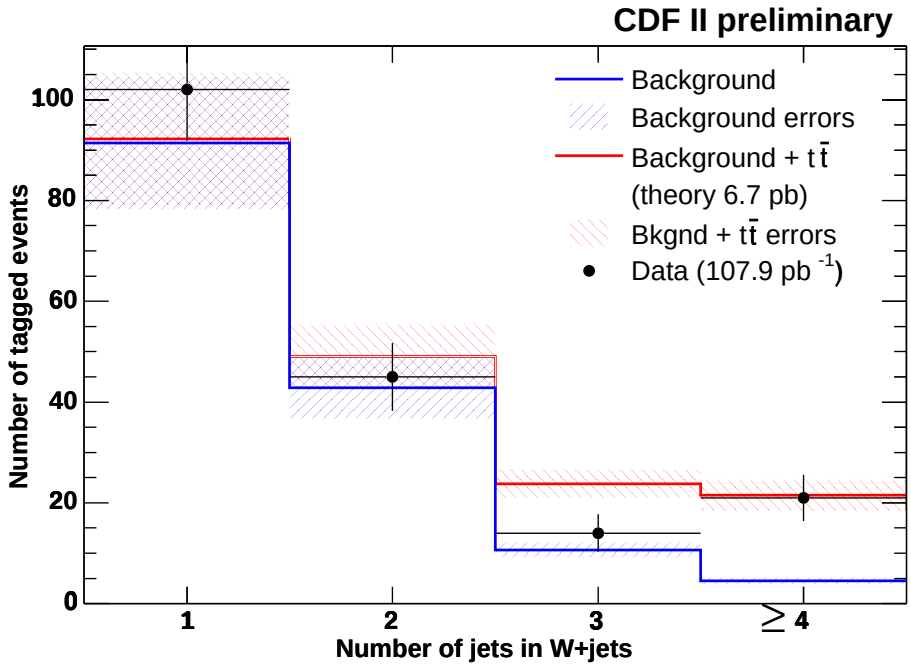

Figure 8.2: Positively tagged data events (points) with the expected contribution from our various background sources. The background sources are summed into the blue line. The red line is the expected distribution of $t\bar{t}$ events found using the Standard Model theory cross section of 6.7 pb.

measurements from CDF and D0. The dilepton channel offers a clean signature with very low statistics. This is evidenced by the large statistical error bars on the dilepton measurement points.

8.1 Cross Checks in Some Interesting Variables

8.1.1 Introduction

We use Monte Carlo samples to obtain shapes for each of our background contributions (with the exception of the QCD background), as well as the shape for the $t\bar{t}$ signal. We obtain shapes from each of the samples by applying the same analysis cuts used in data to define candidate events and filling histograms for various event and jet quantities. These shapes are normalized to the expectations shown in Table 7.20, and then added together. These model distributions are then compared to

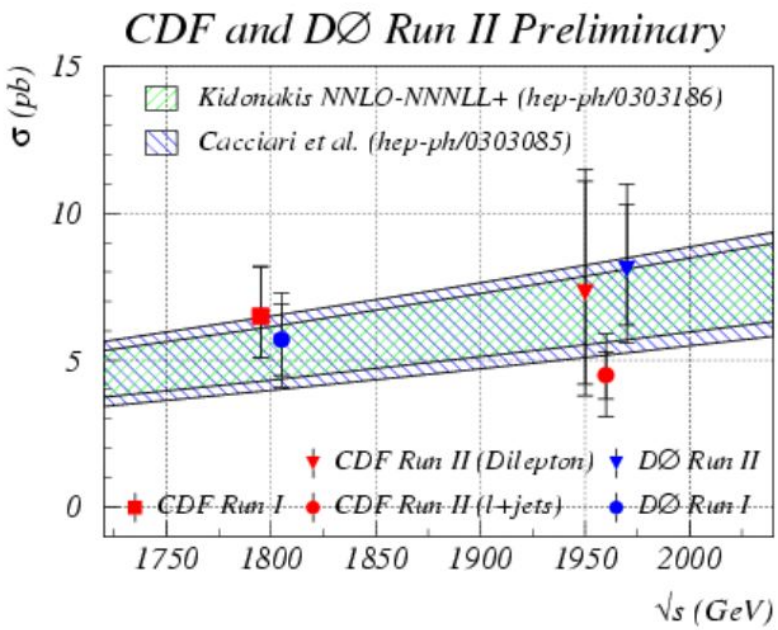

Figure 8.3: Comparisons between measured cross section results and theory predictions. Theory curves have been generated using $M_{top} = 175$ GeV. Shown are results from Run I of the Tevatron, operating under $\sqrt{s} = 1.8$ TeV, and the current results from Run II. Results from the CDF collaboration are shown in red, from D0 in blue. The circle point from Run II is from the B-tagged lepton+jets analysis, the subject of this thesis. Results from the dilepton channel cross section are marked with upside-down triangles. It is evident that the dilepton analyses are still very much statistics limited.

Background	W + 1 jet	W + 2 jets	W + 3 jets	W + $\geq$ 4jets
	Mistags (W+light flavor)			
	Wev1p Wmv1p Wtv1p	Wev2p Wmv2p Wtv2p	Wev3p Wmv3p Wtv3p	Wev4p Wmv4p Wtv4p
Wbb	WevBB0p	WevBB0p	WevBB1p	WevBB2p
	WCC			
	WevCC0p WmvCC0p	WevCC0p WmvCC0p	WevCC1p WmvCC1p	WevCC2p WmvCC2p
Wc	WevC0p	WevC1p	WevC2p	WevC2p
$WW/WZ/ZZ$, $Z \rightarrow \tau\tau$	WW0p	WW0p	WW1p	WW2p
single top	s channel			

Table 8.1: Monte Carlo samples used for background shapes.

those found in the data.

8.1.2 Method

All background and signal shapes except QCD are found using Monte Carlo samples. The naming convention for these is "something+Xp", where the "something" is the physics process - WW, Wc, etc, and the Xp is the number of additional partons allowed in the event. The breakdown of background Monte Carlo samples used for each jet bin is shown in Table 8.1.

We apply the following event selection cuts to the Monte Carlo samples for the signal and all background samples, *except QCD*, to obtain our starting set of pre-tag candidate events :

- OBSV cut (See Section 6.2)
- Cut on number of tight jets, after plug electron removal and jet energy corrections ($n_{jets} \geq$3)
- $\not\!\!E_T > 20$ GeV
- Dilepton Veto
- Z Veto

- Require a good isolated (isolation ≤ 0.1) electron not coming from conversions (or muon not from a cosmic ray)

We cannot rely on the Monte Carlo to model fakes from QCD. The QCD shapes must still be obtained from the non-isolated pre-tag data sample. To obtain our starting sample for the QCD shapes we apply the following cuts :

- Cut on number of tight jets, after corrections only. There is no plug electron removal done for these jets
- Dilepton Veto
- Z Veto
- Require a good non-isolated (isolation ≥ 0.2) electron or muon in the event
- $\not\!\!E_T \geq 20$
  - If it is an electron event, correct the $\not\!\!E_T$ in the standard fashion for good isolated muons
  - If it is a muon event, correct the $\not\!\!E_T$ for all good non-isolated muons in the event

To model variables in the mistag background we use W plus lepton neutrino Monte Carlo samples. We first remove all events containing $b\bar{b}$, $c\bar{c}$, or single charm, as these backgrounds are already accounted for in the W plus heavy flavor Monte Carlo samples. All other backgrounds shapes are obtained from Monte Carlo samples, without any additional manipulation.

The numbers of starting events in the Monte Carlo samples before any cuts are applied, the number of pre-tag candidate events, and the number of tagged events, are shown in Table 8.2 for the 1 and 2 jet bin, and Table 8.3 for the 3 and $\geq$4 jet bin.

Background	W + 1 jet			W + 2 jets		
	Total	Pre-Tag	Tag	Total	Pre-Tag	Tag
	Mistags (W+light flavor)					
Wev	67500	2475	–	189131	3599	–
Wmv	194931	5508	–	260000	3215	–
Wtv	291047	491	–	293736	313	–
$Wb\bar{b}$	233931	9371	2829	233931	2006	992
	WCC					
Wev	109941	3152	216	109941	602	86
Wmv	137487	2383	152	137487	469	61
Wc	293616	26278	1532	290046	10870	809
$WW/WZ/ZZ$, $Z \to \tau\tau$	220027	13839	232	220027	11894	424
single top	236000	3115	1189	236000	6660	3938

Table 8.2: Monte Carlo samples used for background shapes. Total refers to the total input Monte Carlo, before any cuts are made on the sample. Pre-Tag is the number of events left after all event selection cuts, with the exception of B-tagging, have been applied. Tag is the number of events left after the requirement that there be at least one B-tagged jet in the event is applied. Mistag backgrounds are handled differently. (See text)

Background	W + 3 jets			W + $\geq$ 4jets		
	Total	Pre-Tag	Tag	Total	Pre-Tag	Tag
	Mistags (W+light flavor)					
Wev	67500	2933	–	120302	1092	–
Wmv	194931	2012	–	122500	727	–
Wtv	291047	154	–	261504	135	–
Wbb	236005	1095	521	231562	919	431
	WCC					
Wev	109941	692	107	229199	554	67
Wmv	137487	491	62	251156	378	49
Wc	143612	2377	179	143612	452	46
$WW/WZ/ZZ$, $Z \to \tau\tau$	216567	4673	260	103046	1502	102
single top	236000	1934	1140	236000	459	280

Table 8.3: Monte Carlo samples used for background shapes. Total refers to the total input Monte Carlo, before any cuts are made on the sample. Pre-Tag is the number of events left after all event selection cuts, with the exception of B-tagging, have been applied. Mistag backgrounds are handled differently. (See text)

Filling Histograms

We will examine the features of tagged jets in the candidate events, as well as event quantities in the tagged events.

In the tagged jets we examine the corrected E_T of the jet, jet ϕ, jet η, number of tracks in the jet, jet L_{xy}, and number of vertex tracks in the jet. Histograms for the tagged jets are filled by unweighted entries for every positively tagged jet in the candidate events, for all background and signal samples *with the exception of the mistag background.* The mistag background estimate comes from applying the mistag matrix to taggable jets in the candidate data events. For the jet E_T, jet ϕ, jet η, and number of tracks in the jet, we fill the mistag background histograms using each taggable jet in the pre-tag candidate events, weighted by the negative mistag matrix. We use taggable jets to increase the statistics of the sample. The jet L_{xy} and number of vertex tracks in the jet histograms can only be filled for tagged jets. For the mistag background we fill these plots for each negatively tagged jet in our candidate events, and weight the entry by the negative mistag matrix.

Normalizing Histograms

Variables are filled separately for the signal and each background contribution. These shapes are normalized differently for backgrounds, mistags, and signal shapes. The $t\bar{t}$ signal shape is normalized to the distribution expected based on the measured cross section of 4.5 pb. From the Monte Carlo we measured the distribution of $t\bar{t}$ events in the ≥ 3 jet bins. We found 45% of these fall into the 3 jet bin and 55% are in the ≥ 4 jet bin. Our measured cross section has a total of 35 candidate events, of which 20 can be attributed to $t\bar{t}$. This means we expect 9.1 $t\bar{t}$ events in the 3 jet bin and 11.9 events in the ≥ 4 jet bin. All of the signal shapes are normalized to these

expected values.

The histograms are normalized across all backgrounds *except mistags* in the same way. These plots were filled for each positively tagged jet in the candidate events. For tagged jet quantities we need to take into account the possibility of tagging more than one jet in the event. For these plots we normalize each shape to the value of the expected contribution from Table 7.20, divided by the integral of a plot from that same shape that was only filled on a per-tagged event basis, for example the event $\not{E}_T$ ($\int \text{per} - \text{event plot}$). The normalization for each of the backgrounds *except mistags* for the tagged jet quantities is :

$$Normalization = \frac{Expected\ tagged\ events\ Table\ 7.20}{\int \text{per} - \text{event plot}} \tag{8.3}$$

The mistag plots for tagged jets are filled in two different ways. The E_T, η, ϕ, and the number of good tracks in the jet are filled for every taggable jet, weighted by the negative mistag matrix. These plots are normalized by utilizing equation 8.3. The remainder of the tagged jet quantities (L_{xy}, and number of tracks in the vertex) are filled for each negatively tagged jet in the event, weighted by the negative mistag matrix. For these variables we first normalize the histograms to the number of entries found in the plots filled using taggable jets, for example the jet ϕ ($\int \text{per} - \text{taggable jet plot}$). This is done by multiplying the histogram by the integral of the per-taggable jet plot and dividing by the integral of itself. We then weight the resulting histogram using equation 8.3 :

(8.4)

$$Normalization = \frac{\int \text{per} - \text{taggable jet plot}}{\int \text{tagged jet plot}} \cdot \frac{Expected\ tagged\ events\ Table\ 7.20}{\int \text{per} - \text{event plot}}$$

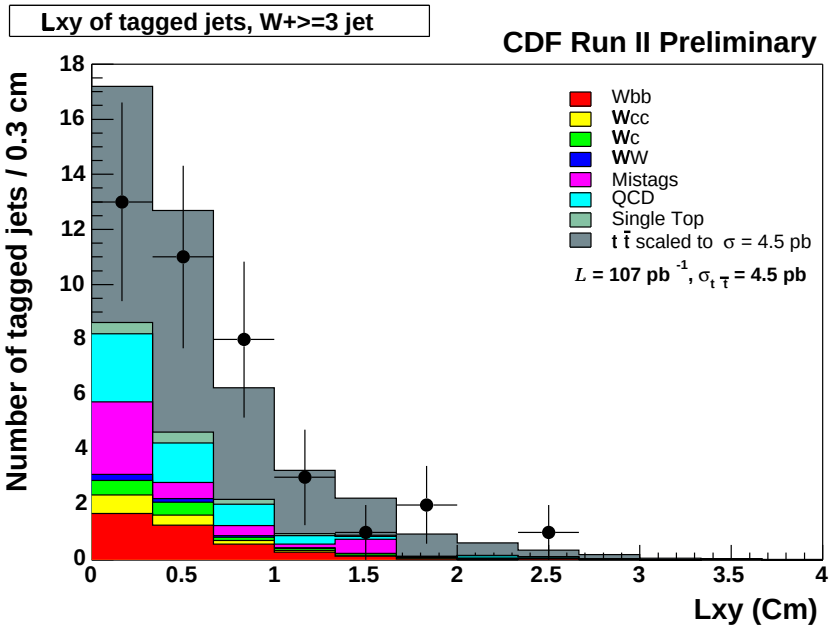

Figure 8.4: L_{xy} of B-tagged jets in Lepton+Jets candidate events in the ≥ 3 jet bin

where "tagged jet plot" is the histogram of the L_{xy} or number of tracks in the vertex.

8.1.3 Results

All normalized shapes are stacked on top of each other, including the shape from the expected $t\bar{t}$ signal. This stacked shape is then plotted overlayed with the shape found from our data points. Shown in Figures 8.4 and 8.5 are examples of these shape comparisons for two tagged jet quantities, L_{xy}, and N_{vtx}. These two plots are crucial for checking the B-tagging algorithm. L_{xy}, as discussed in Section 4.2, is the distance between the primary vertex and the reconstructed secondary vertex of the tagged jets. N_{vtx} is the number of tracks used to reconstruct the secondary vertex. All plots exhibit good agreement between the shape observed in the data and that found from the sum of the expected background and signal shapes.

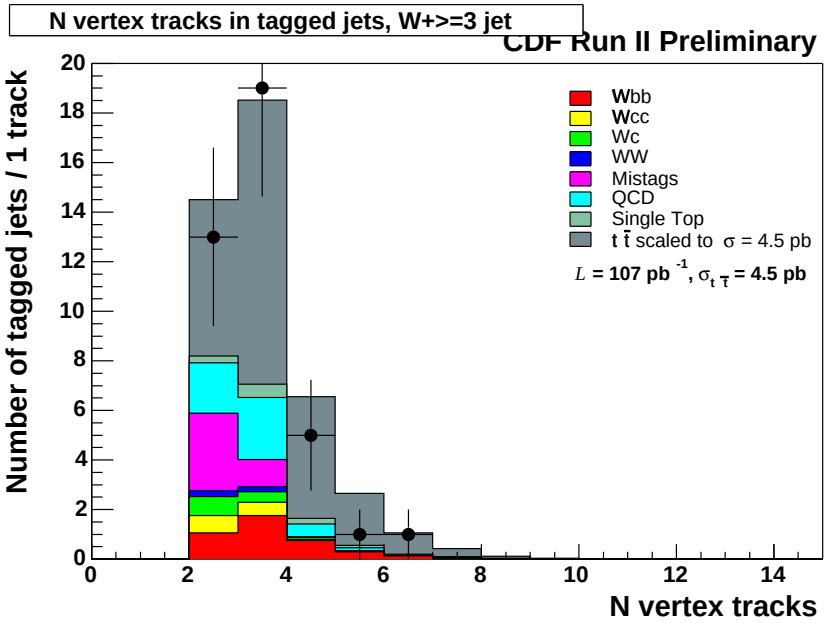

Figure 8.5: Number of vertex tracks of B-tagged jets in Lepton+Jets candidate events in the ≥ 3 jet bin

CHAPTER IX

Optimization Studies

The top event selection requirements used in this analysis are identical to those used to discover the top quark at the Tevatron during Run I. That selection was optimized to look for a top quark of unknown mass, with maximum efficiency. With the top quark now a known object, it is of interest to know if there is a more optimal selection for measurement of the $t\bar{t}$ production cross section.

9.1 Introduction

We explored changes to the $\not\!\!E_T$, jet E_T and jet η cuts, as well as which jet energy corrections were applied. In addition we applied a new technique for estimating the QCD background.

Throughout this chapter the word "baseline" is used to refer to the values measured when using a jet E_T cut of 15 GeV, jet $\mid \eta \mid$ cut of 2.0, and $\not\!\!E_T$ cut of 20 GeV. These are the values used for the lepton+jets B-tagged $t\bar{t}$ cross-section analysis from both Run I and Run II. Please note that this definition of "baseline" does not include any reference to which jet corrections were applied.

9.2 Figures of Merit

We examined four figures of merit simultaneously. These are the total significance, the signal to background ratio, the statistical significance, and the purity. The total significance represents our sensitivity to both the statistical and systematic errors, and was given preference over the other three quantities when optimizing. To verify that the more optimal points were not affecting the top acceptance, and the single and double tagging efficiency, we also evaluated these quantities at each point of optimization.

- Total Significance ($\frac{S}{\sigma_{total}}$)
  - This quantity represents our sensitivity to both the statistical and systematic errors. As we reach higher luminosities our measurement will start to become systematics limited, and the total significance is a measure of how our systematics will be reduced at different cut levels. We expect the systematic uncertainties to dominate with increasing statistics. The total error is the quadratic sum of the statistical error and the systematic error. The systematic error itself is also a quadratic sum, of the systematic error on the expected signal and the systematic error on the background. We find the systematic errors at a given set of cuts by scaling the value found at the baseline. The scale factor is the ratio of total background contribution (or denominator) at the new set of cuts and the value found at the baseline. For example, our baseline denominator found using jet corrections of level 4 is 4.48±0.56 (sys). The denominator found by increasing the jet E_T cut to 20 GeV is 3.90. The new systematic error becomes :

$$\sigma_{E_T\ 20} = 0.56 \cdot \frac{3.90}{4.48} \rightarrow 0.49 \tag{9.1}$$

- S/B
  - The signal to background ratio is a measure of signal strength relative to the background noise.
- Statistical Significance ($\frac{S}{\sqrt{S+B}}$)
  - In a counting experiment, the statistical error on the number of events is approximately the square root of the number of events. Our signal is the number of total observed events minus the number of expected background events, *i.e.* the number of observed top events. The quantity $S+B$ is then the total number of observed events, and the square root is the error on this count. $S/\sqrt{S+B}$ is the significance of the top contribution, relative to the statistical error on the total observed events.
- Purity ($\frac{S}{S+B}$)
  - The signal is the number of observed top events, and $S+B$ is the total number of observed events. The purity is a measure of the total top signal strength relative to the entire observed set of events.
- Top Acceptance ($\epsilon_{t\bar{t}}$)
  - Using the $t\bar{t}$ Monte Carlo sample we find the top acceptance. The number quoted for use in this optimization includes the tagging efficiency, but does not include luminosity.
- Single Tagging Efficiency
  - The single tagging efficiency is found using our $t\bar{t}$ Monte Carlo sample. It is the number of events passing all event selection criterion, having one and only one tagged jet, divided by the total number of events with at least one taggable jet.

- Double Tagging Efficiency
  - The double tagging efficiency is also found using our $t\bar{t}$ Monte Carlo sample. It is the number of events passing all event selection criterion, having two and only two tagged jets, divided by the total number of events with at least one taggable jet.

9.3 Optimizing the QCD Background

This new QCD technique takes the standard Iso vs $\not\!\!E_T$ QCD calculation and applies a cut in ϕ between the leading jet and the event $\not\!\!E_T$. Motivation for the cut is illustrated in Figures 9.1 and 9.2. In Figure 9.1 it can be seen that the QCD events tend to pile up in the $20 < \not\!\!E_T < 30$ GeV region, and there are two definite peaks in the $\triangle\phi$ distribution, at $0.5 > \triangle\phi > 0$ and at $0.5 > \triangle\phi > 3.14$. The $t\bar{t}$ events, shown in Figure 9.2, do not exhibit this tendency. Requiring a cut of $0.5 < \triangle\phi < 2.5$ will not affect our signal events, but will remove a significant portion of the QCD events.

It has been shown that the new QCD cut results in a factor of 3 reduction of the number of expected QCD events compared to using standard Iso vs $\not\!\!E_T$ QCD estimate. (See Reference [78]) This additional cut will become the standard for future versions of the cross section analysis. In addition to the standard figures of merit for optimization (S/B, significance, and purity), we also consider quantities such as the top acceptance and the single and double tagging rates.

9.4 Expected Signal

We determine the expected $t\bar{t}$ signal rate by using the Standard Model cross section of 7 pb and the following equation :

$$N_{t\bar{t}}^{exp} = \sigma_{SM\ t\bar{t}} \cdot (\epsilon_{t\bar{t}} \cdot \int L) \tag{9.2}$$

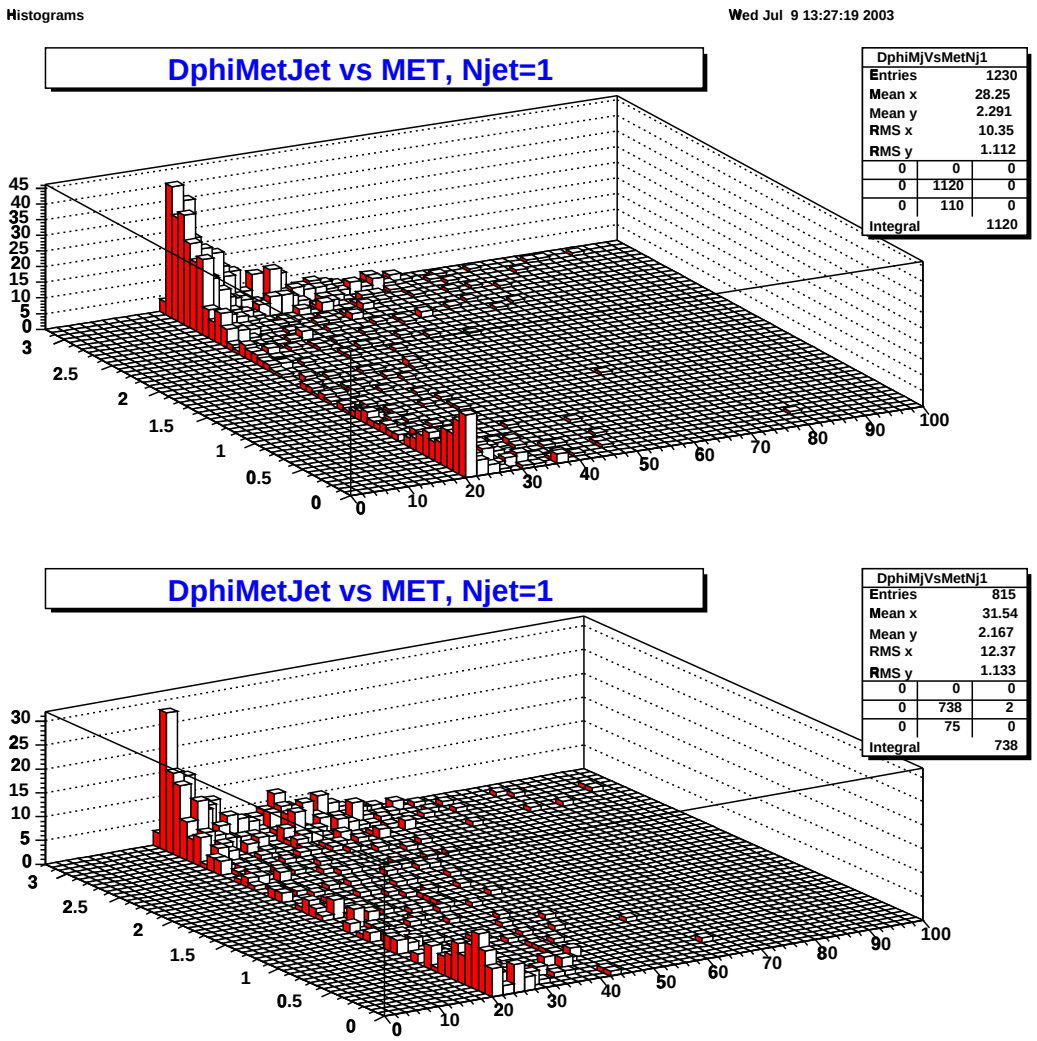

Figure 9.1: $\triangle\phi$ vs $\not\!\!E_T$ for non-isolated lepton events in the data. The standard event selection cut of $\not\!\!E_T > 20$ GeV has already been applied. The plot on the top is for electron events. The bottom displays the distribution for muon events. As mentioned in Section 7.1, events which pass our $\not\!\!E_T$ cut but contain a non-isolated lepton are a good representation of the QCD background to the $t\bar{t}$ production cross section measurement. These figures show the majority of the QCD events exist in the region $20 < \not\!\!E_T < 30$ GeV, and $0.5 > \triangle\phi > 0$, as well as $2.5 > \triangle\phi > 3.14$. [78]

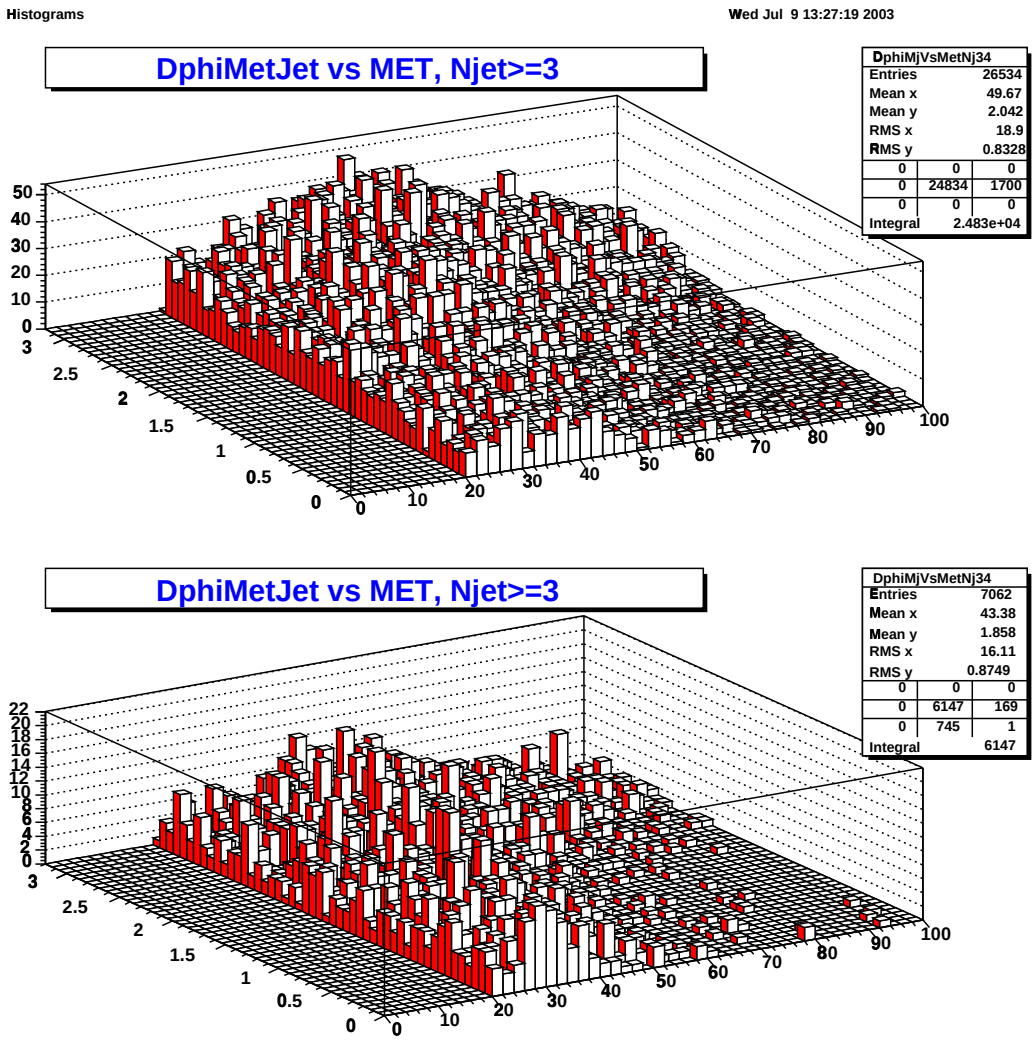

Figure 9.2: $\triangle\phi$ vs $\not\!\!E_T$ for $t\bar{t}$ events found using the ALPGEN Monte Carlo, in the ≥ 3 jet bin region. The standard event selection cut of $\not\!\!E_T > 20$ GeV has already been applied. The plot on the top is for electron events. The bottom displays the distribution for muon events. It can be seen that requiring $0.5 < \triangle\phi < 2.5$ will not affect our signal events. [78]

To estimate the effects of different cut selections we simply remeasure the total efficiency, comprising the tagging efficiency and acceptance, using a sample of $t\bar{t}$ Monte Carlo events. (See Chapter 6.1) The integrated luminosity used for the CEM and CMUP detectors is 107.9 pb^{-1}, and 98 pb^{-1} for the CMX detector.

9.5 Background Estimates

We estimate the expected background contributions for each of our optimization cuts by multiplying the baseline background estimates (Table 9.1) by a scale factor:

$$Bgd\ Estimate_{New\ Cut} = Bgd\ Estimate_{Baseline} \cdot \frac{\#MC\ Entries\ New\ Cut}{\#MC\ Entries\ Baseline} \tag{9.3}$$

The scale factor is the number of tagged events in a background Monte Carlo found by using the test set of cuts, divided by the number found using the baseline set of cuts. The Monte Carlo samples used in this study for each of the backgrounds are the same as those used in the examination of the background contributions. (See Tables 8.1 and 8.2, 8.3) The benefit of using this scale factor is that any changes in tagging efficiency are included in the counting of tagged events.

Our background estimates are found for the 3 and $\geq$4 jet bin separately. We have also corrected the $Wb\bar{b}$, $Wc\bar{c}$, and Wc background estimates shown in Table 9.1 to match the $t\bar{t}$-corrected total background estimate. Values displayed in this table are before correcting. (See Section 7.2) We scale the $t\bar{t}$-corrected backgrounds when examining the varying sets of cuts.

To compute our expected contribution from the QCD background for each of the sets of cuts we apply a technique similar to the one above for the other backgrounds. It is not entirely straightforward to measure the tagged events at the varying sets of cuts for the new QCD calculation, so we employ a smart scaling from the Iso vs $\not\!\!E_T$ QCD method. Recall that the new QCD cut was found to reduce the rate of that

background by a factor of 3. Therefore, to find the number of tagged events at a given set of cuts we count the number of tagged events in the data found by using the standard Iso vs $\not\!\!E_T$ QCD calculation, and scale by a factor of 1/3. This gives us the numerator of equation 9.3. The denominator of equation 9.3 is the number of tagged events found at the baseline set of cuts, applying the new QCD cut.

We use the $Wb\bar{b}$, $Wc\bar{c}$, and Wc Monte Carlo samples to estimate the change in W plus heavy-flavor backgrounds. We assume the heavy-flavor fractions are constant as a function of the kinematic cuts. The original mistag background estimate for our baseline analysis comes from running the mistag matrix over data. To estimate the contribution to the backgrounds from the mistags for each of our optimization cuts we apply Equation 9.3 to the W+light parton Monte Carlo samples. The counts of tagged events used in the scale factor are the raw counts recorded, and are not weighted by the mistag matrix. The baseline WW and single top backgrounds are estimated from Monte Carlo samples, so it is straightforward to measure the change in background from the Monte Carlo.

Background	W + 3 jets	W + $\geq$ 4jets
$-L_{xy}$	2.70 ± 0.40	1.50 ± 0.30
$Wb\bar{b}$	2.42 ± 0.62	1.04 ± 0.32
$Wc\bar{c}$	0.89 ± 0.27	0.35 ± 0.13
Wc	1.00 ± 0.38	0.30 ± 0.12
WW	0.46 ± 0.08	0.08 ± 0.03
Iso vs $\not\!\!E_T$ QCD	3.05 ± 0.59	1.54 ± 0.30
$\triangle\phi$ QCD	1.0 ± 0.22	0.50 ± 0.13
single top	0.79 ± 0.11	0.15 ± 0.02
Total (Iso vs $\not\!\!E_T$ QCD)	11.31 ± 1.27	4.96 ± 0.64
Corrected (Iso vs $\not\!\!E_T$ QCD)	15.45 ± 1.43	
Corrected ($\triangle\phi$ QCD)	12.36 ± 1.30	

Table 9.1: Background estimates for our baseline analysis, using "level 4" jet corrections. (See Section 3.5.1) Results shown are for both the Iso vs $\not\!\!E_T$ and the $\triangle\phi$ methods for estimating the background contribution due to QCD. The values shown for the $Wb\bar{b}$, $Wc\bar{c}$, and Wc backgrounds have not been corrected for the expected residual $t\bar{t}$ component.

In addition to examining the changing the $\not\!\!E_T$, jet E_T and jet η cuts, we also looked

at changing the types of jet energy corrections which were applied. Our cross section measurement was carried out using the first four jet corrections listed in Section 3.5.1 : relative energy, time dependence, raw energy scale, and multiple interactions. These group of corrections are known internally as the "level 4" corrections. In addition we also tried including absolute energy scale corrections ("level 5"), and absolute and underlying event corrections ("level 6"). To find the expected backgrounds for Level 5 and Level 6 jet corrections at the baseline set of cuts we scale the Level 4 estimates (Table 9.1) using the following equation :

(9.4)

$$bgd\ estimate_LEVEL5(6) = bgd\ estimate_LEVEL4 \cdot \frac{\sum\ tagged\ events_{LEVEL\ 5(6)}}{\sum\ tagged\ events_{LEVEL\ 4}}$$

For a given background we find the number of tagged events in the Monte Carlo for the Level 4 and Level 5(6) jet corrections. The ratio of these two numbers becomes the scale factor by which we multiply the original baseline Level 4 background estimate. Table 9.2 compares the backgrounds between jet levels of 4, 5, and 6, for the ≥ 3 jet bin. The QCD background is found using the Iso vs $\not\!\!E_T$ method with the additional $\triangle\phi$ cut, and the $Wb\bar{b}$, $Wc\bar{c}$, and Wc backgrounds shown are before and after correcting for $t\bar{t}$.

9.6 Results

To determine which set of test cuts provides the most optimal point for this analysis we examine our four figures of merit relative to the baseline results. Our primary concern when choosing the most optimal point at each level is finding the point which exhibits the maximum in increase in total significance over the baseline value. We encounter instances where the maximum increase in total significance is

Background	Level 4 Uncorrected	Level 4 $t\bar{t}$ Corrected	Level 5	Level 6
$-L_{xy}$	4.20	4.20	7.28	6.75
Wbb	3.46	2.96	4.31	4.09
$Wc\bar{c}$	1.24	1.07	1.73	1.59
Wc	1.30	1.05	1.74	1.64
WW	0.54	0.54	0.60	0.59
$\triangle\phi$ QCD	1.50	1.50	1.20	1.20
single top	0.94	0.94	1.44	1.36
Total	13.18	12.26	18.30	17.22

Table 9.2: Background estimates for jet correction Levels 4, 5, and 6, in the ≥ 3 jet bin. Level 4 is shown both before and after $t\bar{t}$ corrections for the $Wb\bar{b}$, $Wc\bar{c}$, and Wc backgrounds. Levels 5 and 6 are shown after $t\bar{t}$ corrections only. The $\triangle\phi$ cut is applied when calculating the QCD background. All values are shown for the baseline set of cuts. (See Section 9.1)

stable across several sets of test cuts. In these cases we then examine the other three figures of merit and pick as most optimal the point which has a maximum for the majority of these other figures of merit. The following pages display tables of E_T vs $\not\!\!E_T$ and E_T vs $\mid \eta \mid$ for jet corrections levels 4, 5, and 6. In each chart the baseline number is shown in italics, and the point chosen to be most optimal is highlighted in bold print.

9.6.1 Optimization with Level 4 Jet Corrections

Level 4 jet corrections apply a scale factor to all tight jets in the event to account for relative energy, time dependent, energy scale, and multiple interaction energy corrections. Table 9.4 shows the figures of merit as we vary jet E_T vs $\not\!\!E_T$ at Level 4, and Table 9.5 as we vary jet E_T vs jet $\mid \eta \mid$.

In Table 9.4 there is clearly one point with maximum total and statistical significance. This point is found by increasing our jet E_T to 20 GeV. In Table 9.5 there are three points with maximal total and systematic significance. These points are found in the last three columns of the second row, representing jet E_T of 20 GeV and $\mid \eta \mid$ values of 2.0, 2.25, and 2.5. In all three cases we see the statistical significance values are the same, and the total significance values are the same. In addition, the purity

is comparable. We optimize this set of cuts based on the fourth figure of merit, the signal to background ratio. We find the maximal point occurs at jet E_T of 20 GeV and $\mid \eta \mid$ of 2.0. The final point chosen which is most optimal for jet corrections of Level 4 is at jet $E_T \geq 20$ GeV, jet $\mid \eta \mid \leq 2.0$, and event $\not{E}_T \geq 20$ GeV. The only variable to change from our baseline cross section analysis cuts is the jet E_T, increasing by 5 GeV. This point provides us with a 15% increase in the purity of the sample, and an 84% increase in the signal to background ratio over the original analysis jet E_T cut of 15 GeV.

Figure 9.3 shows the four figures of merit for Level 4, as a function of the jet E_T cut. Between jet E_T of 15 and 20 GeV the total significance experiences a 2% increase, while the statistical significance remains flat. The purity increases by 15%.

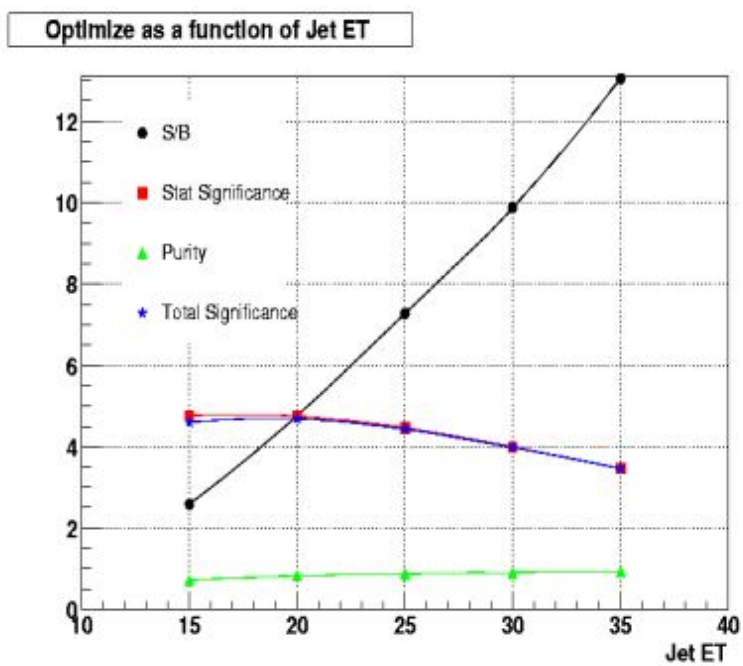

Figure 9.3: Optimization results for Level 4 jet corrections, holding $\not{E}_T$ and η constant and varying jet E_T. Between jet E_T of 15 and 20 GeV the total significance experiences a 2% increase, while the statistical significance remains flat. The purity increases by 15%. The signal to background experiences a significant increase of 84% as we increase the jet E_T cut to 20 GeV.

9.6.2 Optimization with Level 5 Jet Corrections

Level 5 corrects for all factors present at Level 4, and also includes absolute energy corrections. See Table 9.6 for jet E_T vs $\not{E}_T$, and Table 9.7 for jet E_T vs jet $\mid \eta \mid$.

Table 9.6 (jet E_T vs $\not{E}_T$) has two points with maximal total significance, at $\not{E}_T$ of 20 GeV, and jet E_T of 20 and 25 GeV. Here we find that the point at jet E_T of 20 has a higher statistical significance, but a lower signal to background ratio and purity. The total significance is comparable between these two points. There are two motivations for choosing the point at jet E_T of 25 to be the most optimal. In optimizing we look for the point with the maximum in the largest number of figures of merit. Of the four primary figures of merit (signal to background, statistical significance, purity, and total significance), this point is higher in two and equivalent in one to the point at jet E_T of 20. The second rationale is the implications that this optimization point will have for other analyses. This analysis provides the event selection and background normalizations for many other analyses, including the $\mid V_{tb} \mid$ measurement, W helicity, and the top mass analysis. A larger value in purity and signal to background will assure the robustness of these other analyses, in regards to event selection and backgrounds.

For table 9.7 (jet E_T vs $\mid \eta \mid$) the most optimal point is found in a similar fashion. Here we find seven points with equivalent total significance. These are in the jet E_T 20 row, for $\mid \eta \mid$ values 1.75, 2.0, 2.25, and 2.5, and in the jet E_T 25 row, for $\mid \eta \mid$ values 2.0, 2.25, and 2.5. The points in the jet E_T 20 row all have a larger statistical significance relative to the jet E_T 25 row, but are lower in purity and signal to background. As before in the jet E_T vs $\not{E}_T$ optimization we only look at points having the largest number of our figures of merit at a maximum. This leaves us with the three points in the jet E_T 25 row. We find that the statistical

significance, purity, and total significance are equivalent across all three points. The defining figure of merit, then, must be the signal to background. This occurs at an $\mid \eta \mid$ value of 2.0. Therefore, the maximal point at Level 5 is found by changing the jet E_T cut to 25 GeV. The jet η and event $\not\!\!E_T$ cuts remain unchanged from our baseline values.

9.6.3 Optimization with Level 6 Jet Corrections

Level 6 jet corrections include those found at Level 5, plus underlying event corrections. See Table 9.8 for jet E_T vs $\not\!\!E_T$, and Table 9.9 for jet E_T vs jet $\mid \eta \mid$.

Table 9.8 (jet E_T vs $\not\!\!E_T$) also has two points with maximal total significance, at $\not\!\!E_T$ of 20 GeV, and jet E_T of 20 and 25 GeV. As for Level 5 we find that the point at jet E_T of 20 has a higher statistical significance, but a lower signal to background ratio and purity. The total significance is comparable between these two points. Again we choose the point with higher signal to background and purity, the point at jet E_T of 25. Table 9.9 also displays the same behavior as in Level 5 jet corrections, with the highest total significance points residing in the jet E_T 20 and 25 rows. Here the row at jet E_T 20 has a higher statistical significance, but lower signal to background and purity. The total significance is constant across these two jet E_T rows. The most optimal point at Level 6 is the one in which the jet η and $\not\!\!E_T$ values do not change from the baseline, but the jet E_T cut is increased to 25 GeV.

9.7 Conclusions

The most optimal point for each level of jet corrections is shown in Table 9.3. The point of highest statistical and total significance occurs at Level 5, with a jet E_T cut of 25 GeV, jet $\mid \eta \mid$ cut of 2.0, and event $\not\!\!E_T$ of 20 GeV.

	BASELINE	Level 4	Level 5	Level 6
jet E_T (GeV)	15	20	25	25
jet $\mid \eta \mid$	2	2	2	2
MET (GeV)	20	20	20	20
S/total	4.60	4.69	4.73	4.71
S/B	2.59	4.77 ± 0.08	5.05 ± 0.08	5.23 ± 0.09
Significance	4.76	4.75 ± 0.01	4.78 ± 0.01	4.76 ± 0.01
Purity	0.72	0.83 ± 0.01	0.83 ± 0.01	0.84 ± 0.01
top accep	0.042	0.037 ± 0.002	0.037 ± 0.002	0.036 ± 0.002

Table 9.3: Most optimal points for Level 4, Level 5, and Level 6 jet corrections.

9.8 Validity of Total Significance as a Figure of Merit

We have pegged this optimization study to a certain luminosity (107.9 pb^{-1} for the CEM and CMUP detectors, and 98 pb^{-1} for the CMX detector). We argue that optimizing on the total sensitivity will allow this analysis to become more robust at higher luminosities. To test this theory we conduct two additional studies of the optimization. In one case we use our measured cross section of 4.5 pb to generate our expected signal. (See Tables 9.10 and 9.11) In the second case we use the standard model cross section of 7 pb, but double our luminosity (to 215.8 pb^{-1} for CEM and CMUP, 196 pb^{-1} for the CMX). (See Tables 9.12 and 9.13) We conducted these tests using level 5 jet corrections only.

Table 9.10 is the chart of E_T vs $\not\!\!E_T$ found when using our measured cross section of 4.5 pb to generate the expected signal. In this case it is quite clear that there is one point with a maximum in total significance, at $\not\!\!E_T$ 20 and E_T 25. Table 9.11, E_T vs $\mid \eta \mid$ using our measured cross section, has four maximum points in which the statistical significance, purity, and total significance are equal. These are located at a jet E_T cut value of 25 GeV and $\mid \eta \mid$ of 1.75, 2.0, 2.25, and 2.5. The defining value, then, is the signal to background. The two highest signal to background ratios are at $\mid \eta \mid$ of 1.75 and 2.0. We find that there is a slightly higher signal to background

at an $\mid \eta \mid$ value of 1.75, but the consensus of Top Physics working group is to avoid making changes to the η cut based solely on a small increase in signal to background. For this study we conclude that changing the jet E_T cut to $\geq$ 25 GeV provides the point of highest optimization.

Table 9.12 examines E_T vs $\not{E}_T$ cuts when we use the standard model cross section of 7 pb, but double our luminosity. The values found using $\not{E}_T$ 20 and E_T 20 and 25 are maximal in total significance. The point at E_T 25, however, has a higher signal to background and purity value than the point at E_T 20. Table 9.13, for E_T vs $\mid \eta \mid$, finds 8 points which are similar in the maximal value of total significance. These are all η points in the jet E_T 20 row, and $\mid \eta \mid$ of 2.0, 2.25, and 2.5 in the jet E_T 25 row. Again as in the case of the standard Level 5 optimization study, the purity and signal to background are the highest in the jet E_T 25 row. Comparing the three optimal points in the jet E_T 25 row we find that the statistical significance, purity, and total significance are comparable between all points. The defining value for optimization is again the signal to background, and is found at jet E_T 25, $\mid \eta \mid$ of 2.0. The point chosen in the original optimization study for Level 5 (jet $E_T \geq$ 25 GeV) is still the most optimal.

Jet E_T :	15	20	25	30	35
MET : 20 GeV					
S/total	*4.60*	**4.69**	4.43	3.98	3.46
S/B	*2.59*	**4.76 ± 0.08**	7.28 ± 0.19	9.87 ± 0.34	13.05 ± 0.67
Significance	*4.76*	**4.75 ± 0.01**	4.46 ± 0.01	3.99 ± 0.01	3.46 ± 0.01
Purity	*0.72*	**0.83 ± 0.01**	0.88 ± 0.01	0.91 ± 0.01	0.93 ± 0.01
top accep	*0.042*	**0.037 ± 0.002**	0.030 ± 0.002	0.024 ± 0.003	0.017 ± 0.003
ϵ_1	*0.45*	**0.45 ± 0.001**	0.46 ± 0.001	0.46 ± 0.001	0.46 ± 0.001
ϵ_2	*0.16*	**0.16 ± 0.001**	0.16 ± 0.001	0.17 ± 0.002	0.18 ± 0.003
MET : 25 GeV					
S/total	4.53	4.53	4.27	3.83	3.31
S/B	2.91 ± 0.02	4.92 ± 0.08	7.41 ± 0.19	10.02 ± 0.38	13.17 ± 0.59
Significance	4.65 ± 0.01	4.59 ± 0.01	4.30 ± 0.01	3.84 ± 0.01	3.32 ± 0.01
Purity	0.74 ± 0.01	0.83 ± 0.01	0.88 ± 0.01	0.91 ± 0.01	0.93 ± 0.01
top accep	0.039 ± 0.001	0.034 ± 0.002	0.028 ± 0.003	0.022 ± 0.003	0.016 ± 0.003
ϵ_1	0.45 ± 0.0001	0.45 ± 0.001	0.46 ± 0.001	0.46 ± 0.001	0.46 ± 0.001
ϵ_2	0.16 ± 0.0004	0.16 ± 0.001	0.16 ± 0.001	0.17 ± 0.002	0.18 ± 0.003
MET : 30 GeV					
S/total	4.37	4.35	4.08	3.64	3.19
S/B	3.06 ± 0.03	5.16 ± 0.09	7.76 ± 0.19	10.52 ± 0.38	14.05 ± 0.73
Significance	4.47 ± 0.01	4.39 ± 0.01	4.10 ± 0.01	3.65 ± 0.01	3.20 ± 0.01
Purity	0.75 ± 0.02	0.84 ± 0.01	0.89 ± 0.01	0.91 ± 0.01	0.93 ± 0.01
top accep	0.035 ± 0.002	0.031 ± 0.002	0.025 ± 0.003	0.012 ± 0.003	0.015 ± 0.003
ϵ_1	0.45 ± 0.0002	0.45 ± 0.001	0.46 ± 0.001	0.46 ± 0.001	0.46 ± 0.001
ϵ_2	0.16 ± 0.001	0.16 ± 0.0003	0.16 ± 0.001	0.17 ± 0.002	0.18 ± 0.003

Table 9.4: Level 4 jet E_T vs MET, with $\mid \eta \mid$ held constant at 2. The most optimal point is found by increasing the jet E_T cut to 20 GeV, and not changing the MET. Numbers in italics are the baseline, bold-faced numbers are the most optimal.

Jet $\mid \eta \mid$:	1.5	1.75	2.0	2.25	2.5
Jet E_T : 15 GeV					
S/total	4.65	4.67	*4.60*	4.64	4.62
S/B	3.47 ± 0.04	3.07 ± 0.03	*2.59*	2.63 ± 0.02	2.52 ± 0.02
Significance	4.74 ± 0.01	4.79 ± 0.01	*4.76*	4.80 ± 0.01	4.79 ± 0.01
Purity	0.78 ± 0.02	0.75 ± 0.01	*0.72*	0.72 ± 0.01	0.72 ± 0.01
top accep	0.039 ± 0.001	0.041 ± 0.001	*0.042*	0.043 ± 0.001	0.043 ± 0.001
ϵ_1	0.46 ± 0.001	0.45 ± 0.001	*0.45*	0.45 ± 0.0003	0.45 ± 0.0004
ϵ_2	0.17 ± 0.002	0.16 ± 0.001	*0.16*	0.16 ± 0.001	0.15 ± 0.001
Jet E_T : 20 GeV					
S/total	4.59	4.66	**4.69**	4.70	4.69
S/B	5.94 ± 0.11	5.15 ± 0.09	**4.77 ± 0.08**	4.48 ± 0.07	4.33 ± 0.06
Significance	4.64 ± 0.01	4.71 ± 0.01	**4.75 ± 0.01**	4.76 ± 0.01	4.76 ± 0.01
Purity	0.86 ± 0.01	0.84 ± 0.01	**0.83 ± 0.01**	0.82 ± 0.01	0.81 ± 0.01
top accep	0.034 ± 0.002	0.036 ± 0.002	**0.037 ± 0.002**	0.037 ± 0.002	0.037 ± 0.002
ϵ_1	0.46 ± 0.001	0.46 ± 0.001	**0.45 ± 0.001**	0.45 ± 0.0003	0.45 ± 0.0002
ϵ_2	0.17 ± 0.002	0.16 ± 0.001	**0.16 ± 0.001**	0.16 ± 0.0002	0.16 ± 0.0004
Jet E_T : 25 GeV					
S/total	4.29	4.39	4.43	4.45	4.45
S/B	8.75 ± 0.30	7.85 ± 0.20	7.28 ± 0.19	6.96 ± 0.17	6.71 ± 0.16
Significance	4.31 ± 0.01	4.42 ± 0.01	4.46 ± 0.01	4.48 ± 0.01	4.48 ± 0.01
Purity	0.90 ± 0.01	0.89 ± 0.01	0.88 ± 0.01	0.87 ± 0.01	0.87 ± 0.01
top accep	0.028 ± 0.003	0.029 ± 0.002	0.030 ± 0.002	0.031 ± 0.002	0.031 ± 0.002
ϵ_1	0.46 ± 0.001	0.46 ± 0.001	0.46 ± 0.001	0.46 ± 0.001	0.46 ± 0.001
ϵ_2	0.18 ± 0.003	0.17 ± 0.002	0.16 ± 0.001	0.16 ± 0.001	0.16 ± 0.001
Jet E_T : 30 GeV					
S/total	3.84	3.94	3.97	3.99	3.96
S/B	11.47 ± 0.41	10.57 ± 0.40	9.76 ± 0.33	9.45 ± 0.31	8.10 ± 0.26
Significance	3.86 ± 0.01	3.95 ± 0.01	3.99 ± 0.01	4.01 ± 0.01	3.98 ± 0.01
Purity	0.92 ± 0.01	0.91 ± 0.01	0.91 ± 0.01	0.90 ± 0.01	0.89 ± 0.01
top accep	0.022 ± 0.003	0.023 ± 0.003	0.024 ± 0.003	0.024 ± 0.003	0.024 ± 0.003
ϵ_1	0.46 ± 0.001	0.46 ± 0.001	0.46 ± 0.001	0.46 ± 0.001	0.46 ± 0.001
ϵ_2	0.18 ± 0.003	0.17 ± 0.003	0.17 ± 0.002	0.17 ± 0.002	0.17 ± 0.002
Jet E_T : 35 GeV					
S/total	3.33	3.40	3.44	3.45	3.45
S/B	14.84 ± 0.75	13.71 ± 0.76	12.94 ± 0.66	12.31 ± 0.59	11.89 ± 0.55
Significance	3.33 ± 0.01	3.41 ± 0.01	3.45 ± 0.01	3.46 ± 0.01	3.46 ± 0.01
Purity	0.94 ± 0.01	0.93 ± 0.01	0.93 ± 0.01	0.92 ± 0.01	0.92 ± 0.01
top accep	0.016 ± 0.003	0.017 ± 0.003	0.017 ± 0.003	0.017 ± 0.003	0.017 ± 0.003
ϵ_1	0.46 ± 0.002	0.46 ± 0.001	0.46 ± 0.001	0.46 ± 0.001	0.46 ± 0.001
ϵ_2	0.19 ± 0.004	0.18 ± 0.004	0.18 ± 0.003	0.18 ± 0.003	0.18 ± 0.00

Table 9.5: Level 4 jet E_T vs jet $\mid \eta \mid$, with MET held constant at 20 GeV. The most optimal point is found by increasing the jet E_T cut to 20 GeV, and not changing the η cut. Numbers in italics are the baseline, bold-faced numbers are the most optimal.

Jet E_T :	15	20	25	30	35
MET : 20 GeV					
S/total	*4.40*	4.75	**4.73**	4.50	4.12
S/B	*1.84*	3.24 ± 0.04	**5.05 ± 0.08**	7.25 ± 0.18	9.52 ± 0.29
Significance	*4.67*	4.87 ± 0.01	**4.78 ± 0.01**	4.53 ± 0.01	4.14 ± 0.01
Purity	*0.65*	0.76 ± 0.01	**0.83 ± 0.01**	0.88 ± 0.01	0.90 ± 0.01
top accep	*0.045*	0.041 ± 0.001	**0.037 ± 0.002**	0.031 ± 0.002	0.025 ± 0.003
ϵ_1	*0.45*	0.45 ± 0.0003	**0.45 ± 0.001**	0.46 ± 0.001	0.46 ± 0.001
ϵ_2	*0.16*	0.16 ± 0.001	**0.16 ± 0.001**	0.16 ± 0.001	0.17 ± 0.002
MET : 25 GeV					
S/total	4.37	4.64	4.59	4.36	3.99
S/B	2.01 ± 0.01	3.38 ± 0.04	5.22 ± 0.10	7.38 ± 0.18	9.72 ± 0.32
Significance	4.59 ± 0.01	4.74 ± 0.01	4.64 ± 0.01	4.39 ± 0.01	4.00 ± 0.01
Purity	0.67 ± 0.01	0.77 ± 0.01	0.84 ± 0.01	0.88 ± 0.01	0.91 ± 0.01
top accep	0.042 ± 0.001	0.039 ± 0.002	0.034 ± 0.002	0.029 ± 0.003	0.024 ± 0.003
ϵ_1	0.45 ± 0.0002	0.45 ± 0.0004	0.45 ± 0.001	0.46 ± 0.001	0.46 ± 0.001
ϵ_2	0.16 ± 0.0003	0.16 ± 0.001	0.16 ± 0.001	0.16 ± 0.001	0.17 ± 0.002
MET : 30 GeV					
S/total	4.27	4.49	4.42	4.19	3.83
S/B	2.12 ± 0.01	3.54 ± 0.05	5.43 ± 0.10	7.63 ± 0.21	10.09 ± 0.32
Significance	4.45 ± 0.01	4.57 ± 0.01	4.47 ± 0.01	4.21 ± 0.01	3.85 ± 0.01
Purity	0.68 ± 0.02	0.78 ± 0.02	0.84 ± 0.01	0.88 ± 0.01	0.91 ± 0.01
top accep	0.039 ± 0.002	0.036 ± 0.002	0.031 ± 0.002	0.027 ± 0.003	0.022 ± 0.003
ϵ_1	0.45 ± 0.0003	0.45 ± 0.0002	0.45 ± 0.0004	0.45 ± 0.001	0.46 ± 0.001
ϵ_2	0.16 ± 0.0002	0.16 ± 0.001	0.16 ± 0.001	0.16 ± 0.001	0.17 ± 0.0021

Table 9.6: Level 5 jet E_T vs MET, with $|\eta|$ held constant at 2. The most optimal point is found by increasing the jet E_T cut to 25 GeV, holding the MET steady at 20 GeV. Numbers in italics are the baseline, bold-faced numbers are the most optimal.

Jet $\mid \eta \mid$:	1.5	1.75	2.0	2.25	2.5
Jet E_T : 15 GeV					
S/total	4.53	4.51	*4.40*	4.39	4.34
S/B	2.40 ± 0.02	2.12 ± 0.01	*1.84*	1.78 ± 0.01	1.70 ± 0.01
Significance	4.71 ± 0.01	4.73 ± 0.01	*4.67*	4.68 ± 0.01	4.65 ± 0.01
Purity	0.71 ± 0.02	0.68 ± 0.01	*0.65*	0.64 ± 0.01	0.63 ± 0.01
top accep	0.042 ± 0.001	0.044 ± 0.001	*0.045*	0.046 ± 0.001	0.046 ± 0.001
ϵ_1	0.46 ± 0.001	0.45 ± 0.0004	*0.45*	0.45 ± 0.0003	0.45 ± 0.0003
ϵ_2	0.17 ± 0.001	0.16 ± 0.001	*0.16* 0	0.15 ± 0.001	0.15 ± 0.001
Jet E_T : 20 GeV					
S/total	4.70	4.75	4.75	4.73	4.72
S/B	3.99 ± 0.06	3.53 ± 0.05	3.24 ± 0.04	3.02 ± 0.032	2.90 ± 0.03
Significance	4.78 ± 0.01	4.85 ± 0.01	4.87 ± 0.01	4.86 ± 0.01	4.85 ± 0.07
Purity	0.80 ± 0.02	0.78 ± 0.02	0.76 ± 0.01	0.75 ± 0.01	0.74 ± 0.01
top accep	0.038 ± 0.002	0.040 ± 0.002	0.041 ± 0.001	0.042 ± 0.001	0.042 ± 0.001
ϵ_1	0.46 ± 0.001	0.45 ± 0.001	0.45 ± 0.0003	0.45 ± .0001	0.45 ± 0.0002
ϵ_2	0.17 ± 0.002	0.16 ± 0.001	0.16 ± 0.001	0.16 ± 0.0003	0.15 ± 0.001
Jet E_T : 25 GeV					
S/total	4.62	4.69	**4.73**	4.73	4.72
S/B	6.16 ± 0.14	5.44 ± 0.10	**5.05 ± 0.08**	4.71 ± 0.08	4.55 ± 0.07
Significance	4.66 ± 0.01	4.74 ± 0.01	**4.78 ± 0.01**	4.79 ± 0.01	4.79 ± 0.01
Purity	0.86 ± 0.01	0.84 ± 0.01	**0.83 ± 0.01**	0.82 ± 0.01	0.82 ± 0.01
top accep	0.034 ± 0.002	0.036 ± 0.002	**0.037 ± 0.002**	0.037 ± 0.002	0.037 ± 0.002
ϵ_1	0.46 ± 0.001	0.46 ± 0.001	**0.45 ± 0.001**	0.45 ± 0.0004	0.45 ± 0.0004
ϵ_2	0.17 ± 0.002	0.16 ± 0.001	**0.16 ± 0.001**	0.16 ± 0.001	0.16 ± 0.0004
Jet E_T : 30 GeV					
S/total	4.36	4.46	4.50	4.51	4.51
S/B	8.68 ± 0.25	7.78 ± 0.19	7.25 ± 0.18	6.85 ± 0.16	6.63 ± 0.15
Significance	4.38 ± 0.01	4.49 ± 0.01	4.53 ± 0.01	4.55 ± 0.01	4.55 ± 0.01
Purity	0.90 ± 0.01	0.89 ± 0.01	0.88 ± 0.01	0.87 ± 0.01	0.87 ± 0.01
top accep	0.029 ± 0.002	0.030 ± 0.002	0.031 ± 0.002	0.032 ± 0.002	0.032 ± 0.002
ϵ_1	0.46 ± 0.001	0.46 ± 0.001	0.46 ± 0.001	0.45 ± 0.001	0.45 ± 0.001
ϵ_2	0.18 ± 0.003	0.17 ± 0.002	0.16 ± 0.001	0.16 ± 0.001	0.16 ± 0.001
Jet E_T : 35 GeV					
S/total	3.99	4.08	4.13	4.14	4.14
S/B	11.26 ± 0.37	10.35 ± 0.35	9.71 ± 0.30	9.17 ± 0.27	8.87 ± 0.25
Significance	4.00 ± 0.01	4.10 ± 0.01	4.14 ± 0.01	4.16 ± 0.01	4.16 ± 0.01
Purity	0.92 ± 0.01	0.91 ± 0.010	0.91 ± 0.01	0.90 ± 0.01	0.90 ± 0.01
top accep	0.023 ± 0.003	0.025 ± 0.003	0.025 ± 0.003	0.026 ± 0.003	0.026 ± 0.003
ϵ_1	0.46 ± 0.001	0.46 ± 0.001	0.46 ± 0.001	0.46 ± 0.001	0.46 ± 0.001
ϵ_2	0.18 ± 0.003	0.17 ± 0.002	0.17 ± 0.002	0.16 ± 0.002	0.16 ± 0.002

Table 9.7: Level 5 jet E_T vs jet $\mid \eta \mid$, with MET held constant at 20 GeV. The most optimal point is found by increasing the jet E_T cut to 25 GeV, and not changing the η cut. Numbers in italics are the baseline, bold-faced numbers are the most optimal.

Jet E_T :	15	20	25	30	35
MET : 20 GeV					
S/total	*4.45*	4.76	**4.71**	4.46	4.08
S/B	*1.94*	3.39 ± 0.04	**5.23 ± 0.09**	7.50 ± 0.17	9.83 ± 0.32
Significance	*4.69*	4.86 ± 0.01	**4.76 ± 0.01**	4.49 ± 0.01	4.10 ± 0.01
Purity	*0.66*	0.77 ± 0.01	**0.84 ± 0.01**	0.88 ± 0.01	0.91 ± 0.01
top accep	*0.045*	0.0410 ± 0.001	**0.036 ± 0.002**	0.031 ± 0.002	0.025 ± 0.003
ϵ_1	*0.45*	0.45 ± 0.0003	**0.45 ± 0.001**	0.46 ± 0.001	0.46 ± 0.001
ϵ_2	*0.16*	0.16 ± 0.001	**0.16 ± 0.001**	0.16 ± 0.001	0.17 ± 0.002
MET : 25 GeV					
S/total	4.41	4.64	4.57	4.32	3.94
S/B	2.12 ± 0.01	3.52 ± 0.04	5.38 ± 0.10	7.60 ± 0.19	9.91 ± 0.35
Significance	4.61 ± 0.01	4.73 ± 0.01	4.62 ± 0.01	4.35 ± 0.01	3.96 ± 0.01
Purity	0.68 ± 0.01	0.78 ± 0.01	0.84 ± 0.01	0.88 ± 0.01	0.91 ± 0.01
top accep	0.042 ± 0.001	0.038 ± 0.002	0.034 ± 0.002	0.029 ± 0.002	0.023 ± 0.003
ϵ_1	0.45 ± 0.0002	0.45 ± 0.0004	0.45 ± 0.001	0.46 ± 0.001	0.46 ± 0.001
ϵ_2	0.16 ± 0.0003	0.16 ± 0.001	0.16 ± 0.001	0.16 ± 0.001	0.17 ± 0.002
MET : 30 GeV					
S/total	4.30	4.48	4.40	4.15	3.79
S/B	2.24 ± 0.01	3.70 ± 0.05	5.60 ± 0.11	7.88 ± 0.22	10.35 ± 0.34
Significance	4.47 ± 0.01	4.56 ± 0.01	4.44 ± 0.01	4.17 ± 0.01	3.80 ± 0.01
Purity	0.69 ± 0.02	0.79 ± 0.02	0.85 ± 0.01	0.89 ± 0.01	0.91 ± 0.01
top accep	0.039 ± 0.002	0.035 ± 0.002	0.031 ± 0.002	0.026 ± 0.003	0.021 ± 0.003
ϵ_1	0.45 ± 0.0003	0.45 ± 0.0002	0.45 ± 0.001	0.45 ± 0.001	0.45 ± 0.001
ϵ_2	0.16 ± 0.0003	0.16 ± 0.001	0.16 ± 0.001	0.16 ± 0.002	0.17 ± 0.002

Table 9.8: Level 6 jet E_T vs MET, with $\mid \eta \mid$ held constant at 2. The most optimal point is found by increasing the jet E_T cut to 25 GeV, and not changing the MET. Numbers in italics are the baseline, bold-faced numbers are the most optimal.

Jet $\mid \eta \mid$:	1.5	1.75	2.0	2.25	2.5
Jet E_T : 15 GeV					
S/total	4.56	4.54	*4.45*	4.44	4.39
S/B	2.52 ± 0.02	2.23 ± 0.01	*1.94*	1.88 ± 0.01	1.79 ± 0.01
Significance	4.72 ± 0.01	4.74 ± 0.01	*4.69*	4.70 ± 0.01	4.68 ± 0.01
Purity	0.72 ± 0.02	0.69 ± 0.01	*0.66*	0.65 ± 0.01	0.64 ± 0.01
top accep	0.042 ± 0.001	0.044 ± 0.001	*0.045*	0.045 ± 0.001	0.046 ± 0.001
ϵ_1	0.46 ± 0.001	0.45 ± 0.0004	*0.45*	0.45 ± 0.0003	0.45 ± 0.0003
ϵ_2	0.17 ± 0.002	0.16 ± 0.001	*0.16*	0.15 ± 0.001	0.15 ± 0.001
Jet E_T : 20 GeV					
S/total	4.70	4.74	4.75	4.74	4.72
S/B	4.14 ± 0.06	3.68 ± 0.05	3.39 ± 0.04	3.16 ± 0.03	3.04 ± 0.03
Significance	4.77 ± 0.01	4.84 ± 0.01	4.86 ± 0.01	4.86 ± 0.01	4.85 ± 0.01
Purity	0.81 ± 0.02	0.79 ± 0.02	0.77 ± 0.01	0.76 ± 0.01	0.75 ± 0.01
top accep	0.038 ± 0.002	0.040 ± 0.002	0.041 ± 0.001	0.042 ± 0.001	0.042 ± 0.001
ϵ_1	0.46 ± 0.001	0.45 ± 0.001	0.45 ± 0.0003	0.45 ± 0.0001	0.45 ± 0.0002
ϵ_2	0.17 ± 0.002	0.16 ± 0.001	0.16 ± 0.001	0.16 ± 0.0002	0.15 ± 0.0004
Jet E_T : 25 GeV					
S/total	4.60	4.67	**4.71**	4.71	4.71
S/B	6.37 ± 0.13	5.64 ± 0.11	**5.23 ± 0.09**	4.89 ± 0.08	4.72 ± 0.07
Significance	4.63 ± 0.01	4.72 ± 0.01	**4.76 ± 0.01**	4.77 ± 0.01	4.77 ± 0.01
Purity	0.86 ± 0.01	0.85 ± 0.01	**0.84 ± 0.01**	0.83 ± 0.01	0.83 ± 0.01
top accep	0.033 ± 0.002	0.035 ± 0.002	**0.036 ± 0.002**	0.037 ± 0.002	0.037 ± 0.002
ϵ_1	0.46 ± 0.001	0.46 ± 0.001	**0.45 ± 0.001**	0.45 ± 0.001	0.45 ± 0.0004
ϵ_2	0.17 ± 0.002	0.16 ± 0.001	**0.16 ± 0.001**	0.16 ± 0.001	0.16 ± 0.0003
Jet E_T : 30 GeV					
S/total	4.33	4.42	4.46	4.48	4.48
S/B	9.05 ± 0.28	8.09 ± 0.21	7.50 ± 0.17	7.10 ± 0.18	6.87 ± 0.16
Significance	4.35 ± 0.013	4.45 ± 0.01	4.49 ± 0.01	4.51 ± 0.01	4.51 ± 0.01
Purity	0.90 ± 0.01	0.89 ± 0.01	0.88 ± 0.01	0.88 ± 0.01	0.87 ± 0.01
top accep	0.028 ± 0.003	0.030 ± 0.002	0.031 ± 0.002	0.031 ± 0.002	0.031 ± 0.002
ϵ_1	0.46 ± 0.001	0.46 ± 0.001	0.46 ± 0.001	0.46 ± 0.001	0.45 ± 0.001
ϵ_2	0.18 ± 0.003	0.17 ± 0.002	0.16 ± 0.001	0.16 ± 0.001	0.16 ± 0.001
Jet E_T : 35 GeV					
S/total	3.94	4.03	4.08	4.09	4.09
S/B	11.35 ± 0.46	10.39 ± 0.37	9.83 ± 0.32	9.35 ± 0.28	9.02 ± 0.26
Significance	3.96 ± 0.01	4.05 ± 0.01	4.10 ± 0.01	4.11 ± 0.01	4.11 ± 0.01
Purity	0.92 ± 0.01	0.91 ± 0.01	0.91 ± 0.01	0.90 ± 0.01	0.90 ± 0.01
top accep	0.023 ± 0.003	0.024 ± 0.002	0.025 ± 0.003	0.025 ± 0.003	0.025 ± 0.003
ϵ_1	0.46 ± 0.001	0.46 ± 0.001	0.46 ± 0.001	0.46 ± 0.001	0.46 ± 0.001
ϵ_2	0.18 ± 0.003	0.17 ± 0.002	0.17 ± 0.002	0.16 ± 0.002	0.16 ± 0.002

Table 9.9: Level 6 jet E_T vs jet $\mid \eta \mid$, with MET held constant at 20 GeV. The most optimal point is found by increasing the jet E_T cut to 25 GeV, and not changing the η cut. Numbers in italics are the baseline, bold-faced numbers are the most optimal.

Jet E_T :	15	20	25	30	35
MET : 20 GeV					
S/total	*3.16*	3.54	**3.59**	3.47	3.20
S/B	*1.17*	2.07 ± 0.02	**3.22 ± 0.05**	4.63 ± 0.12	6.08 ± 0.19
Significance	*3.41*	3.65 ± 0.01	**3.65 ± 0.01**	3.50 ± 0.01	3.22 ± 0.01
Purity	*0.54*	0.68 ± 0.01	**0.76 ± 0.01**	0.82 ± 0.01	0.86 ± 0.01
top accep	*0.045*	0.041 ± 0.001	**0.037 ± 0.002**	0.031 ± 0.002	0.025 ± 0.003
MET : 25 GeV					
S/total	3.16	3.46	3.50	3.37	3.10
S/B	1.28 ± 0.01	2.16 ± 0.03	3.33 ± 0.06	4.73 ± 0.11	6.21 ± 0.21
Significance	3.37 ± 0.005	3.57 ± 0.01	3.55 ± 0.01	3.40 ± 0.01	3.12 ± 0.01
Purity	0.56 ± 0.01	0.68 ± 0.01	0.77 ± 0.01	0.83 ± 0.01	0.86 ± 0.01
top accep	0.042 ± 0.001	0.039 ± 0.002	0.034 ± 0.002	0.029 ± 0.002	0.024 ± 0.002
MET : 30 GeV					
S/total	3.10	3.36	3.38	3.23	2.98
S/B	1.35 ± 0.01	2.26 ± 0.03	3.47 ± 0.06	4.87 ± 0.13	6.46 ± 0.20
Significance	3.27 ± 0.01	3.44 ± 0.01	3.42 ± 0.01	3.26 ± 0.01	3.00 ± 0.01
Purity	0.58 ± 0.02	0.69 ± 0.02	0.78 ± 0.01	0.83 ± 0.01	0.87 ± 0.01
top accep	0.039 ± 0.002	0.036 ± 0.002	0.032 ± 0.002	0.027 ± 0.003	0.022 ± 0.003

Table 9.10: Level 5 jet E_T vs MET, with $|\eta|$ held constant at 2. The cross section used to generate our expected signal at each set of test cuts is now the measured value of 4.5 pb. It is quite clear that the most optimal point is still at jet E_T of 25 GeV, and the MET value does not change. Numbers in italics are the baseline, bold-faced numbers are the most optimal.

Jet $\mid \eta \mid$:	1.5	1.75	2.0	2.25	2.5
Jet E_T : 15 GeV					
S/total	3.33	3.28	3.18	3.16	3.11
S/B	1.55 ± 0.01	1.36 ± 0.01	*1.19*	1.15 ± 0.01	1.09 ± 0.01
Significance	3.50 ± 0.01	3.49 ± 0.01	*3.43*	3.43 ± 0.004	3.40 ± 0.01
Purity	0.61 ± 0.02	0.58 ± 0.01	*0.54*	0.53 ± 0.01	0.52 ± 0.01
top accep	0.042 ± 0.001	0.044 ± 0.001	*0.045*	0.046 ± 0.001	0.046 ± 0.001
Jet E_T : 20 GeV					
S/total	3.56	3.57	3.55	3.52	3.50
S/B	2.57 ± 0.04	2.27 ± 0.03	2.08 ± 0.02	1.94 ± 0.02	1.86 ± 0.02
Significance	3.64 ± 0.01	3.67 ± 0.01	3.67 ± 0.01	3.65 ± 0.01	3.63 ± 0.01
Purity	0.72 ± 0.01	0.70 ± 0.01	0.68 ± 0.01	0.66 ± 0.01	0.65 ± 0.01
top accep	0.038 ± 0.002	0.040 ± 0.002	0.042 ± 0.001	0.042 ± 0.001	0.042 ± 0.001
Jet E_T : 25 GeV					
S/total	3.55	3.59	**3.61**	3.60	3.59
S/B	3.96 ± 0.09	3.50 ± 0.07	**3.24 ± 0.05**	3.03 ± 0.05	2.93 ± 0.05
Significance	3.60 ± 0.01	3.65 ± 0.01	**3.67 ± 0.01**	3.67 ± 0.01	3.66 ± 0.01
Purity	0.80 ± 0.01	0.78 ± 0.01	**0.76 ± 0.01**	0.75 ± 0.01	0.75 ± 0.01
top accep	0.034 ± 0.002	0.036 ± 0.002	**0.037 ± 0.002**	0.037 ± 0.002	0.038 ± 0.002
Jet E_T : 30 GeV					
S/total	3.39	3.46	3.48	3.48	3.48
S/B	5.59 ± 0.16	5.00 ± 0.12	4.66 ± 0.12	4.39 ± 0.10	4.26 ± 0.10
Significance	3.42 ± 0.01	3.49 ± 0.01	3.51 ± 0.01	3.52 ± 0.01	3.52 ± 0.01
Purity	0.85 ± 0.01	0.83 ± 0.01	0.82 ± 0.01	0.82 ± 0.01	0.81 ± 0.01
top accep	0.029 ± 0.002	0.030 ± 0.002	0.031 ± 0.002	0.032 ± 0.002	0.032 ± 0.002
Jet E_T : 35 GeV					
S/total	3.12	3.18	3.22	3.22	3.23
S/B	7.23 ± 0.24	6.63 ± 0.23	6.26 ± 0.20	5.89 ± 0.17	5.71 ± 0.16
Significance	3.14 ± 0.01	3.20 ± 0.01	3.24 ± 0.01	3.24 ± 0.01	3.25 ± 0.01
Purity	0.88 ± 0.01	0.87 ± 0.01	0.86 ± 0.01	0.86 ± 0.01	0.85 ± 0.01
top accep	0.023 ± 0.003	0.025 ± 0.003	0.025 ± 0.003	0.026 ± 0.003	0.026 ± 0.003

Table 9.11: Level 5 jet E_T vs jet $\mid \eta \mid$, with MET held constant at 20 GeV. The cross section used to generate our expected signal at each set of test cuts is now the measured value of 4.5 pb. It is quite clear that the most optimal point is still at jet E_T of 25 GeV, and the MET value does not change. Numbers in italics are the baseline, bold-faced numbers are the most optimal.

Jet E_T :	15	20	25	30	35
MET : 20 GeV					
S/total	*6.39*	6.78	**6.70**	6.37	5.83
S/B	*1.83*	3.23 ± 0.04	**5.00 ± 0.09**	7.21 ± 0.17	9.5 ± 0.32
Significance	*6.58*	6.86 ± 0.01	**6.74 ± 0.01**	6.39 ± 0.02	5.84 ± 0.02
Purity	*0.65*	0.76 ± 0.03	**0.83 ± 0.03**	0.88 ± 0.02	0.91 ± 0.02
top accep	*0.0449*	0.041 ± 0.001	**0.037 ± 0.002**	0.031 ± 0.002	0.025 ± 0.003
MET : 25 GeV					
S/total	6.31	6.60	6.51	6.16	5.64
S/B	1.99 ± 0.01	3.36 ± 0.04	5.19 ± 0.10	7.32 ± 0.19	9.67 ± 0.32
Significance	6.47 ± 0.01	6.67 ± 0.01	6.55 ± 0.02	6.18 ± 0.02	5.65 ± 0.02
Purity	0.67 ± 0.03	0.77 ± 0.03	0.84 ± 0.03	0.88 ± 0.02	0.91 ± 0.02
top accep	0.042 ± 0.001	0.039 ± 0.002	0.034 ± 0.002	0.029 ± 0.002	0.024 ± 0.003
MET : 30 GeV					
S/total	6.13	6.39	6.27	5.92	5.41
S/B	2.11 ± 0.01	3.53 ± 0.05	5.4 ± 0.11	7.59 ± 0.21	10 ± 0.35
Significance	6.27 ± 0.01	6.44 ± 0.01	6.3 ± 0.02	5.94 ± 0.02	5.42 ± 0.02
Purity	0.69 ± 0.04	0.78 ± 0.03	0.84 ± 0.03	0.88 ± 0.02	0.91 ± 0.02
top accep	0.039 ± 0.002	0.036 ± 0.002	0.032 ± 0.002	0.027 ± 0.003	0.022 ± 0.003

Table 9.12: Level 5 jet E_T vs MET, with $|\eta|$ held constant at 2. The cross section used to generate our expected signal at each set of test cuts is the Standard Model cross section of 7 pb, but we have doubled the luminosity used. As with the Level 5 study done using our current luminosity, the point which is most optimal is found by increasing the jet E_T to 25 GeV and not changing the MET. While this point has a lower statistical significance than the point at 20 GeV, the signal to background and purity are much higher, and the total significance is comparable. Numbers in italics are the baseline, bold-faced numbers are the most optimal.

Jet $\mid \eta \mid$:	1.5	1.75	2.0	2.25	2.5
Jet E_T : 15 GeV					
S/total	6.53	6.53	*6.41*	6.41	6.35
S/B	2.40 ± 0.02	2.12 ± 0.01	*1.84*	1.78 ± 0.01	1.7 ± 0.01
Significance	6.66 ± 0.01	6.68 ± 0.01	*6.61*	6.62 ± 0.01	6.58 ± 0.01
Purity	0.71 ± 0.04	0.68 ± 0.03	*0.65*	0.64 ± 0.03	0.63 ± 0.03
top accep	0.042 ± 0.001	0.044 ± 0.001	*0.045*	0.046 ± 0.001	0.046 ± 0.001
Jet E_T : 20 GeV					
S/total	6.71	6.78	6.80	6.78	6.76
S/B	4.00 ± 0.06	3.52 ± 0.04	3.24 ± 0.04	3.02 ± 0.03	2.9 ± 0.03
Significance	6.76 ± 0.02	6.85 ± 0.01	6.88 ± 0.01	6.87 ± 0.01	6.9 ± 0.01
Purity	0.80 ± 0.03	0.78 ± 0.03	0.76 ± 0.03	0.75 ± 0.02	0.74 ± 0.02
top accep	0.038 ± 0.002	0.040 ± 0.002	0.042 ± 0.001	0.042 ± 0.001	0.042 ± 0.001
Jet E_T : 25 GeV					
S/total	6.56	6.67	**6.72**	6.73	6.73
S/B	6.15 ± 0.13	5.44 ± 0.10	**5.03 ± 0.09**	4.72 ± 0.08	4.55 ± 0.07
Significance	6.58 ± 0.02	6.71 ± 0.02	**6.76 ± 0.01**	6.78 ± 0.01	6.77 ± 0.01
Purity	0.86 ± 0.03	0.85 ± 0.03	**0.83 ± 0.03**	0.83 ± 0.02	0.82 ± 0.03
top accep	0.034 ± 0.002	0.036 ± 0.002	**0.037 ± 0.002**	0.037 ± 0.002	0.038 ± 0.002
Jet E_T : 30 GeV					
S/total	6.18	6.32	6.39	6.41	6.41
S/B	8.68 ± 0.25	7.76 ± 0.20	7.24 ± 0.18	6.85 ± 0.16	6.64 ± 0.15
Significance	6.20 ± 0.02	6.34 ± 0.02	6.41 ± 0.02	6.43 ± 0.02	6.43 ± 0.02
Purity	0.90 ± 0.02	0.89 ± 0.02	0.88 ± 0.02	0.87 ± 0.02	0.87 ± 0.02
top accep	0.029 ± 0.002	0.030 ± 0.002	0.031 ± 0.002	0.032 ± 0.002	0.032 ± 0.002
Jet E_T : 35 GeV					
S/total	5.65	5.79	5.85	5.87	5.87
S/B	11.30 ± 0.40	10.40 ± 0.34	9.71 ± 0.30	9.17 ± 0.27	8.89 ± 0.26
Significance	5.66 ± 0.02	5.80 ± 0.02	5.86 ± 0.02	5.88 ± 0.02	5.88 ± 0.02
Purity	0.92 ± 0.02	0.91 ± 0.02	0.91 ± 0.02	0.90 ± 0.02	0.90 ± 0.02
top accep	0.023 ± 0.003	0.025 ± 0.003	0.025 ± 0.003	0.026 ± 0.003	0.026 ± 0.003

Table 9.13: Level 5 jet E_T vs jet $\mid \eta \mid$, with MET held constant at 20 GeV. The cross section used to generate our expected signal at each set of test cuts is the Standard Model cross section of 7 pb, but we have doubled the luminosity used. Numbers in italics are the baseline, bold-faced numbers are the most optimal.

BIBLIOGRAPHY

BIBLIOGRAPHY

[1] http://hepwww.ph.qmw.ac.uk/epp/glossary.html

[2] S. Willenbrock "The Standard Model and the Top Quark" hep-ph/0211067_v1, November 5, 2002

[3] G. Kane "TASI lectures : weak scale supersymmetry - a top-motivated-bottom-up approach" arXiv:hep-ph/0202185 v2, February 22, 2002

[4] M. L. Perl "The Discovery of the Tau lepton" SLAC-PUB-5937 September 1992

[5] L. M. Lederman "The Discovery of the Upsilon, Bottom Quark, and B Mesons" 3rd International Symposium on the History of Particle Physics June 1992

[6] D. Perkins Introduction to High Energy Physics Addison-Wesley Publishing, 1987

[7] D. Amidei, et al. "Measurement of the $p\overline{p} \rightarrow t\overline{t}$ cross section in the l + jets SECVTX tagged sample" CDF/ANAL/TOP/CDFR/6329 March 4, 2003

[8] D. Amidei, et al. "Measurement of the ttbar Production Cross Section in the SECVTX Tagged Sample" /CDF/ANAL/TOP/CDFR/6585 October 14, 2003

[9] A. Ahmadov, et al. "Top Quark Physics" hep-ph/0103033_v1, March 4, 2000

[10] "The CDF II Detector Technical Design Report" FERMILAB-Pub-96/390-E November, 1996

[11] S. Willenbrock "Studying the Top Quark" hep-ph/008189_v2, September 4, 2002

[12] "The Top Quark Review" Physical Review D Particles and Fields pg 428 - 432, July 1, 2002

[13] http://www-ed.fnal.gov/projects/exhibits/searching/content_1_1_2.html

[14] http://www-ed.fnal.gov/projects/exhibits/searching/content_1_1_3.html

[15] G. Kane Modern Elementary Particle Physics Addison-Wesley Publishing, 1996

[16] http://www-ed.fnal.gov/projects/exhibits/searching/content_3_1_3.html

[17] http://www-ed.fnal.gov/projects/exhibits/searching/content_4_4_4.html

[18] http://www.physics.ohio-state.edu/ klaus/phys780.20/projects/TOP_QUARK_DISCOVERY.pdf

[19] P. Mättig "QCD Tests at e^+e^- and pp Colliders" Quantum Chromodynamics : Theory and Experiment, Proceedings of the Third Lake Louise Winter Institute World Scientific 1988

[20] M. Cacciari, et. al "The t anti-t cross-section at 1.8-TeV and 1.96-TeV: A study of the systematics due to parton densities and scale dependence" hep-ph/0303085, March 11, 2003

[21] F. Halzen, A. Martin Quarks and Leptons : An Introductory Course In Modern Particle Physics John Wiley and Sons, 1984

[22] S. Dawson, R.K. Ellis, P. Nason "The Total Cross Section for the Production of Heavy Quarks in Hadronic Collisions" Nuc. Physics **B303** pg 607 - 633 (1988)

[23] http://www.fnal.gov/pub/inquiring/physics/accelerators/chainaccel.html

[24] S. Kilemnko, et al. "The CDF Run II Luminosity Monitor" CDF/DOC/CDF/CDFR/4330, September 18, 1997

[25] http://www-cdf.fnal.gov/internal/upgrades/tev_mon/short_answers.txt

[26] http://www-cdf.fnal.gov/internal/people/links/JacoboKonigsberg/instr02.ps

[27] H.J. Frisch, P.J. Wilson "Trigger Tower Organization and Summing in $\eta - \phi$ Space for Run II" CDF/DOC/TRIGGER/CDFR/2045 April 15, 1993

[28] P. J. Wilson "Specification of Trigger Tower Summing and E_T Weighting for ADMEM Boards" CDF/DOC/TRIGGER/PUBLIC/4781 October 16, 1998

[29] http://scienceworld.wolfram.com/physics/Pseudorapidity.html

[30] H. Wenzel "Tracking in the SVX" CDF/DOC/SEC_VTX/PUBLIC/1790 May 4, 1998

[31] K. Bloom, W.M. Yao ""Outside-In" Silicon Tracking at CDF" CDF/TRACKING/DOC/CDFR/CDF5991 June 17, 2002

[32] http://mlm.home.cern.ch/mlm/alpgen/

[33] http://www.thep.lu.se/~torbjorn/Pythia.html

[34] http://hepwww.rl.ac.uk/theory/seymour/herwig/

[35] http://wwwasd.web.cern.ch/wwwasd/geant/

[36] http://www.fnal.gov/pub/inquiring/physics/accelerators/00-635D.jpg

[37] http://www-cdfonline.fnal.gov/opshelp/stores/kumac/store_tot.gif

[38] http://www-cdf.fnal.gov/internal/upgrades/tdr/doc/cdfiso_transp.eps

[39] "The CDF II Detector Technical Design Report" FERMILAB-Pub-96/390-E Page 1-7 November, 1996

[40] http://www-ed.fnal.gov/projects/exhibits/searching/content_4_2_3.html

[41] "The CDF II Detector Technical Design Report" FERMILAB-Pub-96/390-E Page 1-9 November, 1996

[42] "The CDF II Detector Technical Design Report" FERMILAB-Pub-96/390-E Page 1-11 November, 1996

[43] D. Mohl, G. Petrucci, L. Thorndahl and S. Van Der Meer "Physics And Technique Of Stochastic Cooling" Phys. Rept. **58**, 73 (1980).

[44] S. Rappoccio, J. Guimaraes da Costa, K. Burkett "First look at SecVtx Using Event Primary Vertex Finder PrimeVtx" CDF/PUB/SEC_VTX/PUBLIC/6417 July 25, 2003

[45] S. Rappoccio, J. Guimaraes da Costa "Impact of PrimeVtx on SecVtx For Summer 2003 Conferences" CDF/PUB/SEC_VTX/PUBLIC/6666 September 5, 2003

[46] A. Mukhurjee "CTC and VTX Tracking" CDF/ANAL/TRACKING/PUBLIC/5490 November 16, 2000

[47] C. Hays, et al. "The COT Pattern Recognition Algorithm and Offline Code" http://phy.duke.edu/ hays/patternrecognition.ps

[48] H. Bachacou, et al. "$t\bar{t}$ Event Selection and Detection Efficiency for Winter 2003 Lepton+Jets Analysis CDF/TOP/PHYS/CDFR/6084 February 26, 2003

[49] A. Taffard "Run II Cosmic Ray Tagger" CDF/ANAL/MUON/CDFR/6100 August 27, 2002

[50] A. Taffard "RunII Cosmic Ray Tagger Performances" CDF/ANAL/MUON/PUBLIC/6255 January 6, 2003

[51] http://cdfcodebrowser.fnal.gov/CdfCode/source/JetMods/doc/JetModsDoc.html#jetclu

[52] J-F Arguin, et al. "Generic Jet Energy Corrections for Run II data used for the Winter Conferences" CDF/ANAL/JET/CDFR/6280 January 21, 2003

[53] http://www-cdf.fnal.gov/internal/cdfoperations/Escale/index.html

[54] J-F. Arguin, B. Heinemann "Underlying Event Corrections for Run II" CDF/ANAL/JET/CDFR/6239 February, 2003

[55] C. Rott et al. "SecVtx Optimization for the 2003 Winter Conferences" /CDF/PUB/SEC_VTX/PUBLIC/6242 January 7, 2003

[56] H. Bachacou, et al. "Efficiency of SecVtx B-Tag Used for 2003 Winter Conferences" CDF/DOC/SEC_VTX/CDFR/6291 March 18, 2003

[57] H. Bacacou, et al. "Efficiency of SecVtx B-Tag Used for 2003 Summer Conferences" CDF/DOC/SEC_VTX/CDFR/6543 June 30, 2003

[58] Physical Review D Particles and Fields, July 1, 2002

[59] B-Tag Working Group "Backgrounds for the SVX b-Tag Top Search : Run IA+IB" CDF/ANAL/TOP/CDFR/2965 January 20, 1995

[60] D. Glenzinski, et al. "A Five-Dimensional SecVtx Tag-Rate Matrix" CDF/DOC/SEC_VTX/CDFR/6378 March 14, 2003

[61] T. Liss "Corrections to the Top Cross Section" CDF/ANAL/TOP/CDFR/2482 February 20, 1994

[62] B. Roe Probability and Statistics in Experimental Physics Springer-Verlag New York, 2001

[63] K. Bloom "Estimating QCD Backgrounds to W Production" CDF/ANAL/TOP/CDFR/6559 July 9, 2003

[64] "Gauge and Higgs Bosons", Physical Review D Particles and Fields pg 23, July 1, 2002

[65] K. Bloom, et al. "ttbar Event Selection and Detection Efficiency for Summer 2003 Lepton+Jets Analyses" /CDF/PHYS/TOP/CDFR/6574 July 30, 2003

[66] H Bachacou, et al. "ttbar Event Selection and Detection Efficiency for Winter 2003 Lepton+Jets Analyses" /CDF/PHYS/TOP/CDFR/6084 February 26, 2003

[67] M. Coca and E. Halkiadakis "Central Electron Identification Efficiencies for Winter 2003 conferences" CDF/DOC/ELECTROWEAK/CDFR/6262 January 9, 2003

[68] Y. K. Kim, et al. "Trigger Efficiencies for High P_T Electrons" CDF/DOC/ELECTRON/CDFR/6234 December 16, 2002

[69] K. Bloom, et al. "Muon Efficiencies" CDF/ANAL/MUON/CDFR/6293 June 2, 2003

[70] D. Dagenhart and V. Martin "Muon Efficiencies for Summer Analyses" CDF/PUB/MUON/PUBLIC/6610 August 7, 2003

[71] M. Coca, et al. "Wenu Cross Section Analysis with Run II Data" CDF/DOC/ELECTROWEAK/CDFR/6300 May 12, 2003

[72] K. Bloom, et al. "Updated Measurements of sigma(ppbar→W→munu),sigma(ppbar→Z→mumu), and R using CDF Run II Data" CDF/PHYS/ELECTROWEAK/CDFR/6302 March 21, 2003

[73] D. Glenzinski, et al. "Run IIa COT Tracking Efficiency" CDF/PHYS/ELECTROWEAK/CDFR/5973 February 25, 2003

[74] D. Glenzinski "ttbar Acceptance Calculation for the Run 1B SVX B-Tag Analysis" /CDF/TOP/ANAL/CDFR/3403 November 7, 1995

[75] http://wwwcdf.fnal.gov/internal/physics/top/jets/jetcorrsystematics.html

[76] "Monte Carlo particle numbering scheme" Physical Review D Particles and Fields pg 242 - 245, July 1, 2002

[77] D. Amidei and H. Ray "Event Tagging Efficiency in the B-tagged Lepton+Jets ttbar Cross Section" CDF/DOC/TOP/CDFR/6598 August 18, 2003

[78] R. Erbacher, et al. "Measurement of the ttbar Cross Section using Kinematic Variables" CDF/ANAL/TOP/CDFR/6206 August 7, 2003